

Acoustic metamaterial properties of a 2D closed cellular solid with entrained fluid

THÈSE N° 7026 (2016)

PRÉSENTÉE LE 20 MAI 2016

À LA FACULTÉ DES SCIENCES ET TECHNIQUES DE L'INGÉNIEUR
LABORATOIRE DE MODÉLISATION MÉCANIQUE MULTI-ÉCHELLE
PROGRAMME DOCTORAL EN MÉCANIQUE

ÉCOLE POLYTECHNIQUE FÉDÉRALE DE LAUSANNE

POUR L'OBTENTION DU GRADE DE DOCTEUR ÈS SCIENCES

PAR

Vladimir DORODNITSYN

acceptée sur proposition du jury:

Prof. F. Gallaire, président du jury
Prof. W. Curtin, Dr B. Van Damme, directeurs de thèse
Prof. K. Van Den Abeele, rapporteur
Dr A. Bergamini, rapporteur
Dr H. Lissek, rapporteur



ÉCOLE POLYTECHNIQUE
FÉDÉRALE DE LAUSANNE

Suisse
2016



Abstract

Metamaterials are often defined as artificial compositions designed to exhibit desired physical properties. These materials attract a lot of research attention due to unusual behavior that may not yet have been seen in nature. Although there is no commonly accepted definition for metamaterials, they are typically associated with peculiar macroscale properties resulting from their substructure. The electromagnetic metamaterial concept was first developed in 1968. As the wave theory is similar in every field, the achievements in optics were reflected in acoustics several decades later. This allowed developing acoustic metamaterials with such extraordinary properties as negative refractive index, negative bulk modulus and mass density, acoustic lensing, sound wave spectral decomposition, and acoustic bandgaps. All of those features are not only attractive scientifically, but are of interest for plenty of potential applications, including sound and vibration insulation, waveguiding, audible and high-frequency filtering, and even seismic absorption.

On the other hand, cellular solids and saturated porous media have been studied for a long time. These media are abundant in nature as granular soils, wood, rocks, bones, and foams. Wave analysis in such environments typically requires some crucial assumptions which do not allow extending a theory to other configurations. An example of such a constraint is the openness of the cells in a medium. Many porous media applications are found in geophysics - particularly gas and oil extractions - the permeability of the cells plays an important role. The ad-hoc dynamic models for such media operate only with open-cell configuration. Moreover, the study is limited to the low-frequency analysis, omitting the influence of wave scattering. The latter, however, is the key source of dispersion in acoustic metamaterials.

Scattering may have two origins, geometrical or resonant. Bragg's scattering is determined by the geometrical configuration, such that constructive interference occurs only when the incident wave matches the characteristic size of a unit cell. This makes such systems practically inconvenient. The concept of resonant scattering, introduced about a decade ago, has much fewer limitations and is mostly determined by the dynamics of matrix inclusions.

In this thesis, a closed-cell cellular solid with thin vibrating walls and fluid-filled cells is

proposed as a new class of acoustic metamaterials. First, the dynamics of a prototypical square cell is investigated numerically considering periodic boundary conditions and taking into account fluid-structure interaction. The results are compared to Biot's theory of saturated porous media in the limit of a closed-cells system. The proposed configuration is studied with respect to dispersion sources, showing the presence of local resonant behavior for different combinations of relative density and entrained fluid. Surprisingly, semi-analytical models can be used to provide a bottom-up explanation of the structure's dynamic behavior. The presence of two pressure waves, slow and fast, is confirmed numerically and analytically. Finally, an experimental proof-of-concept was carried out.

Periodic cellular solids represent a versatile acoustic metamaterial platform characterized by low cost, simple, scalable design, which makes possible achieving the desired macroscopic behavior using different types of fluids and bulk materials.

Keywords: acoustic metamaterials, wave propagation, cellular solids, locally resonant materials, resonant scattering, homogenized models, FEM, fluid-structure interaction, experiment.

Zusammenfassung

Unter dem Begriff Metamaterialien versteht man zumeist künstliche Strukturen, die so konzipiert sind, dass sie gewisse erwünschte physikalische Eigenschaften aufweisen. Aufgrund ihres ungewöhnlichen Verhaltens, welches in manchen Fällen noch nicht in der Natur beobachtet wurde, ziehen diese Materialien großes wissenschaftliches Interesse auf sich. Zwar gibt es keine Übereinkunft darüber, was der Begriff Metamaterialien genau umfasst, doch werden sie zumeist mit besonderen makroskopischen Eigenschaften assoziiert, welche sich aus ihrer Substruktur ergeben. Das Konzept der elektromagnetischen Metamaterialien wurde zuerst 1968 vorgestellt. Da die Wellentheorie in ihrer Anwendung auf verschiedene Felder sehr ähnlich ist, folgten auf die Errungenschaften in der Optik einige Jahrzehnte später entsprechende Erfolge in der Akustik. Sie ermöglichten die Entwicklung akkustischer Metamaterialien mit solch außergewöhnlichen Eigenschaften wie einer negativen Brechzahl, einem negativen Kompressionsmodul, einer negativen effektiven Massendichte oder einer akkustischen Bandlücke, ferner Materialien die einen akkustischen Linseneffekt erzeugen oder die Spektralzerlegung von Schallwellen erlauben. All diese Eigenschaften sind nicht nur interessant für die Wissenschaft, sondern auch für viele potentielle Anwendungen, wie Lärm- und Vibrationsdämmung, Wellenleitung, Filterung im hörbaren und im Hochfrequenzbereich und sogar seismische Absorption.

Zelluläre Feststoffe und gesättigte poröse Medien wiederum sind schon seit langer Zeit Gegenstand der Forschung. Diese Medien sind reichlich in der Natur vorhanden, als granulare Feststoffe, Holz, Stein, Knochen oder Schäume. Eine Analyse der Wellen in solchen Medien erfordert zumeist einige kritische Annahmen, welche die Erweiterung einer Theorie auf andere Konfigurationen unmöglich machen. Ein Beispiel für solcherlei Einschränkung ist die Annahme offener Zellen im Medium. Viele Anwendungen poröser Materialien finden sich im geophysikalischen Bereich, insbesondere in der Gas- und Erdölextraktion. Die Permeabilität der Zellen spielt hier eine wichtige Rolle. Dynamische 'ad-hoc'-Modelle für solche Medien arbeiten ausschließlich mit offenzelligen Konfigurationen. Des Weiteren ist die Analyse auf den Niederfrequenzbereich beschränkt. Der Einfluss der Wellenstreuung wird vernachlässigt.

Letztere ist jedoch die Hauptursache für Dispersion in akkustischen Metamaterialien.

Wellenstreuung hat ihren Ursprung entweder in der Geometrie oder im Resonanzverhalten. Bragg'sche Streuung hängt von der Geometrie der jeweiligen Konfiguration ab. Konstruktive Interferenz tritt nur auf, wenn die Größe der einfallenden Welle gleich der charakteristischen Größe einer Einheitszelle ist. Das macht solche Systeme unpraktisch. Das Konzept der resonanten Streuung, welches vor etwa einem Jahrzehnt eingeführt wurde, hat wesentlich weniger Einschränkungen und hängt hauptsächlich von den dynamischen Eigenschaften der Einschlüsse ab.

In dieser Arbeit wird eine neue Klasse von Metamaterialien vorgestellt. Es handelt sich dabei um zelluläre Feststoffe mit geschlossenen, flüssigkeitsgefüllten Zellen und dünnen, schwingenden Zellwänden. Zunächst wird das dynamische Verhalten einer prototypischen quadratischen Zelle numerisch untersucht, unter Annahme periodischer Randbedingungen und mit Einbeziehung der Fluid-Struktur-Wechselwirkung. Die Ergebnisse werden mit der Biot'schen Theorie für gesättigte poröse Medien und den Grenzfall geschlossenzelliger Systeme verglichen. Die vorgestellte Konfiguration wird auf Dispersionsquellen hin untersucht. Hier zeigt sich für bestimmte Kombinationen von relativer Dichte und eingeschlossener Flüssigkeit lokales Resonanzverhalten. Überraschenderweise können semianalytische Modelle das dynamische Verhalten der Struktur erklären. Das Vorhandensein zweier Druckwellen, einer schnellen und einer langsamen, wird numerisch und analytisch bestätigt. Schließlich wurde die Realisierbarkeit dieses Konzepts experimentell bestätigt.

Periodische zelluläre Feststoffe stellen eine vielseitige Basis für akkustische Metamaterialien. Charakterisiert werden sie durch niedrige Kosten und einfaches, skalierbares Design, welches die Einstellung gewünschter makroskopischer Eigenschaften durch Auswahl verschiedener Fluide oder Matrix-Materialien ermöglicht.

Schlagwörter: akkustische Metamaterialien, Wellenausbreitung, zelluläre Feststoffe, lokales Resonanzverhalten, resonante Streuung, homogenisierte Modelle, FEM, Fluid-Struktur-Wechselwirkung, Experiment

Contents

Abstract English/Deutsche	i
List of figures	ix
List of tables	xi
1 Introduction	1
1.1 Cellular and porous media	1
1.2 Metamaterials	5
1.2.1 Electromagnetic metamaterials	6
1.2.2 Mechanical metamaterials	6
1.3 Mechanical models	12
1.3.1 Numerical and homogenized models	12
1.3.2 Biot's theory for saturated porous media	13
1.4 Motivation and objectives of the thesis	20
1.5 Organization of the work	21
2 Numerical Model of a 2D Square Lattice With Entrained Fluid	23
2.1 Introduction	23
2.2 Lattice Geometry and Computational Models	25
2.2.1 Square-lattice geometry and RVE	25
2.2.2 RVE discretization	26
2.2.3 RVE analysis of plane harmonic waves	28
2.3 Wave propagation in a Two-phase Square Lattice	30
2.3.1 Band structure and wavemodes	30
2.3.2 Dispersion source analysis	33
2.4 Micro-Mechanical Pore Models and Comparison with FE Analyses	34
2.4.1 Equivalent continuum model for shear waves in a dry cellular solid	35
2.4.2 Comparison with Biot's theory	37

Contents

2.4.3	Comparison of analytical and FE models	40
2.5	Conclusion	44
3	Numerical and Homogenized Analysis of Pressure Waves	45
3.1	Introduction	45
3.2	Geometry, RVE, and Numerical Results	47
3.3	Micro-Mechanical Pore Models	48
3.3.1	Equivalent continuum model for pressure waves	49
3.3.2	Comparison of analytical and FE models	57
3.4	Macro-Mechanical Equivalent Continuum Model	59
3.4.1	Homogenized model for C_{11} and C_{12}	59
3.4.2	Dispersion surfaces and slowness curves	61
3.4.3	Extreme behavior of the pressure wave phase velocity	66
3.5	Conclusion	68
4	Analytical Analysis of Slow and Fast Pressure Waves	71
4.1	Introduction	71
4.2	Simplified Finite-Element Approach of P-waves	73
4.3	Analytical dispersion relation of P-wave Propagation	76
4.4	Rayleigh Quotient Analysis of the Analytical System	79
4.4.1	Differential eigenvalue problem	79
4.4.2	Existence of two fast P-waves with same group velocity	81
4.4.3	Analysis of the existence of a slow and fast P-wave with equal frequency	81
4.5	Conclusion	82
5	An Acoustic Metamaterial with Negative Index: Experimental Validation	85
5.1	Introduction	85
5.2	Deformation analysis	86
5.3	Group velocity analysis. Negative index behavior	91
5.4	Partial bandgaps analysis	92
5.5	Conclusion	94
6	Conclusions	97
6.1	Summary of the results	97
6.2	Further outlook and possible applications	99
A	Appendix	105
A.1	Derivation of the analytical dispersion relation	105

Contents

Bibliography	117
Curriculum Vitae	119

List of Figures

1.1 Cellular and porous media classification	2
1.2 Overview of cellular materials by origin type	3
1.3 Examples of static metamaterials	7
1.4 Examples of acoustic metamaterials	9
1.5 Scattering sources	10
2.1 Square lattice geometry	25
2.2 Discretized RVE	26
2.3 Direct and reciprocal lattice	29
2.4 Band structure for RVE with $\rho^* = 0.04$	31
2.5 FSI wavemodes of a system with $\rho^* = 0.04$	31
2.6 Band structure for RVE discretized with plane elements and $\rho^* = 0.04$	33
2.7 Dispersion sources analysis	34
2.8 Examples of the unit cell model with different walls thickness	35
2.9 Band structure for a porous medium with entrained air	36
2.10 Band structures for a square lattice with entrained air and varying relative density	41
2.11 Phase velocities for shear and pressure waves for different fluids as a function of relative density	43
3.1 Band structure for RVE discretized with beam elements with the focus on pres- sure waves	48
3.2 Tube-piston model	49
3.3 Representation of the aligned tube-piston unit cells as system of springs and masses	50
3.4 Band structure detail about the Γ point for beam and plane elements	53
3.5 Pressure wave analysis. Case 1	54
3.6 Pressure wave analysis. Case 2	55
3.7 Pressure wave analysis. Case 3	56

List of Figures

3.8	Comparison of phase velocities for shear and pressure waves	58
3.9	Homogenized model for C_{11} and C_{12}	60
3.10	Dispersion surfaces corresponding to case 1	62
3.11	Dispersion surfaces corresponding to case 2	63
3.12	Slowness curves for shear and pressure waves	65
3.13	Extreme behavior of pressure wave phase velocity	66
3.14	Deformation regimes for different types of entrained fluid	67
4.1	Band-structure limited to $\Gamma - X$ path for $\rho^* = 0.04$	72
4.2	Simplified finite-element and equivalent-continuum models	74
4.3	Comparison of band-structures: simplified and full finite-element models . . .	76
4.4	Comparison of band-structures: analytical and full finite-element models . . .	78
4.5	Comparison of Rayleigh's and analytical models	80
4.6	Analytical wavemodes	81
4.7	Dependence of Rayleigh quotient on the rigid body shift of the wavemode . . .	83
5.1	Numerical and experimental wavemodes comparison	86
5.2	Experimental setup	88
5.3	Measurement of stress-strain relation	90
5.4	Experimental group velocity analysis	91
5.5	Experimental bandgap analysis	94
6.1	Band-structure for the fcc rhombic dodecahedron foam with entrained water .	100
6.2	Band-structure for the solid phase consisting of two bulk materials	102



List of Tables

2.1	Relation between stiffness-tensor constants and parameters of the strain-energy density	40
3.1	Material and geometrical properties used in Cases 1, 2 and 3.	51
4.1	Material and geometrical properties used in Chapter 4	73

1 Introduction

1.1 Cellular and porous media

Cellular media are characterized by a mesoscale alignment of cells. The prefix '*meso*-' indicates an intermediate extent between the microscopic material parameters and the macroscopic behavior of the structure. The unusual mechanical properties caused by the substructure in terms of both static and dynamic behavior have been studied intensively over the past decades. Such media can be classified in various ways, however the most feasible one is to differentiate first by material origin, natural or synthetic (man-made). A chart showing a possible segmentation is shown in Fig. 1.1. Some examples of media of natural origin are shown in Fig. 1.2(a-f), and of man-made origin in Fig. 1.2(g-l). The proposed classes and their interrelations will be discussed further throughout this chapter.

Historically, a detailed study of mechanics of porous media began as a practical implication for the extraction of natural resources (mostly of oil and gas). Soil typically contains two phases: a solid phase (a granular structure such as ground or sand) and a compressible fluid phase filling the pores. In some special occasions, it can even be a three-phase medium, such as an air-fluid-sand system [Lenhard and Parker, 1987]. Porous media contain an interconnected network of pores with fluid channels through which flows are allowed. The pioneer of the dynamic theory of porous media is M.A. Biot, a consultant with the Shell Development Company. In 1955 Biot introduced the theory of propagation of elastic waves in a saturated porous medium [Biot, 1956a,b], which was derived from a macroscale strain-energy functional based on averaged microstructural quantities. Biot's technique became fundamental in geophysics [Dutta and Odé, 1979, Rice and Cleary, 1976] and poroelasticity [Dauchez et al., 2001, Sherwood, 1993], and will be discussed in more detail in Sec. 1.3.2. Some examples of porous media are shown

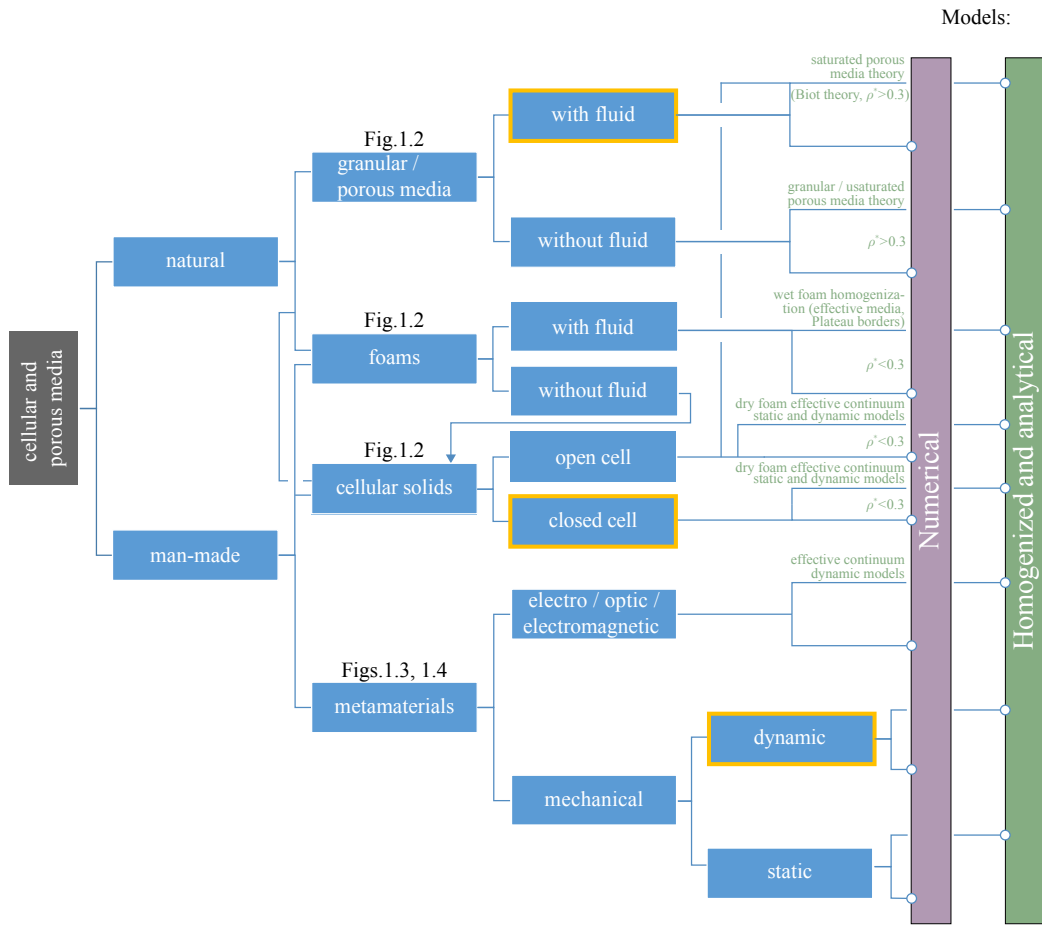
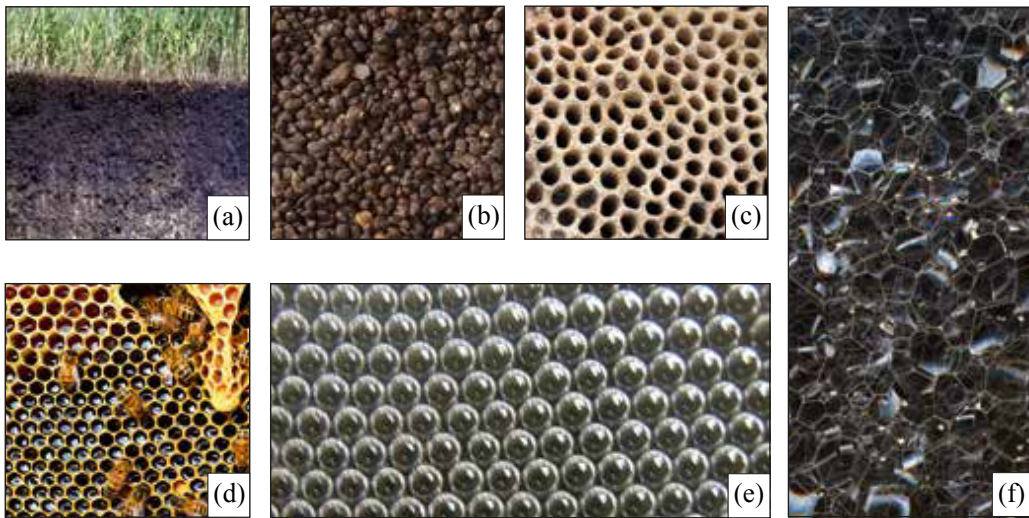


Figure 1.1 – Cellular and porous media classification. The fields of interest for this work are highlighted.

in Fig. 1.2(a-b).

Foams form the next class in Fig. 1.1, a substance formed by trapping gas in a solid or liquid matrix. It can be manufactured or found in nature. These media have fascinated mathematicians, physicists and biologists by its topological, physical and functional behavior [Gibson and Ashby, 1999]. For instance, William Thomson (better known as Lord Kelvin) studied the packaging properties of the cells, Robert Hooke analyzed the foam's formation, and Charles Darwin tested its functionality. It is remarkable that even natural systems obtain a regular structure with a mesoscale periodicity. One of the most compelling structures, perhaps, is the honeycomb - a typical organic cellular architecture that has a hexagonal shape (Fig. 1.2(d)). Every object in nature tends to occupy an energetically optimal state. Already in the 19th century, Darwin noticed the honeycombs to be absolutely perfect in terms of economizing bees' labor and wax. This phenomenon is explained by the mathematical problem of separation

Natural:



Man-made:

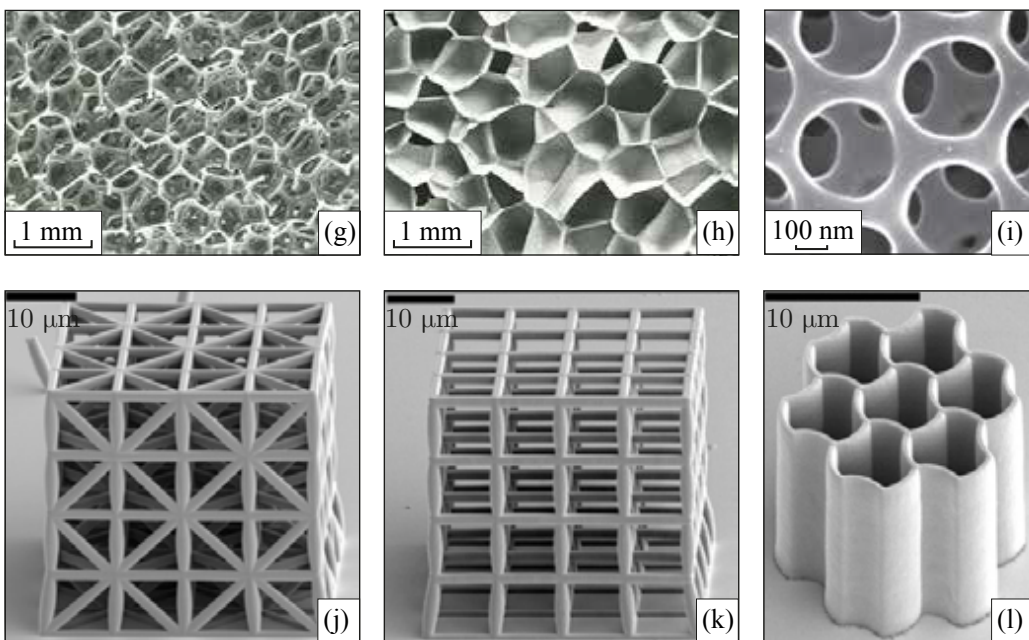


Figure 1.2 – Overview of cellular materials by origin type. The Creative Commons license is applied unless noted otherwise. (a) cross section of a granular soil, (b) organic fertilizers, (c) fossil coral, (d) bee honeycomb, (e) air bubbles in foam, (f) soap foam, (g) open-cell polyurethane foam [Gibson, 2005], (h) closed-cell polyethylene foam [Gibson and Shi, 1997], (i) A carbon metamaterial created by carbonization of a polymer [Lee et al., 2012], (j)-(l) scanning electron microscope images of cellular microarchitectures [Bauer et al., 2014]. Figures (g-l) are reprinted with permission from respective references.

Chapter 1. Introduction

of space into units of the same volume with the least interfacial area. In case of a 2D packed medium, the hexagonal honeycomb represents an optimal solution.

In case of 3D space, the solution is still unknown. Plateau [Plateau, 1873] first studied the geometry of solids in terms of the surface energy minimization, proposing a rhombic dodecahedron as a possible solution. A decade later, Lord Kelvin proposed a 3D geometry of a cell with slightly curved edges for the partitioning based on the body center cubic symmetry [Thomson, 1887], which had less surface energy than Plateau's solution. However, a century after, computer capabilities allowed Weaire and Phelan to introduce a unit cell comprising a dodecahedron and a polyhedron similar to what can be found in clathrate compounds, polymeric substances represented by a lattice with trapped molecules [Weaire and Phelan, 1994]. The latter solution was recently overturned by Gabbrielli who employed a complex topology optimization of 3D periodic point sets [Gabbrielli, 2009]. These studies eventually lead to numerous inspiring applications, like new manufacturing techniques of metal nanohole arrays [Masuda and Fukuda, 1995], cutting edge graphene studies [Allen et al., 2009], and self-organized micrometer-scale polymer films [Widawski et al., 1994].

Returning to foams, one can distinguish two subcategories: dry (no fluid, Fig. 1.2(g-h)) and wet (with fluid, Fig. 1.2(e-f)) foams. The latter owe their existence to the presence of surfactants or constituents which are concentrated and active on the surface [Weaire and Hutzler, 2001]. Generally, surfactants reduce the surface energy and stabilize the formation of Plateau's borders, which represent channels of finite width for fluid transportation between the cells. The presence of Plateau's borders distinguishes the foam type between two extremities of dry and wet foam.

Dry foams are also called cellular solids, a lattice composed of an interconnected network of solid plates or struts (third class in Fig. 1.1). Some examples of natural cellular solids are shown in Fig. 1.2(c-d), and man-made with diverse unit cell typologies in Fig. 1.2(g-l). Even though the manufacturing techniques for dry foams and cellular solids are different [Gibson and Ashby, 1999], dry foams are still described within the same concept used for the cellular solids, which makes the practical difference almost imperceptible.

Cellular solids can be distinguished from porous media in terms of relative density, the actual solid fraction in a medium:

$$\rho^* = V_s/V, \tag{1.1}$$

where V_s is the portion of total volume V occupied by the solid fraction. Following the

phenomenological rule by [Gibson and Ashby, 1999], the limit value is $\rho^* = 0.3$: cellular solids exist for $\rho^* < 0.3$, otherwise it becomes a medium with pores. Cellular solids can be further classified based on the openness of the pores. It might have an open-cell (Fig. 1.2(g)) or closed-cell (Fig. 1.2(h)) configuration. In contrast to open-cell foam, the closed-cell configuration implies cavities form in discrete pockets.

Adding fluid in cellular solids significantly complicates its static and dynamic behavior, as in porous materials. As an additional complication, the macroscopic properties depend not only on the solid and fluid bulk parameters, but also on the interaction of both phases. The low relative density allows a strong interaction, so that the entrained fluid plays an important role even in closed-cell materials.

1.2 Metamaterials

Metamaterials are the final class in Fig. 1.1. They are characterized as artificial compositions designed to exhibit desired physical properties, and they are widely developing nowadays. Materials with a tuned internal microstructure can even exhibit properties that have not yet been found in nature. There is no general valid definition of a metamaterial, however it is mostly associated with peculiar macroscale properties due to its substructure. Although materials with a periodic microstructure have been studied since the early 20th century [Darwin, 1914, Harkins, 1917], compound systems have attracted significant attention only over the past two decades. Modern manufacturing techniques facilitate the production of applications with predefined properties, both optical and mechanical. The underlying physics is often non-intuitive, thus causing a lot of discussion and definitely having a high impact on applications in various domains [Cui et al., 2014].

Metamaterials are always represented as structures with internal periodicity resulting in properties beyond the well-studied response of a standard bulk material. Metamaterials comprise two major families: electromagnetic/optic and mechanical. The latter can be studied in the context of structural elasticity (static), and in the context of elastic wave propagation (dynamic). A short discussion on electromagnetic metamaterials in Sec. 1.2.1 is followed by a review of mechanical metamaterials in Sec. 1.2.2 with a specific focus on acoustic properties.

1.2.1 Electromagnetic metamaterials

Most scientists agree that the metamaterials pioneer was Victor G. Veselago. In his work from 1968 [Veselago, 1968] he developed a theory in which negative refraction occurs as a consequence of electric permittivity and magnetic permeability both being negative. This prediction was confirmed experimentally only in 2000, using an appropriate composite material consisting of copper ring resonators [Smith et al., 2000]. One of the most important findings was not the fact that such material can exist, but that it can be designed with any chosen value of permittivity and permeability. This discovery gave birth to many related studies, such as the planar "superlenses", which provide an improved resolution [Pendry, 2000], or an electromagnetic invisibility cloak, in which scattering from an object is decreased [Schurig et al., 2006].

1.2.2 Mechanical metamaterials

Static metamaterials

The concept of designed elasto-static materials (also known as extremal materials) was introduced by [Milton and Cherkaev, 1995]. The idea which inspired the authors was to show that it is possible to realize any given positive definite fourth order elasticity tensor (satisfying the usual symmetries) using a two-phase composite. The proposed material was introduced as a combination of sufficiently compliant and rigid isotropic phases. The suggested laminates represent pentamode materials, 3D solid structures that can only support longitudinal but not shear deformations. They therefore behave similar to an inviscid fluid. If such a material is subjected to acoustic wave propagation analysis, it is sometimes referred to as an acoustic metafluid [Norris, 2009].

Theoretically the pentamode material class assumes the combination of two constituents: an absolutely rigid and an absolutely compliant one. Clearly, these limitations can only be approximated. The mathematical description of a pentamode material uses the straightforward idea of obtaining an effective stiffness tensor which has five small eigenvalues (ideally zero) and one large eigenvalue. The detailed mathematical derivations can be found in [Itskov, 2000]. It is worth mentioning that since the pentamode model was introduced, it took a rather long time before the results were confirmed experimentally. Only in 2012, the theory found a real-life counter part [Kadic et al., 2012]. The unit cells consisted of double-cone elements arranged in a diamond-type crystal. The polymer structure was fabricated using dip-in direct-laser-writing optical lithography. Even though the connection was not infinitely

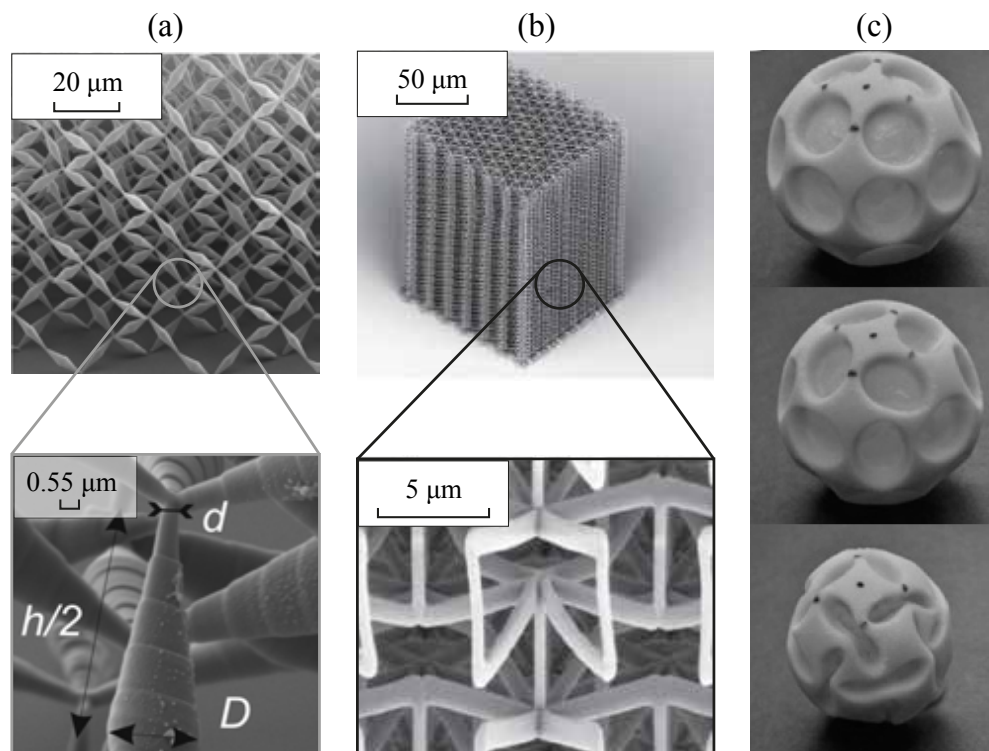


Figure 1.3 – Some examples of static metamaterials. (a) An experimentally realized pentamode material [Kadic et al., 2012], (b) a cellular solid with negative Poisson’s ratio [Bückmann et al., 2012], (c) the Buckliball [Shim et al., 2012]. All figures are reprinted with permission from respective references.

small, it was sufficiently narrow to confirm the pentamode properties. The smallest realized diameter of the connection region of adjacent cones was of order $d = 0.55 \mu\text{m}$, which can be seen in the oblique-view electron micrograph shown in Fig. 1.3(a).

Other materials are branched off from foam properties. As was shown in [Lakes, 1987] a foam comprised of 24-sided polyhedron cells exhibits a negative Poisson’s ratio, a characteristic known as auxetics. The foam samples that were studied by Lakes have an organic origin, whereas more recent works propose several approaches for an artificial cellular structure with negative Poisson’s ratio. A cellular solid fabricated using multiphoton lithography [Bückmann et al., 2012] (Fig. 1.3(b)), a microporous polyethylene structure manufactured with a laser micromachining setup [Alderson and Evans, 1992], or even a porous spherical shell made of a soft silicone-based rubber that due to the auxetic properties undergoes a structural transformation induced by buckling under a pressure load ([Shim et al., 2012] Fig. 1.3(c)) are some recent examples.

Dynamic (acoustic) metamaterials

The revolutionary results of optical metamaterials were soon extrapolated to the mechanical metamaterial domain. As the basic concept of wave theory is similar for every field, it was an interesting exercise to translate the optics to elastodynamic acoustic waves. As a starting point, the sound attenuation by a particular sculpture was observed by [Martinezsala et al., 1995]. This sculpture by Eusebio Sempere is shown in Fig. 1.4(a). It is made of periodically spaced hollow steel cylinders with a diameter of 2.9 cm, fixed on a rotatable platform. The lattice has a simple cubic symmetry with a unit cell of 10 cm. Studying the propagation of sound waves the authors demonstrated several attenuation peaks in the audible frequency range up to 5 kHz.

Three years later, the phenomenon of elastic wave attenuation within certain frequency ranges was described numerically and experimentally [Sánchez-Pérez et al., 1998]. This phenomenon became known as the acoustic bandgap, analogous to photonic bandgaps occurring in crystals at near-infrared wavelengths [Krauss et al., 1996].

Bandgaps are the most studied and desired phenomena for acoustic metamaterials due to the wide application range. In principle, they can result from Bragg scattering at wavelengths comparable to the characteristic size of a unit cell, or from resonant scattering due to in-lattice resonators.

Bragg diffraction was first proposed by William Henry Bragg and William Lawrence Bragg, father and son [Bragg and Bragg, 1913]. This article explored their discovery that crystalline solids produce intense peaks of reflected X-ray radiation in a certain direction. The described diffraction was limited to radiation with wavelengths λ comparable to the atomic spacing of the crystalline system. The reflected wave is experiencing constructive interference at certain angles of incidence θ for the interplanar distance d (Fig. 1.5(a)). Constructive interference implies that waves reflected at different levels are in phase, so that the traveled distance of each wave is an integer multiple of the wavelength. Thus constructive interference is reached when:

$$2d \sin \theta = n\lambda, \tag{1.2}$$

with n being a positive integer.

This concept has a geometrical origin and holds for every scale with a corresponding wavelength-frequency combination: starting from subatomic-level lattices [Cowley, 1995] and reaching

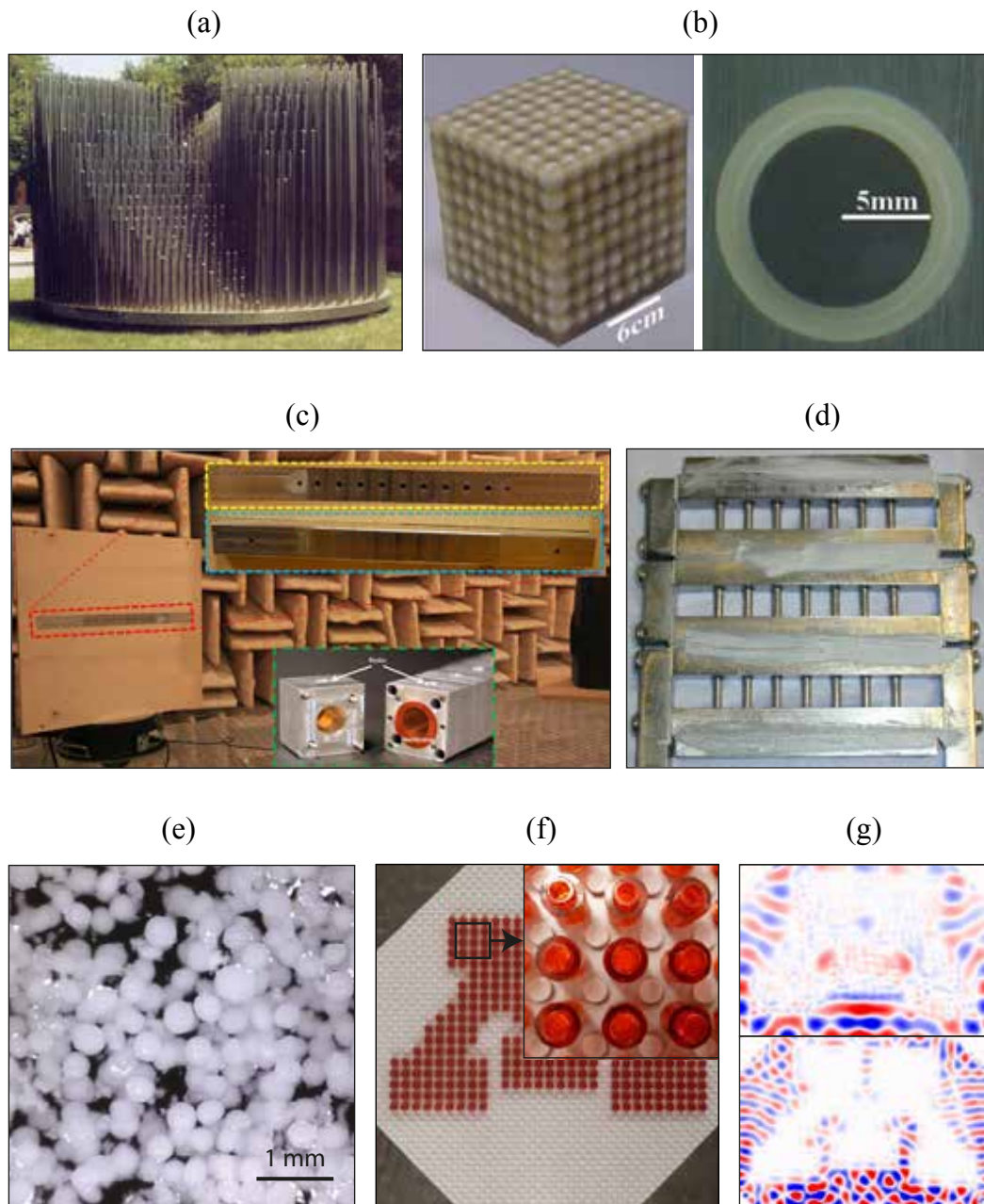


Figure 1.4 – Overview of acoustic metamaterials. (a) sculpture by Eusebio Sempere [Martinezsala et al., 1995], (b) locally resonant acoustic metamaterial [Liu et al., 2000], (c) frequency-dependent refractive index metamaterial acting as an acoustic prism [Esfahlani et al., 2016] (the Creative Commons license is applied), (d) acoustic metamaterial with negative index composed of Helmholtz resonators [Fok and Zhang, 2011], (e) soft 3D acoustic metamaterial with negative index [Brunet et al., 2015], (f) acoustic metamaterial comprised of the Lego blocks [Celli and Gonella, 2015] with its waveguide response at two different frequencies (g). Figures are reprinted with permission from respective references.

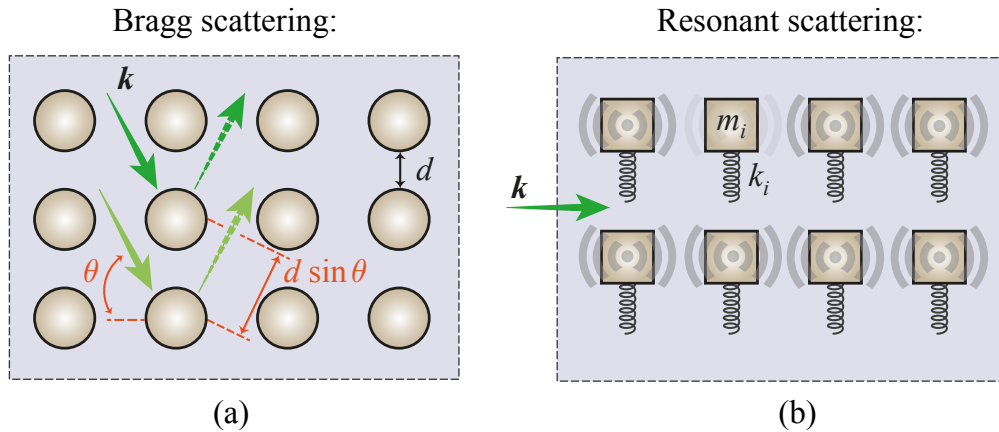


Figure 1.5 – Two scattering sources: (a) Bragg diffraction, and (b) local resonant scattering. Incident wave with corresponding wavevector \mathbf{k} is shown with solid arrow, while reflected one is in dash.

meter-sized structures [Martinezsala et al., 1995]. Therefore, an acoustic bandgap can only be obtained if the lattice distance d is at least a wavelength. In the case of low-frequency acoustic waves this requires structures of several meters, which is practically unfeasible.

Alternatively to Bragg scattering, a bandgap can result from resonant scattering (Fig. 1.5(b)). In that case energy dissipates due to in-lattice resonators which are spaced at the distance independent of the wavelength they interact with. Some authors identify resonant scattering as a distinctive feature of acoustic metamaterials, while using the term phononic crystals in case of Bragg scattering materials [Banerjee, 2011].

The pioneering work, describing wave propagation in the resonant-based system, was experimentally realized by [Liu et al., 2000]. The authors fabricated a lattice composed of centimeter-sized lead balls, coated with a layer of silicone (shown in Fig. 1.4(b)). The assembled structure exhibited bandgaps, strong dips of acoustic transmission in narrow frequency bands, due to resonance of the inclusions whose spacing was two orders of magnitude smaller than the relevant sonic wavelength.

Several more concepts discovered for electromagnetic metamaterials were reflected to the acoustic domain, such as cloaking and lensing. Acoustic cloaking was studied by [Chen and Chan, 2007], while lensing attracted ample research. Based on locally resonant behavior of an alignment of triple-layered rods the acoustic magnifying hyperlens was introduced by [Ao and Chan, 2008]. In [Molerón et al., 2014] the authors proposed a concept of acoustic lenses based on the principle of extraordinary acoustic transmission using a rigid plate with

subwavelength openings which guarantee the resonant scattering. Furthermore, as an extension to acoustic lenses, an acoustic analog of the optical dispersive prism was derived very recently by [Esfahlani et al., 2016]. The dispersive nature of the proposed metamaterial with frequency-dependent refractive index allowed the predicted splitting of sound waves towards different and frequency-dependent directions in the audible domain. The fabricated prototype was assembled from vibrating thin plates and open ducts combined in an acoustic waveguide with circular cross section. The acoustic prism is shown in Fig. 1.4(c) (zoomed in red frame with front and back sides in yellow and blue frames, respectively), a unit cell is also magnified (green frame).

The negative refractive index or left-hand behavior, one of the key ideas of an acoustic prism, represents another major research scope of mechanical metamaterials with local resonances. A negative refractive index represents the property of a material to contain frequency bands within which the phase and group velocities have different signs. Materials with left-hand behavior may result in such unusual properties as negative mass density and negative bulk modulus [Lee et al., 2009, Liu et al., 2011a]. The first experimental confirmation was done by [Fok and Zhang, 2011], where a water-based 2D acoustic metamaterial operating in the 18–22 kHz range was presented. The resonant behavior was guaranteed by rod-spring and Helmholtz resonators assembled into the system shown in Fig. 1.4(d) (rods are aligned horizontally, and Helmholtz resonators are perpendicular to it). Very recently [Brunet et al., 2015] showed a conceptually new 3D acoustic metamaterial with negative index which can be referred to as a metafluid, since it consists of a concentrated suspension of microbeads (see Fig. 1.4(e)). This soft metamaterial exhibits the left-hand behavior over a broad range of ultrasonic frequencies between 140 kHz and 275 kHz.

Finally, waveguiding is an important reason for engineers to study acoustic metamaterials. An interesting and easily reconfigurable concept, based on local resonant behavior, was proposed by [Celli and Gonella, 2015]. The authors exploited regularly spaced Lego blocks to create the desired substructures (see Fig. 1.4(f)). Spatial wave manipulation, such as waveguiding and seismic isolation, was studied in detail at different wavelengths. For the topology shown in Fig. 1.4(f), the waveguiding was achieved for wavelengths larger (Fig. 1.4(g) top) and shorter (Fig. 1.4(g) bottom) than the unit cell. Such waveguiding is highly demanded in problems of vibration analysis and seismic isolation [Kim and Das, 2012, Yan et al., 2014].

1.3 Mechanical models

1.3.1 Numerical and homogenized models

Every class of materials in Fig. 1.1 has its own well developed means of mechanical analysis. Due to the multiple scales, this results in a complicated mechanical and mathematical problem. For these purposes the employment of computational models is required. There are dozens of numerical techniques, most of which are based on energy variational methods for a discretized (meshed) geometry. Perhaps the most common technique used in almost every domain is finite element modeling [Cook, 2001], which allows to conveniently describe the mechanics of solids with complex geometry and boundary conditions. It is particularly useful when a fluid phase is considered in addition to the solid one. In order to couple both phases the fluid-structure interaction scheme can be employed [Belytschko, 1980]. For periodic structures, the numeric effort can be reduced to a minimum using the Bloch theorem. In this case, only one mesoscopic cell with appropriate boundary conditions is analyzed explicitly. It can be reduced even to a portion smaller than a unit cell if in addition to translational periodicity a structure has screw or glide symmetries [Maurin, 2016]. After employing the Bloch theorem, equations of motion derived for a specific configuration can be reformulated in terms of a generalized eigenvalue problem. The solution to it is often analyzed in terms of the band-structures, a typical tool to describe the wave propagation in a periodic lattice, originally emerged in solid state physics used to characterize the range of energies (bands) that an electron within the solid is allowed to have [Kittel, 2004].

On the other hand, homogenized models can be considered to explain the complete but possibly difficult to interpret result from a numerical analysis. A homogenized model is a bottom-up approach, aiming to derive the macroscopic behavior from micro- and mesoscale models. The latter are typically described in terms of effective parameters. The output of these models is the required approximation of macroscopic characteristics, such as the equivalent Young's modulus or phase and group velocities. In case of statics, the cellular solids theory for certain geometries provides very precise equivalent continuum formulations [Gibson and Shi, 1997]. In case of dynamics, such models should retain the important properties of the system and exhibit the same behavior in the considered frequency and wavenumber ranges. These models are useful to understand the physical mechanism responsible for the wave propagation. Comparing the energy stored in a unit cell and in an equivalent continuum can provide an effective technique for cellular solids with low relative density [Bažant and Christensen, 1972, Kumar and McDowell, 2004]. In case of porous structures, Biot's theory for

saturated media is used instead. This ad-hoc homogenization is briefly introduced in the next section.

1.3.2 Biot's theory for saturated porous media

In the case of saturated porous solids, wave propagation is described by Biot's theory [Biot, 1956a,b] and many of its extensions [Brutsaert, 1964, Carcione et al., 2004, Santos et al., 1990]. The general idea is to disregard the microscopic behavior, but to describe the macroscopic quantities from a continuum mechanics point of view. In order to derive the wave propagation equations, the Lagrangian approach is then applied.

Main assumptions of the theory

Overall the following conditions are assumed:

- (a) the analysis is restricted to linear elastic deformations,
- (b) the solid structure is isotropic,
- (c) the fluid is inviscid and its stress distribution is hydrostatic,
- (d) the cells are open and the pore network is interconnected, i.e. each point from the fluid phase has a continuous path connecting it to every other,
- (e) all the processes are isothermal,
- (f) the studied wavelengths are larger than the characteristic size of the cells, such that scattering is neglected.

Stress-strain relations

Consider the displacements and strains in the solid and fluid phases to be the macroscopic averages of its microscopic values in a certain region, a representative elementary volume [Bachmat and Bear, 1987]. The solid phase can be conveniently described as $\rho^* \rho_s$, where ρ_s is the bulk solid material density and ρ^* is the relative density introduced in Eq. (1.1). Thus the fluid phase is given as $(1 - \rho^*) \rho_f$, where ρ_f is the density of the fluid. The stress tensor of the fluid phase in the presence of a hydrostatic pressure p_f can be written according to

Chapter 1. Introduction

assumption (c) as:

$$\sigma_{ij}^{(f)} = -(1 - \rho^*) p_f \delta_{ij}, \quad (1.3)$$

where δ_{ij} is the Kronecker delta with indices i, j corresponding to spatial coordinates x_1, x_2, x_3 .

The strain energy density function of every isotropic medium can be described in terms of the invariants of a corresponding strain tensor. Keeping in mind that fluid does not support any shear, the strain-energy per unit volume for a continuum with effective macroscopic parameters is postulated in the following form:

$$U = a_1 \theta_m^2 + a_2 d_m^2 + a_3 \theta_f^2 + a_4 \theta_m \theta_f. \quad (1.4)$$

Here $d_m = \varepsilon_{ij}^{(m)} - \frac{1}{3} \theta_m \delta_{ij}$ is the deviatoric part of the solid frame (matrix) strain tensor, and $\theta_p = \text{tr}(\varepsilon_{ij}^{(p)})$ is the volumetric part of the solid frame ($p = m$) and fluid ($p = f$) strain tensors. The coupling of both phases is captured by the last term of Eq. (1.4).

The macroscopic coefficients a_k can be found from static experiments: a pure shear test, a jacketed compressibility test, and an unjacketed compressibility test. These parameters are often unavailable analytically and require experimental determination [Chekkal et al., 2012, Gravade et al., 2012, Gueven et al., 2012]. For some specific configurations these parameters are listed in [Biot and Willis, 1957].

The stress-strain relations follow from Eq. (1.4):

$$\sigma_{ij}^{(m)} = \frac{\partial U}{\partial \varepsilon_{ij}^{(m)}}, \quad \sigma^{(f)} = \frac{\partial U}{\partial \theta_f}. \quad (1.5)$$

Equations of motion

The equations of motion can be obtained via Lagrange's equations once the kinetic energy T and potential energy U are defined. To find the kinetic energy, the macroscopic expression is postulated in terms of three parameters to be determined using volumetric averages of corresponding microscopic velocities.

The macroscopic form is postulated [Biot, 1956a]:

$$T = \frac{1}{2} V_b \left[\rho_{11} v_i^{(m)} v_i^{(m)} + 2\rho_{12} v_i^{(m)} v_i^{(f)} + \rho_{22} v_i^{(f)} v_i^{(f)} \right], \quad (1.6)$$

where the Einstein summation over the repeated indicies is used. Here $v_i^{(p)} = \dot{u}_i^{(p)}$ is the macroscopic velocity of corresponding phase (p) along the i^{th} spatial coordinate in a representative region V_b . The density constants ρ_{ab} are determined by the system parameters.

On the other hand, the kinetic energy in the microscopic formulation can be written as a combination of kinetic energies of the solid $V_m = V_b \rho^*$ and the fluid $V_f = V_b(1 - \rho^*)$ portions:

$$T = \frac{1}{2} \left[\int_{V_m} \rho_s w_i^{(m)} w_i^{(m)} dV + \int_{V_f} \rho_f w_i^{(f)} w_i^{(f)} dV \right], \quad (1.7)$$

where $w_i^{(p)}$ is the microscopic particle velocity. Homogenization implies the averaging of all microscopically defined values. The average of (Eq. (1.7)) assuming the portion densities to stay constant within V_b reads:

$$T = \frac{1}{2} \left[\rho_s V_m \langle w_i^{(m)} w_i^{(m)} \rangle_m + \rho_f V_f \langle w_i^{(f)} w_i^{(f)} \rangle_f \right], \quad (1.8)$$

with the usual notation $\langle . \rangle$ for volumetric average.

The equality of Eq. 1.6 and Eq. (1.8) yields:

$$\rho_{11} v_i^{(m)} v_i^{(m)} + 2\rho_{12} v_i^{(m)} v_i^{(f)} + \rho_{22} v_i^{(f)} v_i^{(f)} = \rho_s \rho^* \langle w_i^{(m)} w_i^{(m)} \rangle_m + \rho_f (1 - \rho^*) \langle w_i^{(f)} w_i^{(f)} \rangle_f. \quad (1.9)$$

Moreover, the condition of simultaneous motion of fluid and solid components in Eq. (1.9) leads to the definition of the average density $\bar{\rho}$ as:

$$\bar{\rho} = \rho^* \rho_s + (1 - \rho^*) \rho_f = \rho_{11} + 2\rho_{12} + \rho_{22}. \quad (1.10)$$

The macroscopic linear momentum, $\partial T / \partial v_i^{(p)}$, can be straightforwardly found by differentiating Eq. (1.6). Similarly, the microscopic linear momentum, $\partial T / \partial w_i^{(p)}$, is found from Eq. (1.8). Therefore the equality of both formulations leads to:

$$\rho_{11} + \rho_{12} = \rho^* \rho_s, \quad (1.11)$$

$$\rho_{12} + \rho_{22} = (1 - \rho^*) \rho_f. \quad (1.12)$$

Chapter 1. Introduction

Substituting Eqs. (1.11),(1.12) into Eq. (1.9) yields [Nelson, 1988]:

$$\rho_{12} = -\frac{\rho^* \rho_s (\langle w_i^{(m)} w_i^{(m)} \rangle_m - v_i^{(m)} v_i^{(m)}) - (1 - \rho^*) \rho_f (\langle w_i^{(f)} w_i^{(f)} \rangle_f - v_i^{(f)} v_i^{(f)})}{(v_i^{(f)} - v_i^{(m)})(v_i^{(f)} - v_i^{(m)}),} \quad (1.13)$$

which, for a nearly rigid matrix, can be simplified to:

$$\rho_{12} = -(1 - \rho^*) \rho_f (\tau - 1), \quad (1.14)$$

where τ is defined via the following ratio:

$$\tau = -\frac{\langle (w_i^{(f)} - v_i^{(m)})(w_i^{(f)} - v_i^{(m)}) \rangle_f}{(v_i^{(f)} - v_i^{(m)})(v_i^{(f)} - v_i^{(m)})}. \quad (1.15)$$

For the condition of a rigid frame Eq. (1.15) simplifies to:

$$\tau = \left(\frac{l}{L} \right)^2 \geq 1, \quad (1.16)$$

expressing the ratio of a curved path length l to the physical distance L between two points in the fluid, which clearly cannot be less than one. The parameter τ is known as the tortuosity, representing a degree to which the averaged path in the medium is curved (tortuous), a common tool to describe diffusion in porous media [Epstein, 1989]. Eq. (1.16) implies that the additional apparent density $\rho_{12} \leq 0$.

Following [Berryman, 1980], the total effective density of the solid moving in the fluid, ρ_{11} , can be expressed as:

$$\rho_{11} = \rho^* (\rho_s + r \rho_f), \quad (1.17)$$

where r can be found from a microscopic formulation for the frame moving in the fluid [Berryman, 1980]. Eq. (1.17) allows to update Eq. (1.15) as:

$$\tau = 1 + \left(\frac{\rho^*}{1 - \rho^*} \right) r. \quad (1.18)$$

Combining Eq. (1.17) and Eq. (1.18) yields:

$$\rho_{11} = \rho^* \rho_s + (1 - \rho^*) (\tau - 1) \rho_f. \quad (1.19)$$

The only remaining unknown coefficient ρ_{22} is derived by substituting Eq. (1.14) into Eq. (1.12):

$$\rho_{22} = (1 - \rho^*) \tau \rho_f. \quad (1.20)$$

Plugging Eq. (1.19), Eq. (1.14), and Eq. (1.20) into Eq. (1.6) allows finding the kinetic energy T .

The dynamic behavior of homogeneous systems in space can be specified by a Lagrangian density function \mathcal{L} , which is expressed in terms of generalized coordinates and their first time and space derivatives. In the present case, the macroscopic particle displacements $u_i^{(p)}$ are used as the generalized coordinates, which reads:

$$\mathcal{L} = \mathcal{L}\left(u_i^{(p)}, \dot{u}_i^{(p)}, \partial_j u_i^{(p)}\right) = T - U, \quad \text{where } \dot{u}_i^{(p)} = \frac{\partial u_i^{(p)}}{\partial t}, \quad \text{and } \partial_j u_i^{(p)} = \frac{\partial u_i^{(p)}}{\partial x_j} = \varepsilon_{ij}^{(p)}. \quad (1.21)$$

Hamilton's principle states that the variation of the integral of \mathcal{L} for any $\delta(u_i^{(p)})$ over the volume V_b vanishes (ch. 2.9 in [Achenbach, 2012]):

$$\delta \int_{t_1}^{t_2} \int_{V_b} \mathcal{L} dx_1 dx_2 dx_3 = 0. \quad (1.22)$$

The stationary Eq. (1.22) is equivalent to the following Euler equations of motion (ch. 3.1 in [Morse and Feshbach, 1953]):

$$\frac{\partial}{\partial t} \left(\frac{\partial \mathcal{L}}{\partial \dot{u}_i^{(p)}} \right) + \partial_j \left(\frac{\partial \mathcal{L}}{\partial (\partial_j u_i^{(p)})} \right) - \frac{\partial \mathcal{L}}{\partial u_i^{(p)}} = 0, \quad (1.23)$$

where the Einstein summation over the repeated indices is used.

Substitution of Eq. (1.21) into Eq. (1.23) yields:

$$\frac{\partial}{\partial t} \left(\frac{\partial T}{\partial v_i^{(p)}} \right) - \partial_j \left(\frac{\partial U}{\partial (\partial_j u_i^{(p)})} \right) = 0, \quad (1.24)$$

Notice that due to Eq. (1.6) the kinetic energy does not depend explicitly on displacements. Employing Eq. (1.5), the second term of Eq. (1.24) for (p)=(m) becomes:

$$\partial_j \left(\frac{\partial U}{\partial (\partial_j u_i^{(m)})} \right) = \partial_j \left(\frac{\partial U}{\partial \varepsilon_{ij}^{(m)}} \right) = \partial_j (\sigma_{ij}^{(m)}). \quad (1.25)$$

Chapter 1. Introduction

Similarly, in accordance with Eq. (1.3), (p)=(f) implies:

$$\partial_j \left(\frac{\partial U}{\partial (\partial_j u_i^{(f)})} \right) = \partial_j (\sigma_{ij}^{(f)}) = -(1 - \rho^*) \partial_i p_f. \quad (1.26)$$

The first term of Eq. (1.24) represents the generalized linear momentum per unit volume of a corresponding phase, which can be found from Eq. (1.6):

$$\frac{\partial T}{\partial v_i^{(m)}} = \rho_{11} v_i^{(m)} + \rho_{12} v_i^{(f)}, \quad (1.27)$$

$$\frac{\partial T}{\partial v_i^{(f)}} = \rho_{12} v_i^{(m)} + \rho_{22} v_i^{(f)}. \quad (1.28)$$

Combining Eqs. (1.25-1.28) and substituting it into Eq. (1.24), yields the following system of equations:

$$\partial_j \sigma_{ij}^{(m)} = \rho_{11} \ddot{u}_i^{(m)} + \rho_{12} \ddot{u}_i^{(f)}, \quad (1.29)$$

$$-(1 - \rho^*) \partial_i p_f = \rho_{12} \ddot{u}_i^{(m)} + \rho_{22} \ddot{u}_i^{(f)}. \quad (1.30)$$

These equations of motion are subjected to the plane harmonic wave analysis in the next section.

Elastic wave propagation

In infinite isotropic media, two types of waves can occur: longitudinal (pressure) and lateral (shear). The propagation characteristics of each wave type can be analyzed using the system of Eqs. (1.29, 1.30).

Pressure waves are considered first. The analysis can be conveniently done rewriting the equations of motion in terms of strain invariants. Taking the divergence from Eq. (1.29) yields:

$$\partial_i \partial_j \sigma_{ij}^{(m)} = \rho_{11} \ddot{\theta}_m + \rho_{12} \ddot{\theta}_f. \quad (1.31)$$

Notice that $\sigma_{ij}^{(m)}$ can be found from Eq. (1.5):

$$\sigma_{ij}^{(m)} = \frac{\partial U}{\partial \varepsilon_{ij}^{(m)}} = 2a_2 d_{ij}^{(m)} + (2a_1 \theta_m + a_3 \theta_f) \delta_{ij}. \quad (1.32)$$

Therefore, the left hand side of Eq. (1.31) can be expanded as:

$$\partial_i \partial_j \sigma_{ij}^{(m)} = 2a_2 \partial_i \partial_j \varepsilon_{ij}^{(m)} + 2(a_1 - \frac{1}{3} a_2) \partial_i \partial_i \theta_m + a_3 \partial_i \partial_i \theta_f. \quad (1.33)$$

Plugging Eq. (1.33) back into Eq. (1.29) and simplifying the tensor expressions leads to:

$$2(a_1 + \frac{2}{3} a_2) \partial_i \partial_i \theta_m + a_3 \partial_i \partial_i \theta_f = \rho_{11} \ddot{\theta}_m + \rho_{12} \ddot{\theta}_f. \quad (1.34)$$

Similarly, the divergence of Eq. (1.30) yields:

$$a_3 \partial_i \partial_i \theta_m + 2a_4 \partial_i \partial_i \theta_f = \rho_{12} \ddot{\theta}_m + \rho_{22} \ddot{\theta}_f. \quad (1.35)$$

Assuming plane harmonic waves with angular frequency ω and wavevector \mathbf{k} :

$$\boldsymbol{\theta} = \boldsymbol{\theta}_0(\mathbf{k}) e^{i\omega t}, \quad (1.36)$$

or in a vector form:

$$\begin{Bmatrix} \theta_m(\mathbf{k}) \\ \theta_f(\mathbf{k}) \end{Bmatrix} = \begin{Bmatrix} \theta_m^{(0)}(\mathbf{k}) \\ \theta_f^{(0)}(\mathbf{k}) \end{Bmatrix} e^{i\omega t}, \quad (1.37)$$

Eqs. (1.34,1.35) are reduced to the eigenvalue problem:

$$[\mathbf{B} - c_p^2 \mathbf{D}] \cdot \boldsymbol{\theta}_0 = \mathbf{0}, \quad (1.38)$$

where:

$$\mathbf{B} = \begin{bmatrix} 2(a_1 + \frac{2}{3} a_2) & a_3 \\ a_3 & 2a_4 \end{bmatrix}, \quad \mathbf{D} = \begin{bmatrix} \rho_{11} & \rho_{12} \\ \rho_{12} & \rho_{22} \end{bmatrix}. \quad (1.39)$$

Two eigenvalues $c_p = \omega / \|\mathbf{k}\|$ are the phase velocities of a slow and fast pressure waves.

A similar approach can be used to obtain the velocity of the shear wave. Taking the curl of the sum of Eqs. (1.29, 1.30) under the assumption of plane harmonic waves, the phase velocity of

shear waves in the low-frequency regime is [Biot, 1956a, Carcione, 2007]:

$$c_S = \sqrt{\frac{a_2}{\bar{\rho} - \rho_f(1 - \rho^*)\tau^{-1}}} = \sqrt{\frac{a_2}{\rho_s\rho^* + \rho_f(1 - \rho^*)(1 - \tau^{-1})}}. \quad (1.40)$$

These results are of great importance to describe the dynamic properties of open cell porous materials in which two pressure and one shear waves exist. These waves are well studied numerically [Carcione and Quiroga-Goode, 1995, Göransson, 1998] and experimentally [Gurevich et al., 1999, Smeulders and Van Dongen, 1997]. However, due to the initial assumptions, and the introduction of tortuosity, the theory is not applicable to the dynamics of closed-cell media. A major question arises as to what happens in this limit case of $\tau \rightarrow \infty$, when the inter-cell coupling becomes determined only by deformations of structure as a complex function of solid and fluid interaction. Moreover, under these conditions, scattering cannot be neglected anymore since the interfacial walls and cavities may resonate introducing a strong dispersion to the system, which naturally yields the analysis to the class of locally resonant metamaterials.

1.4 Motivation and objectives of the thesis

Until now, the concept of acoustic metamaterials is closely associated with their optical counterpart, as they were developed mainly to mimic electromagnetic outcomes. Therefore, the numeric and experimental results are rather scattered, and the proposed substructures are often complex and too expensive for real-life applications. It would be of scientific interest to extend this stand-alone field to existing material classes with a regular architecture, taking advantage of their well-developed theories.

Biot's theory for saturated porous media should enable us to validate it from an acoustic metamaterials point of view. A similar material class - although it does not fulfill some of Biot's assumptions - are fluid filled cellular materials. Considering a periodic cellular solid could allow a significant simplification of the current concept of acoustic metamaterials. This work investigates a closed-cell cellular solid with entrained fluid and soft vibrating walls within the metamaterial framework. Such a system contains local resonators (the vibrating walls), and could therefore find a wide application due its low cost, simplicity, versatility in terms of scalability, and ability to design desired dynamic macroscopic behavior using different types of fluids and bulk materials. Unit cells in natural cellular solids range from the micrometer to centimeter scale. Regular man-made structures can be established within the same limits.

This material class therefore provides an excellent outlook for applications from audible frequencies to ultrasound. On the whole, there are four objectives of the current work:

- Develop a numerical model for the dynamics of a closed-cell cellular solid with entrained fluid, using periodic boundary conditions, to describe the propagation of an elastic wave explicitly considering the interaction of fluid and structure.
- Analyze the physics of the concept from an acoustic metamaterial point of view, i.e. to consider its phononic properties with homogenized and fully analytical models.
- Extend Biot's theory of saturated porous media in the context of a closed cell cellular solid subjected to acoustic wave analysis.
- Confirm experimentally the proposed numerical and analytical models.

1.5 Organization of the work

The framework of the thesis follows the objectives listed above using the following structure. In Chapter 2, the numerical model for wave propagation in cellular and porous solids with entrained fluid is introduced. The results are compared to Biot's theory, described in Sec. 1.3.2, in terms of the phase velocity of pressure and shear waves.

In Chapter 3, the pressure waves are analyzed. Identifying the key parameters for the propagation characteristics allows the derivation of effective mechanical models. Based on proposed homogenized models the effective stiffness tensor of an equivalent continuum at the macroscale is introduced. The analysis of dispersion surfaces is provided to indicate a single isotropic pressure mode for frequencies below resonance of the lattice walls, unlike Biot's theory which predicts two pressure modes. The dependence of the solid and fluid phases on the relative density and mass coupling is discussed via the microstructural deformations.

Chapter 4 describes the propagation of pressure waves analytically. Based on the vibration analysis of loaded beams, all numerically predicted longitudinal waves are identified within the studied frequency range. The analytical dispersion relation is compared to the full finite-element solution. Furthermore, the co-existence of a slow and fast wave is proved using Rayleigh's energy approach.

Finally, in Chapter 5, an experimental proof-of-concept is given to validate the analytical and numerical models for shear waves. This is done in three steps. First, the wavemode shapes pertaining to the first three shear waves are analyzed with a steady-state analysis. Then, the

Chapter 1. Introduction

numerical estimation of the group velocity is compared to experimental results. The analysis of the partial bandgaps exhibited by the system concludes the thesis.

2 Numerical Model of a 2D Square Lattice With Entrained Fluid

The chapter is mainly reprinted from [Dorodnitsyn and Spadoni, 2014a] with authorization of the publisher.

2.1 Introduction

The elasto-dynamics of cellular materials present a number of unique phenomena not found in solid, single-phase materials. In the long-wavelength, low-frequency regime, cellular materials behave as effective solids, with high mass-specific stiffness, whose quasi-static behavior can be described by homogenized models [Gibson and Ashby, 1999, Kumar and McDowell, 2004, Spadoni and Ruzzene, 2011]. The effective stiffness tensor derived from the static-deformation mechanism of the microstructure is sufficient to describe the propagation of linear-elastic waves [Eringen, 2001, Gonella and Ruzzene, 2008b, Martinsson and Movchan, 2003, Phani et al., 2006, Suiker et al., 2001]. Depending on the employed theory, various wave-modes are found for an infinite medium: pressure and shear waves from classical elasticity theory [Gonella and Ruzzene, 2008b, Phani et al., 2006], and additional rotational and coupled modes from micro-continuum theories [Eringen, 2001, Martinsson and Movchan, 2003, Suiker et al., 2001]. In the low-frequency regime, the anisotropy of the stiffness tensor is determined purely by geometric symmetries of the microstructure [Gibson and Ashby, 1999, Kumar and McDowell, 2004]. For frequency regimes above resonance of internal components, cellular materials present numerous unusual phenomena. Band gaps [Gonella and Ruzzene, 2008a, Martinsson and Movchan, 2003, Mead, 1996, Phani et al., 2006, Spadoni et al., 2009], frequency regimes with evanescent waves, resonance-induced anisotropy [Casadei and Rimoli, 2013, Spadoni et al., 2009], wave-beaming [Ruzzene et al., 2003], and caustics [Spadoni et al., 2009] are characteristic of this regime. Stiff inclusions [Liu et al., 2011b] and hierarchical struc-

Chapter 2. Numerical Model of a 2D Square Lattice With Entrained Fluid

ture [Martinsson and Movchan, 2003, Xu et al., 2012] enhance the unusual characteristics of the resonant regime.

Less is known about elastic wave propagation in cellular solids with closed cells, and this remains a topic of active research. In the case of porous solids with entrained fluid, wave propagation is described by Biot's theory [Allard and Atalla, 2009, Biot, 1956a, Carcione, 2007] derived from a strain-energy functional defined at the macroscale, based on averaged microstructural quantities. The theoretical bridging between micro and macroscales in Biot's theory has since been validated with rigorous micromechanical models [Auriault and Sanchez-Palencia, 1977, Burrige and Keller, 1981, Cheng, 1997, Chevillotte et al., 2010, Dormieux et al., 2002, Perrot et al., 2008a, Thompson and Willis, 1991]. Biot's theory, discussed in Sec. 1.3.2, however requires the mechanical properties of the solid matrix for both drained and undrained conditions, but these are often not available, and comparisons with specific configurations are based on experiments [Chekkal et al., 2012, Gueven et al., 2012]. Parameters describing the coupling between solid and fluid phases, such as the tortuosity for example, are still topics of active research [Chekkal et al., 2012, Gueven et al., 2012]. Porous solids moreover are distinguished from cellular solids based on their relative density $\rho^* = V_s/V$ (Eq. 1.1) or the porosity $\phi = V_f/V$ where $V = V_s + V_f$, and V_s , V_f are the volumes occupied by the solid and fluid phases respectively. Cellular solids are defined by $\rho^* < 0.3$ [Gibson and Ashby, 1999]. Biot's theory predicts three bulk-wave modes: two pressure modes and a shear mode, but it is not clear if these findings extend to cellular solids for which $\rho^* \rightarrow 0$ ($\phi \rightarrow 1$).

In this chapter, we analyze elastic-wave propagation in a cellular solid with closed cells and entrained compressible fluid, for which mechanical properties in drained conditions are known analytically. We employ a periodic square lattice as a prototypical two-phase medium to explore the applicability of Biot's theory for low relative density $\rho^* \rightarrow 0$. We also investigate high frequency regimes where the spectrum of elastic waves may include resonant frequencies of the fluid cavities. We employ finite-element (FE) analysis, detailed in Sec. 2.2, which explicitly considers the direct coupling of fluid and structural dynamics. In Sec. 2.3, we discuss wave-propagation characteristics and sources of dispersion for a cellular solid with slender internal components of aspect ratio 0.01 and relative density $\rho^* = 0.04$. In Sec. 2.4, we compare Biot's theory for plane 2D conditions (introduced previously in Sec. 1.3.2) to homogenized models obtained for drained conditions and computational results for varying relative density $0.0001 \leq \rho^* \leq 1$. We find excellent agreement between computational models and Biot's theory for pressure and shear wave velocities for almost the entire ρ^* range. We also show that in the limit of $\rho^* \rightarrow 1$, homogenized models for drained cellular solids and Biot's theory overestimate

the velocities of shear and pressure waves.

2.2 Lattice Geometry and Computational Models

In the current work, we consider elastic wave propagation in an infinite-periodic cellular medium with fluid-filled, closed cavities. As a result, we restrict ourselves to analyzing the dynamics of a representative volume element (RVE) composed of both solid and fluid phases, and with appropriate symmetry conditions.

2.2.1 Square-lattice geometry and RVE

We consider the fluid-filled square lattice in plane conditions shown in Fig. 2.1 defined in the basis $(\mathbf{i}_1, \mathbf{i}_2)$. The out-of-plane thickness is unity, while the RVE (shown in Fig. 2.2) is defined by characteristic length L and wall thickness $h/2$. The lattice vectors $\mathbf{e}_1 = L\mathbf{i}_1$, $\mathbf{e}_2 = L\mathbf{i}_2$ define the periodicity of an infinite medium. The relative density ρ^* and porosity ϕ are defined as:

$$\rho^* = 2\frac{h}{L} - \left(\frac{h}{L}\right)^2 = 1 - \phi. \quad (2.1)$$

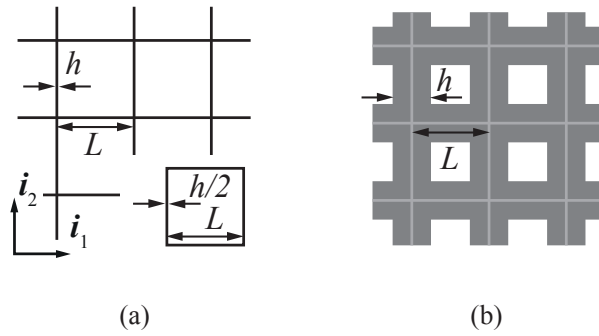


Figure 2.1 – Square lattice with walls thickness h and cell length L with (a) $\rho^* < 0.3$ and (b) $\rho^* > 0.3$. The superposed unit cell in (a) has thickness $h/2$.

In order to explore the range of applicability of Biot's theory and analyze wave propagation for $\rho^* \rightarrow 0$, we consider two computational models based on the finite-element method: (i) cell walls discretized with Euler-Bernoulli beam elements to explore $h, \rho^* \rightarrow 0$ and (ii) cell walls discretized with 2D plane-elements for large ρ^* . We employ the beam model for configurations with very thin walls, which would require very small plane elements to maintain a reasonable aspect ratio.

2.2.2 RVE discretization

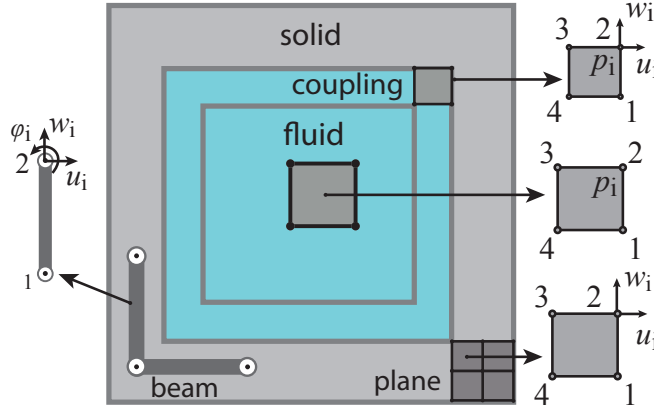


Figure 2.2 – Discretized RVE: beam and 4-node plane elements are shown with appropriate degrees of freedom. In both cases, coupling elements with both structural and pressure degrees of freedom enforce fluid-structure interaction.

In the case (i) of beam elements of Fig. 2.2, we only account for stress distribution along L resulting from both transverse $w(x_l)$ and axial $u(x_l)$ displacements, where x_l is the local coordinate along L . Then, the strain energy of the beam, which is employed to discretize the walls of the cell is, accordingly [Cook, 2001]:

$$U_b = \int_0^L \left[E_s I_{33} \left(\frac{\partial^2 w(x_l, t)}{\partial x_l^2} \right)^2 + E_s A \left(\frac{\partial u(x_l, t)}{\partial x_l} \right)^2 \right] dx_l, \quad (2.2)$$

where E_s is the Young's modulus of the walls material, A is the wall cross-sectional area, and I_{33} is the area-moment of inertia. The corresponding kinetic energy is:

$$T_b = \int_0^L \rho_s A \left[\left(\frac{\partial w(x_l, t)}{\partial t} \right)^2 + \left(\frac{\partial u(x_l, t)}{\partial t} \right)^2 \right] dx_l, \quad (2.3)$$

where ρ_s is the density of the wall material. This discretization notably omits shear stress within the walls, and the contribution of Poisson's effects. The work done by the fluid pressure is:

$$W_b = \int_0^L p(x_l, t) w(x_l, t) dx_l, \quad (2.4)$$

where p is the pressure exerted on the structure by the fluid. In order to preserve the bending stiffness of the actual cell walls, the beam discretization for the RVE considers the thickness $h/2$ to be doubled to correctly account for the mass of the RVE in Eq. (2.3) upon enforcing

2.2. Lattice Geometry and Computational Models

symmetry conditions (discussed in Sec. 2.2.3). The total energy in the case of beam elements is simply $\Pi_b = U_b + T_b - W_b$.

In the case (ii) of 2D plane elements, we use the displacement formulation [Cook, 2001] which accounts for in-plane displacement components $u(x_l, y_l)$, $w(x_l, y_l)$ in the local element coordinates (x_l, y_l) and plane-strain conditions. We use a formulation known as QM6 [Cook, 2001] to ameliorate shear locking and spurious behavior. The total energy in each element is:

$$\Pi_s = \frac{1}{2} \int_{\Omega_s} \boldsymbol{\varepsilon}^T \boldsymbol{\sigma} d\Omega_s + \frac{1}{2} \int_{\Omega_s} \rho_s \dot{\mathbf{u}}^2 d\Omega_s - \int_{\partial\Omega_s} p \mathbf{u} d\partial\Omega_s, \quad (2.5)$$

where $\boldsymbol{\varepsilon} = \{\varepsilon_{11}, \varepsilon_{22}, 2\varepsilon_{12}\}^T$ is the solid strain tensor, $\boldsymbol{\sigma} = \{\sigma_{11}, \sigma_{22}, \sigma_{12}\}^T$ is the solid Cauchy stress tensor, $\mathbf{u} = \{u, w\}^T$ is the global displacement vector, and Ω_s is the element area.

We neglect convection (quiescent conditions) and we consider the fluid phase as inviscid so that pressure in the cavities is governed by the wave equation:

$$\nabla^2 p = \frac{1}{c_0^2} \frac{\partial^2 p}{\partial t^2} \quad (2.6)$$

with boundary conditions:

$$\frac{\partial p}{\partial \mathbf{n}} = -\rho \ddot{\mathbf{u}}_n, \quad (2.7)$$

where $c_0 = \sqrt{B_f/\rho_f}$ is the speed of sound in the fluid, $B_f = -p/(dV/V)$ is the bulk modulus, and \mathbf{n} is a unit normal vector outward from the fluid boundary. Accordingly, the total energy in the fluid is [Cook, 2001]:

$$\Pi_f = \int_{\Omega_f} \frac{1}{2} \left[\left(\frac{\partial p}{\partial x} \right)^2 + \left(\frac{\partial p}{\partial y} \right)^2 + \left(\frac{\partial p}{\partial z} \right)^2 + \frac{2}{c_0^2} p \ddot{p} \right] d\Omega_f + \int_{\partial\Omega_f} \rho_f \ddot{\mathbf{u}}_n p d\partial\Omega_f, \quad (2.8)$$

where the last term denotes the work done by applied pressure due to acceleration of the cavity walls. The fluid region is discretized with quadrilateral plane elements [Cook, 2001] with area $\partial\Omega_f$. Enforcing that the total energy in the solid Π_s (or Π_b) and in the fluid Π_f are at a minimum, one obtains:

$$\begin{bmatrix} M_s & 0 \\ \rho_f S & M_f \end{bmatrix} \begin{Bmatrix} \ddot{\mathbf{u}} \\ \ddot{\mathbf{p}} \end{Bmatrix} + \begin{bmatrix} K_s & -S^T \\ 0 & K_f \end{bmatrix} \begin{Bmatrix} \mathbf{u} \\ \mathbf{p} \end{Bmatrix} = \begin{Bmatrix} \mathbf{F}_{ext} \\ \mathbf{0} \end{Bmatrix}, \quad (2.9)$$

where \mathbf{F}_{ext} is the vector of external forces acting on the structure, \mathbf{u} and \mathbf{p} are the global nodal displacement and pressure arrays. The matrix [S] defines the asymmetric fluid-structure

interaction:

$$\mathbf{R}_f = \rho_f [S] \ddot{\mathbf{u}}, \quad \mathbf{R}_s = [S]^T \mathbf{p}, \quad (2.10)$$

where vectors \mathbf{R}_f and \mathbf{R}_s are the nodal loads acting on the structure and fluid respectively. $[K_s]$, $[K_f]$, $[M_s]$, $[M_f]$ are the fluid and structural element matrices.

2.2.3 RVE analysis of plane harmonic waves

We are interested in the propagation of plane, harmonic waves in a periodic medium of infinite extent; this can be analyzed considering the governing equations of motion for an appropriate RVE with symmetry conditions provided by Bloch's theorem [Kittel, 2004]. Bloch's theorem states that for an infinite medium with repetitive identical units, the evolution of waves across cells does not depend on cell location within the periodic system, and can be fully identified through the analysis of the RVE (Fig. 2.2).

The entire lattice-point system with a basis is referred to as a direct lattice and is obtained by translation of the RVE by the basis vectors ($\mathbf{i}_1, \mathbf{i}_2$) (Fig. 2.3(a)). It can be shown that linear plane waves in such media have spatially-periodic solution [Brillouin, 2003] and only a subset of wavevector space is required to obtain the full solution. This wavevector subspace is most easily expressed in the reciprocal-lattice space (k -space), which is determined by $\mathbf{i}_j^* \cdot \mathbf{i}_k = 2\pi\delta_{jk}$, where \mathbf{i}_j^* are the basis vectors of the reciprocal lattice (Fig. 2.3(a)). The wavevector subspace defined in the basis \mathbf{i}_j^* is known as the first Brillouin Zone which can be further reduced by symmetry arguments. The result is the irreducible Brillouin Zone (iBZ), the contour of which provides information about maximum diffraction along high symmetry directions [Brillouin, 2003]. The size of the Brillouin zone is defined to exhibit all the wavevector combinations with the wavelengths larger than the characteristic interunit distance. The symmetry points, which define the iBZ in the nondimensional wavevector space for the given lattice, form a triangle with the vertices positioned at $\Gamma = (0, 0)$, $X = (\pi, 0)$, $M = (\pi, \pi)$ shown in Fig. 2.3(a). The long-wavelength limit corresponds to the origin of first Brillouin Zone denoted by Γ . Paths $\Gamma - X$ and $X - M$ represent the waves traveling in directions \mathbf{i}_1 and \mathbf{i}_2 respectively, while path $\Gamma - M$ describes waves with 45° orientation in direct space.

Assuming a plane harmonic wave with frequency ω , amplitude $\hat{\mathbf{u}}$, and position vector \mathbf{r} , one has:

$$\mathbf{u}(\mathbf{r}, t) = \hat{\mathbf{u}} e^{i(\mathbf{k} \cdot \mathbf{r} - \omega t)} = \hat{\mathbf{u}}(k) e^{i\omega t}, \quad (2.11)$$

2.2. Lattice Geometry and Computational Models

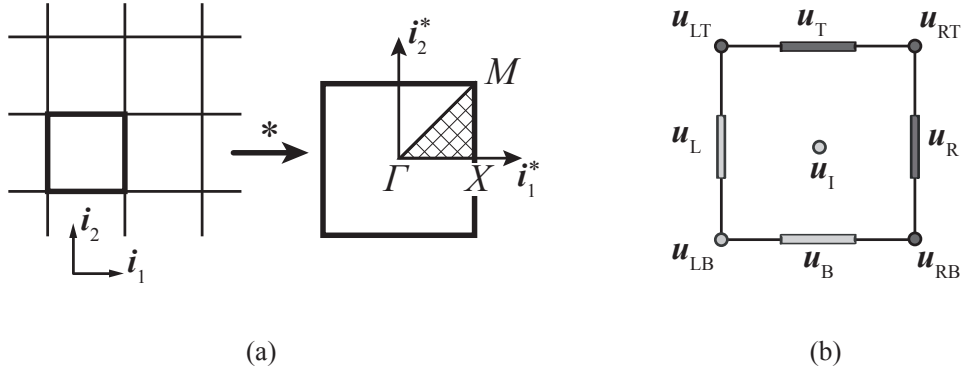


Figure 2.3 – Transformation (a) from direct $(\mathbf{i}_1, \mathbf{i}_2)$ to reciprocal basis $(\mathbf{i}_1^*, \mathbf{i}_2^*)$ with first and irreducible Brillouin zones with symmetry points $\Gamma = (0, 0)$, $X = (\pi, 0)$, $M = (\pi, \pi)$. RVE (b) with associated master (light gray) and slave (dark gray) degrees of freedom.

where $i^2 = -1$. Given the lattice is infinite, we take the wavevector $\mathbf{k} = k_1 \mathbf{i}_1 + k_2 \mathbf{i}_2$ to be real, and we neglect attenuation. According to Bloch's theorem, the displacement of the point corresponding to P at location $\boldsymbol{\rho}_P = \mathbf{r} + n_1 \mathbf{i}_1 + n_2 \mathbf{i}_2$, where n_1, n_2 are integer numbers, can be written in terms of the displacement of the reference unit cell as:

$$\mathbf{u}(\boldsymbol{\rho}_P, t) = \mathbf{u}(\mathbf{r}, t) e^{i(n_1 k_x + n_2 k_y)}, \quad (2.12)$$

where $k_x = \mathbf{k} \cdot \mathbf{i}_1$ and $k_y = \mathbf{k} \cdot \mathbf{i}_2$. The same property can be used to define symmetry conditions for the RVE: by denoting top, bottom, left, right, and internal regions with subscripts $(\)_T$, $(\)_B$, $(\)_L$, $(\)_R$, and $(\)_I$ (refer to Fig. 2.3b), the following conditions hold for vectors of nodal displacements \mathbf{u} and nodal forces \mathbf{f} [Mead, 1996]:

$$\begin{aligned} \mathbf{u}_{RB} &= e^{ik_x} \mathbf{u}_{LB}, \quad \mathbf{u}_R = e^{ik_x} \mathbf{u}_L, \\ \mathbf{u}_{LT} &= e^{ik_y} \mathbf{u}_{LB}, \quad \mathbf{u}_T = e^{ik_y} \mathbf{u}_B, \quad \mathbf{u}_{RT} = e^{i(k_x + k_y)} \mathbf{u}_{LB}, \\ \mathbf{f}_R &= -e^{ik_x} \mathbf{f}_L, \quad \mathbf{f}_T = -e^{ik_y} \mathbf{f}_B, \\ \mathbf{f}_{RT} + e^{ik_x} \mathbf{f}_{LT} + e^{ik_y} \mathbf{f}_{RB} + e^{i(k_x + k_y)} \mathbf{f}_{LB} &= 0. \end{aligned} \quad (2.13)$$

Denoting $\mathbf{u}_r = \{u_{LB}, u_L, u_B, u_I\}^T$ as the reduced degree of freedom (DOF) vector containing only master DOFs, its relation to the vector \mathbf{u} is:

$$\mathbf{u} = [T] \mathbf{u}_r, \quad (2.14)$$

with $[T]$ expressing the symmetry conditions of Eq. (2.13). Symmetry conditions can be

enforced as:

$$[T]^T ([K^*] - \omega^2 [M^*]) [T] \hat{\mathbf{u}}_r = [T]^T \mathbf{f} = \mathbf{0}, \quad (2.15)$$

where $[M^*]$ and $[K^*]$ denote the coupled mass and stiffness matrices from the Eq. (2.9) respectively. Eq. (2.15) constitutes a generalized eigenvalue problem:

$$([K_r](\mathbf{k}) - \omega^2 [M_r](\mathbf{k})) \hat{\mathbf{u}}_r = \mathbf{0}, \quad (2.16)$$

which relates the frequency ω to the wavevector \mathbf{k} . For \mathbf{k} restricted to the boundaries of the irreducible Brillouin zone, one obtains the band structure providing the dispersion relation for each wavemode.

2.3 Wave propagation in a Two-phase Square Lattice

2.3.1 Band structure and wavemodes

In this chapter, we consider a square lattice defined by solid density $\rho_s = 1000 \text{ kg/m}^3$, solid Young's modulus $E_s = 1000 \text{ Pa}$ and Poisson's ratio $\nu_s = 0.46$, wall length $L = 100 \text{ }\mu\text{m}$, and wall thickness $10 \text{ nm} \leq h \leq 100 \text{ }\mu\text{m}$. In this section we consider the fluid phase to be air with bulk modulus $B_f = 142 \text{ kPa}$ and density $\rho_f = 1.2 \text{ kg/m}^3$, unless noted otherwise. The band structure for a square lattice defined by $\rho^* = 0.04$ is shown in Fig. 2.4, where dash lines denote the solution to the structure-only configuration (FE model neglecting pressure DOFs, only considering the first of Eq. (2.9), and neglecting $[S]$), in agreement with previous studies [Phani et al., 2006], while solid lines denote the solution to the fluid-structure-interaction (FSI) case. The corresponding wavemodes are shown in Fig. 2.5. For both configurations, we use two normalized frequencies in Fig. 2.4: on the left ordinate $\bar{\omega} = \omega/\omega_0$, where $\omega_0 = 4.73^2 \sqrt{E_s I / (\rho_s A^* L^4)}$ is the first natural frequency of a clamped-clamped beam (A is the cross-sectional area of the wall of the cell, and I is the area moment of inertia) and on the right ordinate $\hat{\omega} = \omega/\omega_c$, where ω_c is the first natural frequency of the fluid cavity alone. Given the nonlinearity of the band structure near $\omega/\omega_0 = 1$, strong dispersion in this frequency regime is the result of resonances of the lattice structure. The frequency range considered in Fig. 2.4 is well below the first natural frequency of the fluid cavity.

The first difference between the two solutions is the presence of a high-speed, longitudinal wavemode for the FSI configuration for $0 \leq \bar{\omega} \leq 1$. This indicates that the propagation of pressure (longitudinal) waves is strongly affected by the presence of entrained fluid (discussed

2.3. Wave propagation in a Two-phase Square Lattice

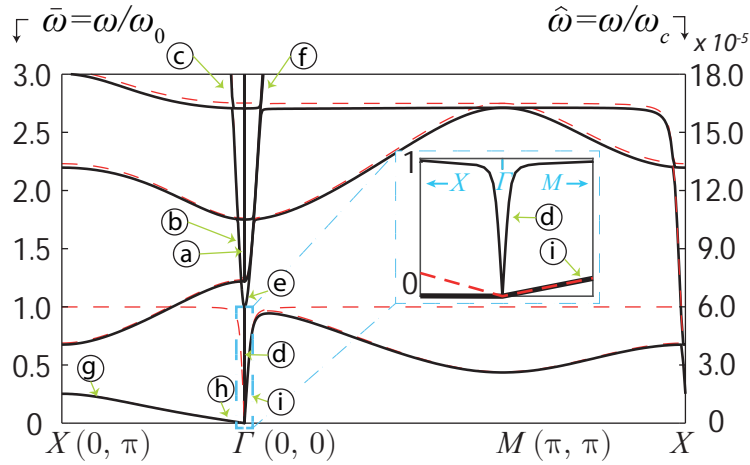


Figure 2.4 – Band structure for RVE with $h/L = 0.02$, $\rho^* = 0.04$ discretized with beam elements for the irreducible Brillouin Zone with high-symmetry points Γ , X , M . Left ordinate is normalized by the first natural frequency of a clamped-clamped beam, ω_0 ; the second ordinate is normalized by the first natural frequency of the fluid cavity alone, ω_c . Solid lines are the solution to the coupled problem (FSI), dashed lines are the solution to the structure-only case. Zoomed region around Γ -location is in blue dashed inset. Circled letters (a)-(i) denote wavenumber combinations used to depict deformed configurations in Fig. 2.5

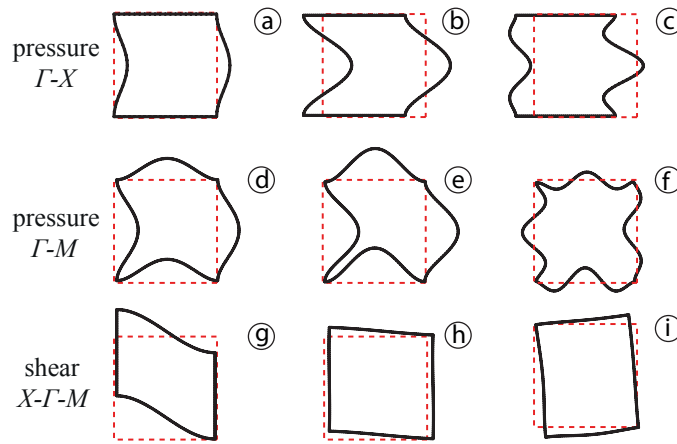


Figure 2.5 – Fluid-structure (FSI) wavemodes corresponding to the wavenumber combinations indicated by the labels (a-i) in Fig. 2.4. Solid lines denote the deformed configuration while dashed lines denote the initial configuration.

in detail in Sec. 2.4). The deformed configuration of this mode are identical to that shown in Fig. 2.5(a). Beyond the first natural frequency of internal members, ($\bar{\omega} > 1.25$), two dispersive pressure modes are present: a fast and a slow mode. Although their deformation is nearly identical, the fast mode has fluid and structure displacing in phase, while for the slow mode

Chapter 2. Numerical Model of a 2D Square Lattice With Entrained Fluid

fluid and structure displace out of phase (Figs. 2.5(a,b) for $\Gamma - X$ direction or $k_x \in [0, \pi]$ and $k_y = 0$). In addition to displacement phase of solid and fluid components, the difference between the two pressure modes is their phase and group velocity. This is in agreement with Biot's theory [Carcione, 2007], which predicts a fast and a slow pressure mode, albeit in our case, this happens above the first natural frequency of lattice members (clamped-clamped beam). Similar conclusions can be drawn for plane waves propagating in the $\Gamma - M$ direction ($k_x = k_y \in [0, \pi]$), although in this case all four sides of the RVE deflect (Figs. 2.5(d-f)). For frequencies $\hat{\omega} > 3$, the fast and slow pressure modes are characterized by a combination of first and third mode shapes for a clamped-clamped beam (Fig. 2.5(c)). We do not find any wavemodes characterized by even mode shapes of clamped-clamped beams as a result of nearly-hydrostatic pressure loading below the first natural frequency of the fluid cavity ($\hat{\omega} < 1$).

An additional feature of the band structure in Fig. 2.4 is the fact that shear modes are not affected by the entrained fluid for frequencies $\hat{\omega} < 1$. The structure-only and FSI solutions in fact overlap if the entrained fluid does not contribute significant mass, as for the case of air considered here. Typical deformed configurations are shown in Figs. 2.5(g-i). These wavemodes are equivoluminal and thus are not affected by the presence of fluid beyond added-mass effects. This is in agreement with the assumption of inviscid entrained fluid, but does not hold for $\hat{\omega} > 1$ (discussed in Sec. 3.3). The branch denoted by label (i) in Figs. 2.4 and 2.5 is a hybrid pressure-shear mode for the FSI configuration, while it is a pure shear mode for the structure-only case.

Results obtained with the plane-element, FE model in Fig. 2.6(a) for the same geometric and material parameters are in agreement with those of Fig. 2.4 (superposed in Fig. 2.6(a) with blue dotted lines) albeit with a small reduction in the predicted frequencies. This is to be attributed to the naturally-deformable joints between sections of the unit cell, compared to rigid joints in the case of beam elements. The agreement between Figs. 2.4 and 2.6(a) is encouraging as we will employ the plane-element model to investigate wave propagation in configurations with both thin and thick walls in Sec. 2.4. The contribution of added mass by the entrained fluid affects both shear and pressure wavemodes. In Fig. 2.6(b), we superpose the first shear mode in the $\Gamma - X$ direction computed for entrained air and for entrained water ($\rho_f = 1000 \text{ kg/m}^3$, $B_f = 2 \text{ GPa}$). For the same structural parameters (discussed in the next section), water naturally leads to a slower shear mode.

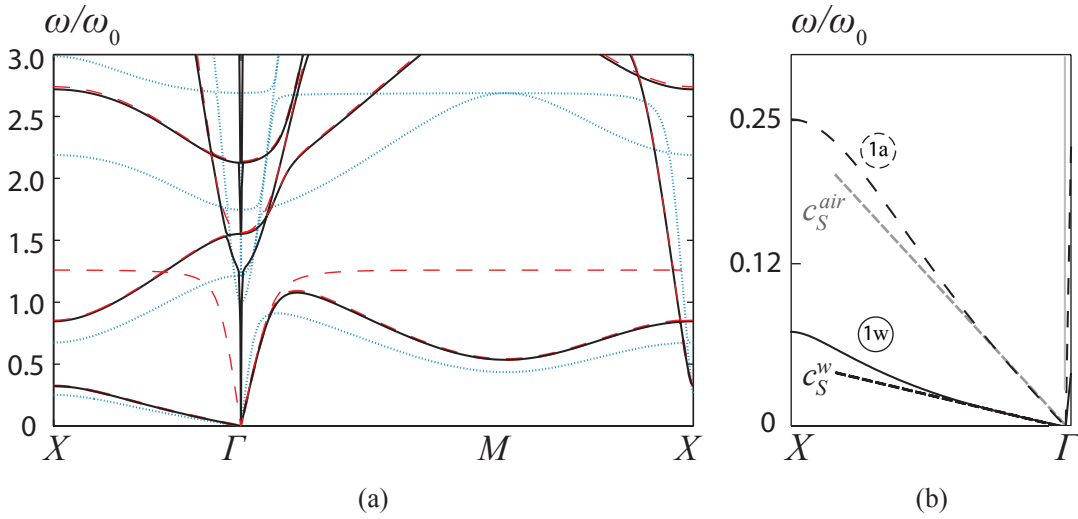


Figure 2.6 – Band structure (a) for the same parameters as Fig. 2.4, computed with plane elements. Solid lines are the solution to the FSI configuration, dashed are the solution to the structure-only configurations. The FSI configuration computed with beam elements (Fig. 2.4) is superposed with the blue dotted lines. Superposition of FSI band structures (b) with entrained air (1a) and water (1w) with detail view of first shear wavenode. Homogenized phase velocities denoted as c_S^{air} and c_S^w for air and water respectively.

2.3.2 Dispersion source analysis

The structural lattice we investigate here is characterized by internal components with resonances within the frequency range of interest. Strong dispersion indeed coincides with the first natural frequency of a clamped-clamped beam (Figs. 2.4 and 2.6(a)). An analysis of the contribution of resonant frequencies of structure and cavity is in order. In Fig. 2.7(a) we superpose the band structure of configuration FSI, for the parameters of Sec. 2.3, and the first four natural frequencies of clamped-clamped beam. We conclude that, in addition to Bragg scattering from wavelengths comparable to L , resonance of the lattice components indeed is a strong source of dispersion. The fast pressure mode is only affected by odd modes of the lattice ligaments, in agreement with the pressure loading imparted by the fluid. For propagation in the $\Gamma - X$ direction, the horizontal walls are undeformed (Fig. 2.5(a-b)) as this guarantees minimum energy in the RVE. Shear wavenodes on the other hand are affected by all resonances of the lattice components. The same behavior is exhibited by the plane elements model.

The cavity resonant frequencies for air are much higher ($\omega_c/\omega_0 = 1.7 \times 10^4$) than the considered frequencies in Figs. 2.4, 2.6(a), and 2.7(a) and they do not contribute any dispersion. However, if one reduces the cavity resonances (for example, by changing bulk modulus, or by changing

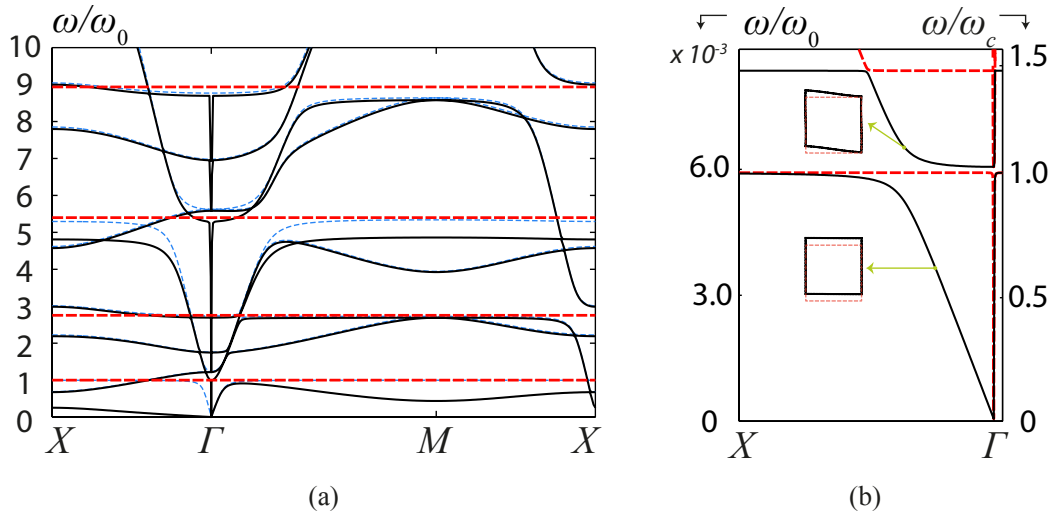


Figure 2.7 – Band structure (beam elements) for the FSI configuration (a) for the same parameters as Fig. 2.4 in solid black lines with the first four natural frequencies of a clamped-clamped beam superposed as dashed red lines. The ordinate is normalized by ω_0 . Blue dashed lines are the solution to the structure-only case. Band structure (beam elements) and mode shapes for the FSI configuration (b) for entrained fluid with $B_f = 1.42 \cdot 10^{-7}$ Pa and $\rho_f = 1.2$ kg/m³ with $\hat{\omega} = \omega/\omega_c$ on the ordinate. Solid black lines are shear modes while dashed red lines denote the fast pressure modes.

the geometry of the structure) the fluid will also affect shear modes owing to strong pressure gradients. In Fig. 2.7(b), we show the $\Gamma - X$ portion of the band structure for an entrained fluid with $B_f = 1.42 \cdot 10^{-7}$ Pa, and $\rho_f = 1.2$ kg/m³. In this case, both shear and pressure waves are dispersed by resonances of the cavity, which couple efficiently with all mode shapes of the lattice components. The dynamic stiffness of the cavity moreover is at a minimum near resonances inducing phase changes between fluid and structural response.

2.4 Micro-Mechanical Pore Models and Comparison with FE Analyses

Section 2.3 is devoted to the analysis of configurations with $\rho^* = 0.04$ ($L/h = 100$) for which the lattice structure can be correctly modeled with either beam or plane elements. However, with increasing walls thickness h and aspect ratio of beam elements, beam theory becomes unreliable and we employ quadrilateral plane elements instead (refer to Fig. 2.2).

A cellular solid with slender walls differs from a porous solid according to the relative density ρ^* (Sec. 2.1). For increasing relative density $\rho^* > 0.3$ (or $h/L > 0.16$), the lattice walls

2.4. Micro-Mechanical Pore Models and Comparison with FE Analyses

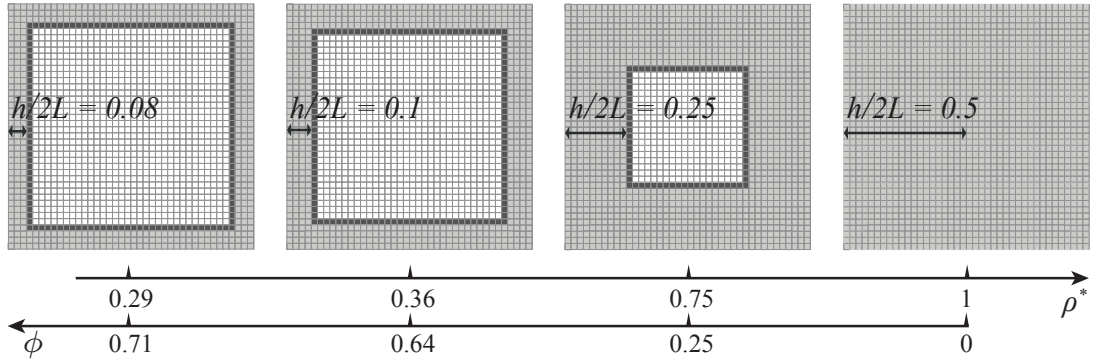


Figure 2.8 – Examples of the unit cell model with different walls thickness: (a) $h/L = 0.16$, $h/L = 0.2$ (b), $h/L = 0.5$ (c), and $h/L = 1$ (d). Solid elements are shown in gray, fluid elements in blue, and coupled elements in green.

become thick, the pores become small, and the cellular solid transforms into mostly solid material with isolated pores [Gibson and Ashby, 1999]. We select the wall thickness values $h = 0.16L$, $0.2L$, $0.5L$, and L to characterize wave propagation in a porous medium with decreasing porosity ϕ (Fig. 2.8). Band structures corresponding to these configurations are shown in Fig. 2.9. The first value from this set of walls thickness, $h/L = 0.16$, corresponds to the transition between cellular and porous solids, whereas $h/L = 1$ represents a homogeneous solid. For frequencies $\omega < 2$ kHz (which represents a threshold of dispersion in Figs. 2.9(a-c)), the pressure-wave velocity for the structure-only case is consistently lower than that of the FSI configuration.

In the limit case $\rho^* \rightarrow 1$, $\phi \rightarrow 0$ (Fig. 2.9(d)) dashed and solid lines coincide, which is the logical confirmation of the absence of fluid cavities. Any dispersion in Fig. 2.9(d) is due to length scales introduced by the RVE. Indeed, for $h = L$, the shear and longitudinal computational wave velocities in the band structure are in excellent agreement with the analytical expressions:

$$c_S = \sqrt{\frac{E_s}{2\rho_s(1+\nu_s)}}, \quad c_L = \sqrt{\frac{E_s(1-\nu_s)}{\rho_s(1+\nu_s)(1-2\nu_s)}}, \quad (2.17)$$

The velocities c_S , c_L are shown in Fig. 2.9(d) in green dashed lines.

2.4.1 Equivalent continuum model for shear waves in a dry cellular solid

Shear waves propagating in the $\Gamma - X$ direction ([1 0] direction in direct space) are equi-luminal and thus are not affected by the hydrostatic-like behavior of the entrained fluid for

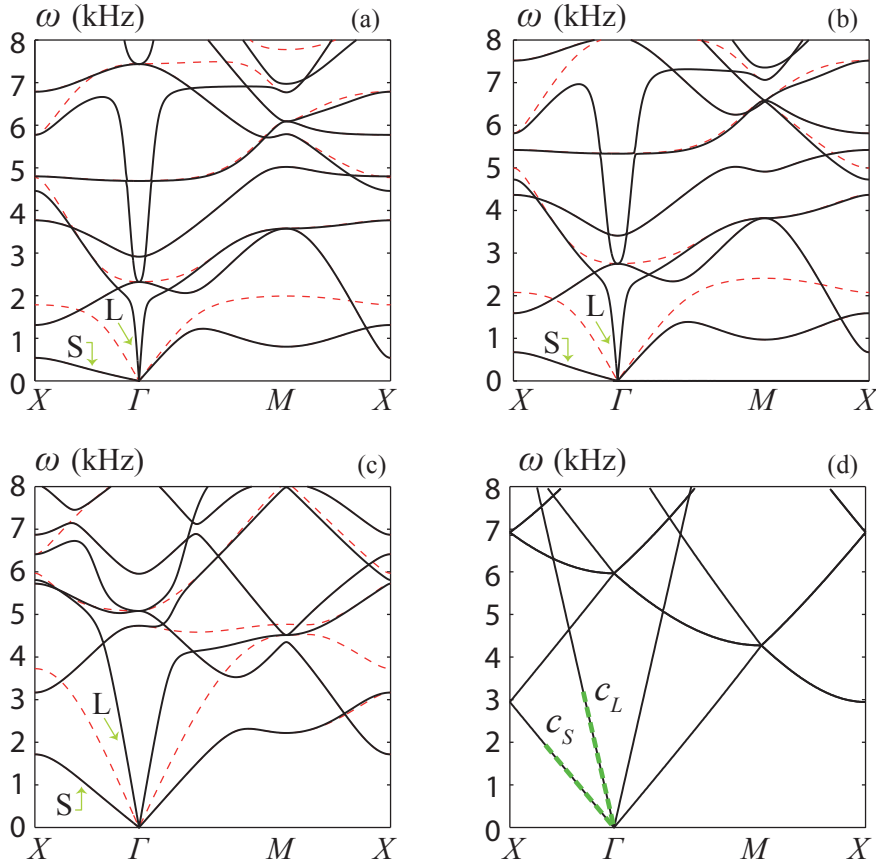


Figure 2.9 – Band structure for a porous medium with entrained air for (a) $h = 0.16L$, (b) $h = 0.2L$, (c) $h = 0.5L$, and (d) $h = L$ corresponding to the RVEs of Fig. 2.8. Solid lines represent solution of the FSI configuration, dashed red lines are the solution to the structure-only case. Shear and longitudinal (pressure) wavemodes are denoted as S and L respectively. Dashed lines in (d) denote the phase velocities of Eqs. (2.17).

$\hat{\omega} < 1$. Accordingly, the strain energy in the RVE is only due to microstructural deformations of the walls. Letting the microstructural strain energy be the same as that of an equivalent continuum occupying the same volume as the RVE, one finds the relation between macroscale shear stress and strain to be [Bažant and Christensen, 1972, Gibson and Ashby, 1999, Kumar and McDowell, 2004]:

$$\sigma_{12} = \frac{E_s h^3}{L_1^2 L_2} \varepsilon_{12} = E_s \left(1 - \sqrt{1 - \rho^*}\right)^3 \varepsilon_{12} = C_{44} \varepsilon_{12}, \quad (2.18)$$

where C_{44} is the coefficient of the corresponding homogenized elasticity tensor. L_1, L_2 are the length and the width of the RVE, respectively (in our case $L_1 = L_2 = L$). The speed of the shear wave in the low-frequency regime in the $[1\ 0]$ direction for an equivalent medium with

2.4. Micro-Mechanical Pore Models and Comparison with FE Analyses

effective density $\bar{\rho} = \rho^* \rho_s + (1 - \rho^*) \rho_f$ is:

$$c_S = \sqrt{C_{44} / \bar{\rho}}, \quad (2.19)$$

which in terms of relative density is:

$$c_S = \sqrt{\frac{E_s (1 - \sqrt{1 - \rho^*})^3}{(1 - \rho^*) \rho_f + \rho^* \rho_s}}. \quad (2.20)$$

The homogenized shear-wave velocity is well posed in that its limit exists:

$$\lim_{\rho^* \rightarrow 0} c_S = 0, \quad (2.21)$$

and Eq. (2.20) correctly captures the effects of added mass of the entrained fluid, in the long-wavelength limit, in addition to the contribution of the micro-structural deformation. This fact is shown in Fig. 2.6(b), which provides the model test conducted for both types of the entrained fluid: air and water. Furthermore, as the wall thickness h increases, the phase velocity of the shear mode S increases (Fig. 2.9). This is consistent with Eqs. (2.18) and (2.20). We find the same agreement with the plane-element model.

2.4.2 Comparison with Biot's theory

In the current section the numerical model is discussed in the context of Biot's theory introduced in detail in Sec. 1.3.2. The equilibrium Eqs. (1.29, 1.30) can be also written in terms of porosity as:

$$\begin{aligned} \nabla_j \sigma_{ij}^{(m)} &= \rho_{11} \ddot{u}_i^{(m)} + \rho_{12} \ddot{u}_i^{(f)}, \\ -\phi \nabla_i p_f &= \rho_{12} \ddot{u}_i^{(m)} + \rho_{22} \ddot{u}_i^{(f)}. \end{aligned} \quad (2.22)$$

In order to compare Biot's theory to our idealized two-phase medium, we recast the constitutive law for plane-strain conditions as:

$$\left\{ \sigma_{11}^{(m)} \sigma_{22}^{(m)} \sigma_{12}^{(m)} \sigma^{(f)} \right\}^T = \hat{C} \left\{ \varepsilon_{11}^{(m)} \varepsilon_{22}^{(m)} 2\varepsilon_{12}^{(m)} \theta_f \right\}^T, \quad (2.23)$$

where \hat{C} is the plane-strain stiffness tensor given by matrix with components \hat{C}_{ij} , obtained from Eqs. (1.5). These components depend on the following mechanical parameters of the frame (matrix): the Young's modulus E_m , the shear modulus μ_m , and the bulk modulus of the

Chapter 2. Numerical Model of a 2D Square Lattice With Entrained Fluid

frame K_m (or generalized drained modulus). The mechanical properties of isotropic foams with closed cells can be approximated by [Gibson and Ashby, 1999]:

$$\begin{aligned} E_m &= 0.32E_s [(\rho^*)^2 + \rho^*], \\ \mu_m &= 3/8E_s(\rho^*)^2, \end{aligned} \quad (2.24)$$

where E_s is the Young's modulus of the material composing the frame.

While the square lattice is not isotropic, and anisotropic formulations of Biot's theory are available although require many constants, we restrict ourselves to analyzing waves propagating in the [1 0] direction, and thus we consider an isotropic model. According to [Carcione, 2007], the generalized drained bulk modulus can be represented as:

$$K_m = \frac{2}{9}\rho_s \frac{h}{L}. \quad (2.25)$$

With the mechanical properties for a 3D medium in hand, the stiffness tensor for plane conditions is derived as usual. Taking the divergence of Eqs. (2.22) and considering plane harmonic waves, one obtains:

$$(\hat{C}_{11} + \hat{C}_{12} + 2\hat{C}_{33}) \left(\frac{\partial^2}{\partial x_1^2} + \frac{\partial^2}{\partial x_2^2} \right) \theta_m + \hat{C}_{14} \left(\frac{\partial^2}{\partial x_1^2} + \frac{\partial^2}{\partial x_2^2} \right) \theta_f = \rho_{11}\ddot{\theta}_m + \rho_{12}\ddot{\theta}_f \quad (2.26)$$

$$\hat{C}_{14} \left(\frac{\partial^2}{\partial x_1^2} + \frac{\partial^2}{\partial x_2^2} \right) \theta_m + \hat{C}_{44} \left(\frac{\partial^2}{\partial x_1^2} + \frac{\partial^2}{\partial x_2^2} \right) \theta_f = \rho_{12}\ddot{\theta}_m + \rho_{22}\ddot{\theta}_f. \quad (2.27)$$

Recall, that $\theta_m = \text{tr}(\epsilon_{ij}^{(m)})$, and $\theta_f = \text{tr}(\epsilon_{ij}^{(f)})$.

The procedure used to derive the pressure wave velocities is identical to the one for Eq. (1.39), thus assuming plane harmonic wave:

$$\boldsymbol{\theta} = \check{\boldsymbol{\theta}}(k) e^{i\omega t}, \quad (2.28)$$

Eq. (2.27) can be recast into the eigenvalue problem:

$$[\hat{B} - c_p^2 D] \cdot \check{\boldsymbol{\theta}} = \mathbf{0}, \quad (2.29)$$

where the eigenvalue $c_p = \omega / \|\mathbf{k}\|$ is the pressure wave phase velocity, $\check{\boldsymbol{\theta}}$ is the total vector of

2.4. Micro-Mechanical Pore Models and Comparison with FE Analyses

displacement and pressure amplitudes, and:

$$[\hat{B}] = \begin{bmatrix} \hat{C}_{11} + \hat{C}_{12} + 2\hat{C}_{33} & \hat{C}_{14} \\ & \hat{C}_{14} \\ & \hat{C}_{14} & \hat{C}_{44} \end{bmatrix}, \quad [D] = \begin{bmatrix} \rho_{11} & \rho_{12} \\ \rho_{12} & \rho_{22} \end{bmatrix}.$$

The solution to the eigenvalue problem Eq. (2.29) provides the phase velocity c_p^B of pressure waves in the long-wavelength regime under plane-strain conditions starting from the 3D constitutive law. Of note, Eq. (2.29) predicts two pressure wavemodes: a fast one with fluid and structure displacing in phase, and a slow one with fluid and structure displacing out of phase.

The procedure to find the pressure wave velocity for the initially plane problem is the same as the one used to derive Eq. (2.29). The approach in this case is to use mechanical parameters derived in the drained case for the 2D square lattice [Kumar and McDowell, 2004]:

$$\begin{aligned} E_m &= \frac{E_s h}{L}, \\ \mu_m &= \frac{E_s h^3}{L_1^2 L_2} = \frac{E_s h^3}{L^3}, \end{aligned} \quad (2.30)$$

completed with the frame bulk modulus K_m given by Eq. (2.25). We attribute this choice to the fact that the shear modes in the band structure are unchanged (Sec. 2.3.1). If one denotes the plane stiffness tensor by \tilde{C} , then, assuming plane harmonic wave (Eq. (2.28)), the phase velocity of the pressure wave in the long-wavelength regime is:

$$[\tilde{B} - c_p^2 D] \cdot \tilde{\theta} = \mathbf{0}, \quad (2.31)$$

where:

$$[\tilde{B}] = \begin{bmatrix} \tilde{C}_{11} + \tilde{C}_{12} + 2\tilde{C}_{33} & \tilde{C}_{14} \\ & \tilde{C}_{14} \\ & \tilde{C}_{14} & \tilde{C}_{44} \end{bmatrix}.$$

The difference between Eqs (2.29) and (2.31) is given in Table 2.1.

A similar approach can be used to derive the shear-wave velocity (refer to Eq. (1.40)). Taking the curl of the sum of Eqs. (2.22) and assuming plane harmonic waves, the phase velocity of

Plane strain (Eq. (2.29), initially 3D)	Plane (Eq. (2.31), 2D)
$\hat{C}_{11} + \hat{C}_{12} + 2\hat{C}_{33} = 4a_1 + 5/3a_2$	$\tilde{C}_{11} + \tilde{C}_{12} + 2\tilde{C}_{33} = 4a_1 + a_2$
$\hat{C}_{14} = a_3$	$\tilde{C}_{14} = a_3$
$\hat{C}_{44} = 2a_4$	$\tilde{C}_{44} = 2a_4$

Table 2.1 – Relation between stiffness-tensor constants and parameters of the strain-energy density (Eq. (1.4)) for plane strain and initially plane cases.

shear waves in the low-frequency regime is (refer to Eq. (1.40)):

$$c_S^B = \sqrt{\frac{\mu_m}{\bar{\rho} - \rho_f \phi \tau^{-1}}} = \sqrt{\frac{\mu_m}{\rho_s(1 - \phi) + \rho_f \phi(1 - \tau^{-1})}}. \quad (2.32)$$

We note that the phase velocities of shear wave for plane-strain and initially plain conditions are the same, and match c_S^B in the 3D case (Eq. (2.32)).

2.4.3 Comparison of analytical and FE models

Thin internal components in cellular solids, like the walls of the square lattice, may resonate inducing strong dispersion even for wavelengths much smaller than the characteristic pore length L . The thicker solid phase in porous materials does not resonate, at least for the first several branches in the band structure, and dispersion is the result of Bragg scattering for wavelengths near L . Biot's theory was derived to describe the macroscopic behavior in the latter regime. It is of interest to extend Biot's theory to the case of cellular solids.

For this purpose, we analyze three configurations defined by $(h/L = 0.02, \rho^* = 0.04)$, $(h/L = 0.4, \rho^* = 0.64)$, and $(h/L = 0.8, \rho^* = 0.96)$ with entrained air. This first configuration is a cellular solid, while the second and third are porous solids. As Biot's theory describes the elasto-static behavior of porous medium, we restrict our analysis to the acoustic branches of the band structure near the Γ point for pressure modes (Fig. 2.10(a-c)), and $\Gamma - X$ for shear modes. The review of Biot's theory in Sec. 1.3.2 pertains to isotropic materials, while the square lattice has cubic symmetry. As a result, we restrict comparisons of Biot's theory and numerical results to wavenumbers in $\Gamma - X$ direction. Biot's theory predicts a fast and a slow pressure mode; our calculations, on the other hand, predict the presence of the fast-pressure mode only for frequencies below the first resonance of the lattice walls. The phase velocity of the fast pressure mode predicted by Biot's theory is in good agreement for $\rho^* \lesssim 0.5$ (Fig. 2.10(a-c)).

In the absence of dissipation, the shear wave velocity from Biot's theory is given by Eq. (2.32).

2.4. Micro-Mechanical Pore Models and Comparison with FE Analyses

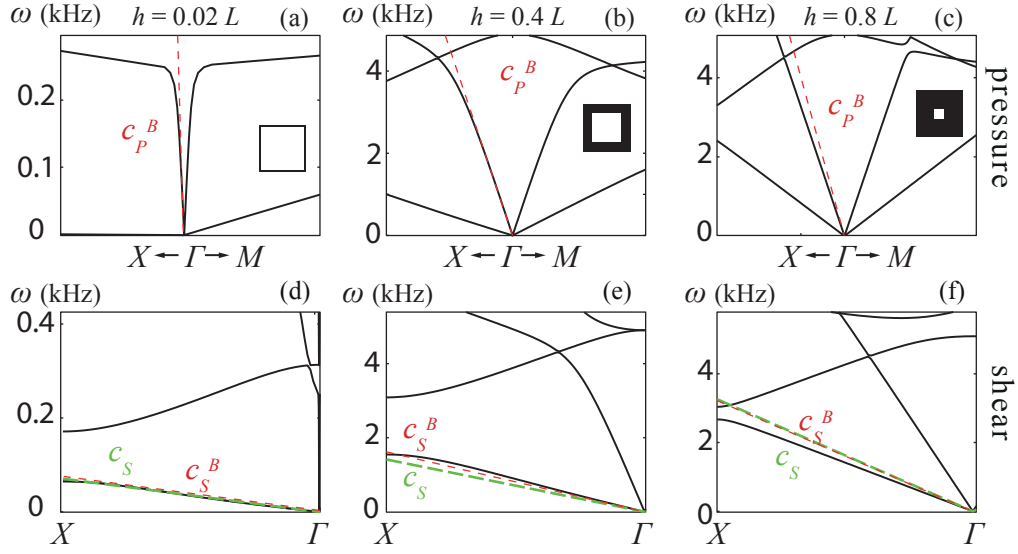


Figure 2.10 – Band structures for a square lattice with entrained air with $h/L = 0.02$ (a,d), $h/L = 0.4$ (b,e), and $h/L = 0.8$ (c,f). Panel (a-c) highlight pressure modes, while panels (d-f) highlight shear modes. Red dashed lines denote shear and pressure phase velocities from Biot's theory. Thick green dashed lines denote the shear-wave velocity of Eq. (2.20). The insets in (a-c) show the RVE for each configuration.

This equation differs from the homogenized model equation (2.20) by the coefficient $(1 - \tau^{-1})$ multiplying the term $\rho_f \phi$ in Eq. (2.32). According to the definition of tortuosity introduced above, and a closed-cells configuration, we employ $\tau \rightarrow \infty$. One can also verify that this is necessary for convergence of Eq. (2.32) to Eq. (2.20) which is in excellent agreement with our computational models (Fig. 2.6).

Expanding the expressions (2.20) and (2.32) in Taylor series for two limit cases of $\phi \rightarrow 0$ ($\rho^* \rightarrow 1$) and $\phi \rightarrow 1$ ($\rho^* \rightarrow 0$), one obtains:

$$\begin{aligned} \lim_{\phi \rightarrow 0} c_S &= \lim_{\phi \rightarrow 0} c_S^B = \sqrt{\frac{E_s}{\rho_s}}, \\ \lim_{\phi \rightarrow 1} c_S &= \lim_{\phi \rightarrow 1} c_S^B = 0. \end{aligned} \quad (2.33)$$

However, the rate of convergence differs and depends on the values of τ and ρ_f . The latter fact is further confirmed by Fig. 2.11(a,b). For $\phi \rightarrow 0$, both models in error by $1/\sqrt{1 + \nu_s}$ with respect to the first equation of Eq. (2.17), which for $\nu_s = 0.33$ is 14%. Eq. (2.20) is derived employing Bernoulli-beam theory, which does not take in account shear deformations of the beam cross-section. Employing Timoshenko-beam theory [Kumar and McDowell, 2004] gives $c_S = \sqrt{E_s/2\rho_s(1 + 1.2(1 + \nu_s))}$ as $\rho^* \rightarrow 1$. This correction underestimates the shear velocity by

27%.

Biot's pressure wave velocities under the plane-strain conditions (Eq. (2.29)) and initially plane conditions (Eq. (2.31)) in the solid limit:

$$\begin{aligned} \lim_{\rho^* \rightarrow 1} c_P^B &= \sqrt{\frac{E_s(11/6 - 2/3\nu_s)}{\rho_s(1 - 2\nu_s)(1 + \nu_s)}} \quad (\text{plane-strain}), \\ \lim_{\rho^* \rightarrow 1} c_P^B &= \sqrt{\frac{3/2E_s}{\rho_s(1 - 2\nu_s)(1 + \nu_s)}} \quad (\text{initially 2D}) \end{aligned} \quad (2.34)$$

overestimate the plane-strain value (Eq. (2.17)) for $\nu_s = 0.33$ by 55.2% and 49.6%, respectively. The latter difference is based on the fact that the strain energy density coefficients a_k in Biot's theory are derived from the beam equations for the lattice walls. Therefore, as h/L increases, these coefficients should be updated, but are not available analytically. Thus, we rely on the beam theory given the fact that C_{44} from Eq. (2.19), when $\rho^* \rightarrow 1$, has small discrepancy with values for a continuum.

In order to explore the bounds of applicability for Biot's theory and the contribution of entrained fluid, we repeat the analyses of Fig. 2.10 for $1 \times 10^{-4} \leq \rho^* \leq 1$ with both air and water. We consider RVEs discretized with both beam and plane elements to explore very small and very large values of ρ^* but also to compare the performance of each element type. Beam and plane elements are in agreement in predicting the shear-wave velocity for all considered values of relative density. We find the same for air and water (Figs. 2.11(a-b)).

In the case of pressure waves, Biot's theory well predicts the phase velocity for the considered values of ρ^* . In the case of air (Fig. 2.11(c)) Biot's estimation c_P^B diverges from the computational model for values of ρ^* smaller than for the case of water (Fig. 2.11(d)). In the case of air, Biot's theory overestimates the pressure-wave velocity and beam elements exceed the velocity predicted by plane elements for $\rho^* > 0.1$. In this case, the discrepancy between beam and plane elements may partly be attributed to the fact that the size of the fluid cavity does not vary for increasing ρ^* for the former elements. We also note that the performance of Biot's theory with plane-strain and initially plane formulations is very similar. In the case of air, plane elements exceed the values predicted by beam elements for $\rho^* < 0.03$; this is reasonable as plane elements are known to be stiffer than beam elements when modeling structures with large aspect ratios [Cook, 2001]. Nonetheless, the agreement between plane-elements and Biot's theory is excellent for $\rho^* < 0.1$. In the case of water, beam elements significantly overestimate the pressure wave velocity for all values of ρ^* . We believe that this discrepancy results from the perfect rigidity of beam-element cross section. Beam theory indeed neglects

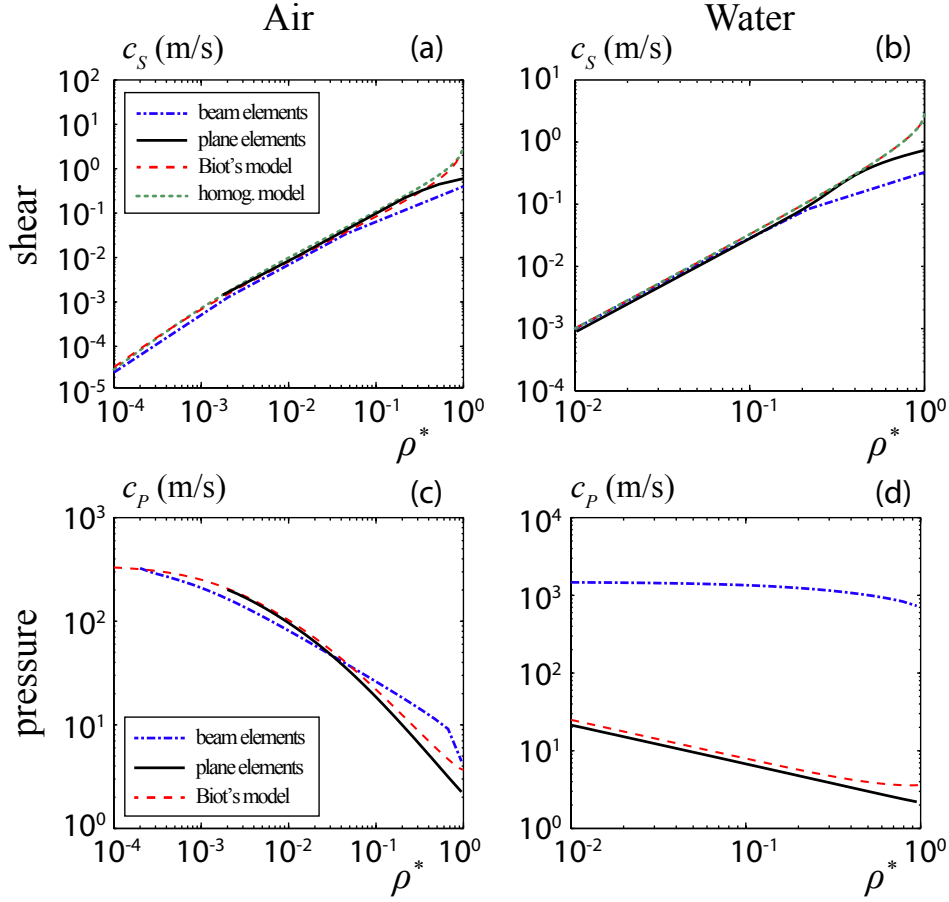


Figure 2.11 – Phase velocities for shear ((a) and (b)) and pressure ((c) and (d)) waves for entrained air ((a) and (c)) and water ((b) and (d)) for increasing relative density. Solid and dashed-dotted lines correspond to the RVE model discretized with plane and beam elements, respectively. Red dashed lines denote Biot’s theory for plane conditions. Green dotted lines in panels (a) and (b) correspond to the homogenized model for shear in drained conditions [Kumar and McDowell, 2004]. All velocities correspond to wavenumbers in the $\Gamma - X$ direction.

direct stress components perpendicular to the beam axis. The bulk modulus of water ($B_f = 2.2$ GPa) is much larger than that of solid phase in our model ($B_s = 6.25$ kPa) while the densities are the same. In this case, the fluid cavity can be considered as a rigid inclusion, and it is reasonable to expect most deformations to take place in the solid phase. Despite the suspected shortcomings of beam theory, Biot’s theory is nonetheless in reasonable agreement (Fig. 2.11(d)).

2.5 Conclusion

In the present chapter, we analyze elastic-wave propagation in cellular and porous solids with entrained fluid and disjointed pores. We employ a periodic square lattice in plane-strain conditions as the simplest porous solid, and we analyze the propagation of plane waves by considering a representative volume element. We use finite-element models based on beam and plane elements for the solid phase and plane elements for the fluid phase. Our objective is to explore the applicability of Biot's theory, originally devised for porous media, to estimate the phase velocity of shear and pressure waves in the long-wavelength limit in cellular solids. We compare analytical and numerical models for configurations with relative density $1 \times 10^{-4} \leq \rho^* \leq 1$ considering both air and water as the fluid phase, for which we neglect convection and viscosity.

For waves with frequency-spectra well below the first resonance frequency of the pores, we find that the deformations and phase velocity of pressure wavemodes are strongly affected by the entrained fluid unlike shear modes. The latter are altered by added mass effects only, and their phase velocity is decreased by the presence of fluid. For waves with frequency spectra exceeding the first resonance frequency of the cavity, the fluid effectively couples to both shear and pressure wavemodes, owing to strong pressure gradients in the fluid domain. Biot's theory moreover predicts two pressure modes, a fast and a slow one, but for frequencies below resonance of the lattice walls, we only find the fast mode. For higher frequencies, both pressure modes are present.

We find that Biot's theory based on mechanical properties derived from beam theory overestimates the phase velocity of pressure waves in porous media as $\rho^* \rightarrow 1$, but it is otherwise in excellent agreement with computational models. In the case of shear-wave velocities, we find that homogenized models based on microstructural deformations for drained configurations perform equally well as Biot's model, at least for a square lattice.

An alternative theory of wave propagation in cellular solids with entrained compressible fluid, based on dynamic deformations of the microstructure, will be discussed in Chapter 3. The alternative equivalent continuum model for longitudinal waves will be introduced as well.

3 Numerical and Homogenized Analysis of Pressure Waves

The chapter is mainly reprinted from [Dorodnitsyn and Spadoni, 2014b] with authorization of the publisher.

3.1 Introduction

The propagation of waves in a heterogeneous medium is determined by the character of the heterogeneities, which may simply be impedance barriers immersed in a matrix. These can be voids and inclusions with impedance jumps due to material properties or their own dynamics. A typical example may be that of sound waves in water with bubbles, in which propagation characteristics can be derived based on the resonance frequency of a single bubble isolated in water [Feuillade, 1996], which is known as the Minnaert frequency [Minnaert, 1933]. A similar approach may be adopted to describe the dynamics of a porous medium [Diebels and Ehlers, 1996, Stinson and Champoux, 1992], composed of a solid matrix or skeleton bounding fluid-filled pores. In [Stinson and Champoux, 1992], the skeleton is considered rigid and the dynamics of the fluid in the pores, simplified as tubes of various cross sections, provide an effective bulk modulus; refinements based on pore-shape factors provide reasonable comparisons with experimental measurements. A similar approach is employed in [Wang and Lu, 1999] to optimize absorption.

As the pore fraction – the porosity ϕ – increases, the skeleton should not be considered rigid with respect to the pores, since the dynamics of both phases interact. These conditions prove more difficult to describe with dynamic models for the pores alone and are modeled by Biot's theory instead [Biot, 1956a,b, Biot and Willis, 1957]. Biot's theory is derived from a macroscale-strain-energy functional based on averaged microstructural quantities [Allard

and Atalla, 2009, Carcione, 2007]. The bridging between micro and macroscales has since been validated with rigorous micromechanical models [Auriault and Sanchez-Palencia, 1977, Burridge and Keller, 1981, Cheng, 1997, Dormieux et al., 2002, Thompson and Willis, 1991]. Biot's theory, however, requires the knowledge of the equivalent-continuum properties of the skeleton for both drained and undrained conditions; in addition to the tortuosity needed to phenomenologically describe the geometric nature of the pores, these parameters are often not analytically available and are experimentally obtained for specific configurations [Chekkal et al., 2012, Gravade et al., 2012, Gueven et al., 2012]. More phenomenological parameters, especially for fluid-solid inertia coupling, are required for anisotropic media [Carcione, 2007]. A more detailed analysis yet of microstructural behavior improves on Biot by considering porosity as a field variable [Lopatnikov and Cheng, 2004].

As the porosity ϕ increases, the volume occupied by the solid phase, given by the relative density $\rho^* = 1 - \phi$, decreases, yielding a cellular solid. The distinction between porous and cellular solids is phenomenological and is given by $\rho^* < 0.3$ (Sec. 1.3.2). Similar to porous solids, cellular solids may have open and closed-cell configurations. The former are used for absorption of sound [Gibson and Ashby, 1999, Gravade et al., 2012, Hoang and Perrot, 2013, Lind-Nordgren and Göransson, 2010, Lu et al., 2000, Perrot et al., 2008b, Wang and Lu, 1999] and energy [Dempsey et al., 2005, Evans et al., 1998, Wang and McDowell, 2005]. Closed-cell configurations are more challenging to model analytically and are often described by phenomenological models based on the effective properties of an equivalent continuum [Chevillotte and Panneton, 2007, Doutres et al., 2011]. In this direction, theoretical models based on frequency-dependent equivalent density and bulk modulus have recently been proposed to evaluate methods to enhance sound absorption in partially-perforated closed-cell foams [Chevillotte et al., 2010, Perrot et al., 2008a]. Alternatively, the stiffness tensor of an equivalent continuum can be numerically evaluated from the dispersion relations of a unit cell: numerical models for the acoustic absorption properties based on the effective density and compressibility parameters are discussed in [Lee et al., 2009] for porous media with cubic and hexagonal unit cells. Conversely, starting with numerical models for frequency-dependent properties, wave propagation for a general periodic medium is discussed in [Stadler and Schanz, 2010]. Analytically, however, even the static response is challenging to describe at the microstructural level, and phenomenological models scaling with ρ^* are common [Gibson and Ashby, 1999, Roberts and Garboczi, 2001, Warner et al., 2000].

While Biot's theory has been validated for porous media, less is known about its performance for cellular solids with closed cells especially for $\rho^* \rightarrow 0$. In the case of the 2D periodic

configurations accurate equivalent-continuum mechanical properties are available for drained conditions [Gibson and Ashby, 1999, Gonella and Ruzzene, 2008b, Kumar and McDowell, 2004, Spadoni and Ruzzene, 2012, Suiker et al., 2001]. Employing a numerical model accounting for fluid-structure interaction (FSI) in a representative-volume element (RVE), an excellent quantitative agreement with Biot's theory and our numerical results for wave propagation in a square lattice was shown in Chapter 2 (also in [Dorodnitsyn and Spadoni, 2014a]). Biot's theory, however, is based on complex expressions of geometric and material parameters and does not lend itself to analyzing the physical origin of specific wave-propagation characteristics beyond qualitative statements. In this chapter, we propose a much simpler model for equivalent-continuum behavior, given the microstructural deformations computed from our numerical models. Based on this model, we describe three fundamental frequencies denoting the resonance of the skeleton, resonance of the pores, and resonance of the combination of the two. We also describe three propagation regimes, in terms of ρ^* , determined by the deformation mechanisms of the skeleton, as the bending, through-the-thickness deformations, and hybrid modes.

We employ finite-element (FE) analysis, detailed in Sec. 2.2 and summarized in 3.2, that explicitly considers the direct coupling of fluid and structural dynamics in an RVE to compute dispersion surfaces and associated wavemodes. In Sec. 3.3, a tube-piston model that describes the micro-mechanical behavior of pores for pressure waves is proposed. Such model is compared with the numerical results and Biot's theory. Sec. 3.4 introduces a macromechanical equivalent-continuum model, which allows us to determine the effective stiffness tensor. The phase velocity of wavemodes in the long-wavelength limit are evaluated from dispersion surfaces computed with the FE models and are compared to phase velocities obtained from the Christoffel matrix, based on the proposed equivalent-stiffness tensor. Typical deformation mechanisms determined by the mass coupling and relative density are discussed in Sec. 3.4. The analyses and findings are summarized in Sec. 3.5.

3.2 Geometry, RVE, and Numerical Results

In this section, we use the results from finite-element (FE) analysis, detailed in Sec. 2.2.3, where the band structure (relation between the frequency ω and wavevector $\mathbf{k} = \{k_x, k_y\}^T$ along the boundaries of the irreducible Brillouin zone [Brillouin, 2003]) is obtained from the eigenvalue problem Eq.(2.16). For $L = 100 \mu\text{m}$, $\rho^* = 0.04$, skeleton Young's modulus $E_s = 1 \text{ kPa}$, density $\rho_s = 1000 \text{ kg/m}^3$, and air as the entrained fluid with speed of sound $c_0 = 343 \text{ m/s}$, density $\rho_f = 1.225 \text{ kg/m}^3$, and bulk modulus $B_f = 142 \text{ kPa}$, we obtain the band-structure

shown in Fig. 3.1. Following the notation in Sec. 2.3, dashed lines in Fig. 3.1 denote the solution to the structure-only configuration (simulations with no pressure dofs involved), while solid lines denote the solution to the two-phase (FSI) configuration.

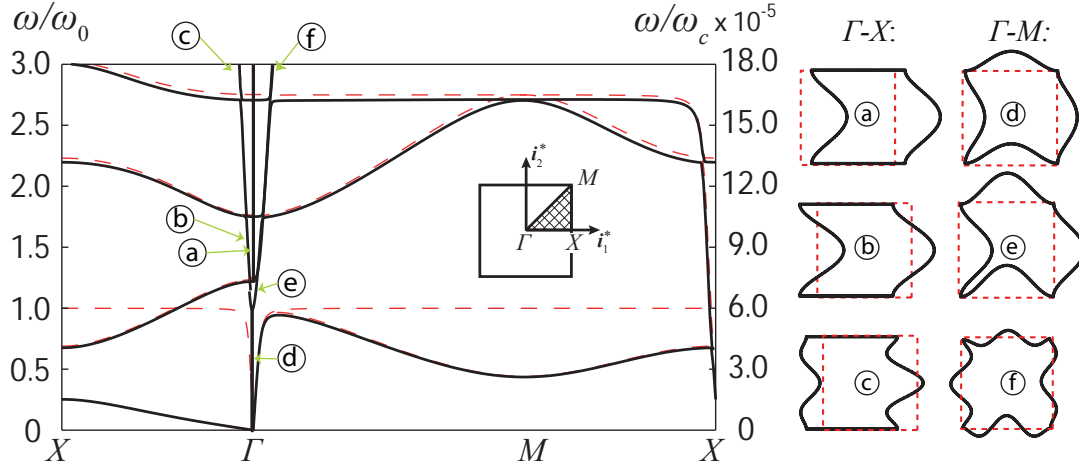


Figure 3.1 – Band structure for RVE with $L = 100 \mu\text{m}$, $\rho^* = 0.04$ discretized with beam elements for the irreducible Brillouin Zone with high-symmetry points Γ , X , M . Left ordinate is normalized by the first natural frequency of a clamped-clamped beam, ω_0 ; the second ordinate is normalized by the first natural frequency of the fluid cavity alone, ω_c . Solid lines are the solution to the FSI problem, dashed lines are the solution to the structure-only case. Circled letters (a-f) denote wavenumber combinations used to depict fluid-structure pressure-wavemodes (in the right part), with solid and dashed lines denoting the deformed and initial configurations respectively.

For the aforementioned properties, the following facts transpire. Cell-wall resonance $\bar{\omega} = \omega/\omega_0 = 1$ is a strong source of dispersion. Note that if $\rho_f \ll \rho_s$, ω_0 is that of a clamped-clamped beam in vacuum, otherwise the fluid added mass must be included. The shear response is not affected by the entrained fluid for the square lattice. The FSI solution yields a fast pressure mode for $\bar{\omega} < 1$ and two pressure modes for $\bar{\omega} > 1$. Wavemodes corresponding to the labels in band-structure are shown in right-hand side of Fig. 3.1. The pressure wavemode (a) has the same polarization for $\bar{\omega} < 1$ and $\bar{\omega} > 1$. For $\hat{\omega} = \omega/\omega_c < 1$, the pressure distribution within the pores is uniform and only odd modes of the cell walls are excited.

3.3 Micro-Mechanical Pore Models

The shear waves propagating in the $\Gamma - X$ direction ($[1\ 0]$ -direction in direct space) are equioluminal, thus, are not affected by the hydrostatic-like behavior of the entrained fluid for $\hat{\omega} < 1$. Accordingly, the strain energy in the RVE is only due to microstructural deformations

of the walls. Therefore, if one lets the microstructural strain energy be the same as that of an equivalent continuum occupying the same volume as the RVE, a relation between macroscale shear stress and strain is obtained in Chapter 2. The linearity of the longitudinal-wave velocity near the Γ -point (see Fig. 3.1) suggests that homogenization techniques can describe low-frequency longitudinal waves analogously to shear waves. Such models are only available for the structure-only case [Kumar and McDowell, 2004] for which the propagation of longitudinal waves in the $[1\ 0]$ -direction is described by $c_L^* = \sqrt{C_{11}/\bar{\rho}}$, where $C_{11} = E_s h/L$, and effective density $\bar{\rho} = \rho^* \rho_s + (1 - \rho^*) \rho_f$. This model is in excellent agreement with our numerical results for the structure-only case but significantly underestimates the pressure-wave velocity for fluid-filled configurations. We proceed with a more appropriate homogenized-continuum model for the FSI-case.

3.3.1 Equivalent continuum model for pressure waves

Pressure modes in the $[1\ 0]$ direction (see Figs. 3.1(a-c)) present in-phase wall deflections described by appropriate combinations of odd modeshapes of a clamped-clamped beam (the joints between walls are rigid). This is consistent with the hydrostatic loading imparted by the fluid. The horizontal walls are undeformed as this guarantees minimum energy in the RVE. The simple deformed configuration of pressure modes in the $[1\ 0]$ -direction (see Figs. 3.1(a-c)) suggests the analogy of a tube with one end constrained by a moving piston and closed end on the other side. This model is depicted in Fig. 3.2. The modeling of cavities in porous media as tubes with an effective cross-sectional area is a common technique (see [Carcione, 2007, Stinson and Champoux, 1992] and references therein). Here, we extend this technique for cavities with deformable walls.

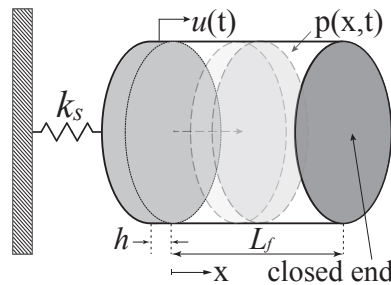


Figure 3.2 – 1D tube-piston model applicable in the linear pressure mode regime.

Infinitesimal pressure oscillations in the tube are governed by the one-dimensional (for waves

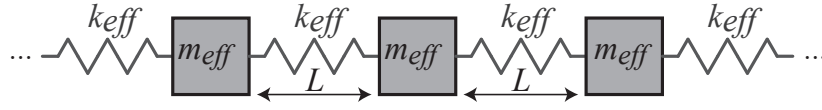


Figure 3.3 – Representation of the aligned tube-piston unit cells as system of springs and masses in series with effective stiffness and mass (k_{eff} , m_{eff}) for pressure wave propagation near the Γ point.

in the [1 0] direction) wave equation:

$$\frac{\partial^2 p}{\partial x^2} = \frac{1}{c_0^2} \frac{\partial^2 p}{\partial t^2}, \quad \forall x \in [0, L_f] \quad (3.1)$$

where $L_f = L - h$. The boundary conditions are determined by the presence of the piston as:

$$\left. \frac{\partial p}{\partial x} \right|_{x=0} = -\rho_f \frac{\partial^2 u}{\partial t^2}, \quad \left. \frac{\partial p}{\partial x} \right|_{x=L_f} = 0, \quad (3.2)$$

where u is the displacement of the piston and is defined by:

$$m_s \frac{d^2 u}{dt^2} + k_s u = -p(0, t) A_{eff}, \quad (3.3)$$

where m_s , k_s , and A_{eff} denote the piston's mass, stiffness and effective cross-sectional area. A_{eff} is determined as follows: for a given piston-displacement u the pressure within the tube is $p = \Delta V / V = Au / V$, where V and A are the area and volume of the tube. For wall bending, the change in volume is:

$$\Delta V = \int_0^L \mu(x) dx \cdot 1 = A_{eff} u, \quad (3.4)$$

where $\mu(x)$ is a spatial function that describes the deformation of the skeleton wall with maximum amplitude u , that is, the first eigenfunction of a clamped-clamped beam. Then, for a clamped-clamped beam $A_{eff} \cong 0.5231A$. Eqs. (3.1)-(3.3) are solved simultaneously [Martin, 2007] employing separation of variables $p(x, t) = X(x)T(t)$: the characteristic equation for the coupled system is:

$$\cot(\alpha_r L_f) = \frac{m_s \omega_0}{\rho_f c_0 A_{eff}} \left(\frac{\alpha_r L_f}{\alpha_0 L_f} \right) \left[1 - \left(\frac{\alpha_0 L_f}{\alpha_r L_f} \right)^2 \right] = \beta^{-1} \left(\frac{\alpha_r L_f}{\alpha_0 L_f} \right) \left[1 - \left(\frac{\alpha_0 L_f}{\alpha_r L_f} \right)^2 \right], \quad (3.5)$$

where $\alpha_r = \omega_r / c_0$, while ω_r and ω_0 are the r^{th} natural frequency of the coupled system and the natural frequency of the piston respectively. The coefficient β denotes the non-dimensional

Table 3.1 – Material and geometrical properties used in Cases 1, 2 and 3.

	β	$\alpha_0 L_f$	c_0 , m/s	ρ_f , kg/m ³	B_f , Pa	ρ_s , kg/m ³	E_s , kPa	ρ^*
Case 1	\forall	$\ll \pi/2$	343	1.2	142000	1000	1	0.04
Case 2	$\ll 1$	$\gg \pi/2$	0.01	1	0.0001	1000	1	0.08
	$\gg 1$	$\gg \pi/2$	0.01	10 ⁶	105.7	1000	1	0.2
Case 3	$\ll 1$	$\sim \pi/2$	0.51	1	0.264	1000	1	0.2

fluid-loading parameter, describing the ratio of characteristic specific acoustic impedance of the fluid to the magnitude of impedance of the piston mass per unit area at frequency ω_0 [Fahy and Gardonio, 2007]. Approximate solutions may be obtained for three cases: (1) $\alpha_0 L_f \ll \pi/2$, (2) $\alpha_0 L_f \gg \pi/2$, and (3) $\alpha_0 L_f \cong \pi/2$. The material and geometric properties for each case are listed in Table 3.1.

Case 1

Let us begin with case 1, where we assume that the tube's (cavity) natural frequency is much larger than that of the pistons (cell walls) such that $\alpha_0 L_f = \omega_0 L_f / c_0 \ll \pi/2$, where $\pi/2 = \alpha_f L_f = \omega_f^{oc} / c_0 L_f$ is the non-dimensional wavelength at resonance for the tube open at one end. With this assumption, the first argument of cotangent on the left-hand side of Eq. (3.5) is $\alpha_1 L_f = \alpha_0 L_f (\omega_1 / \omega_0) \ll \pi/2$, and cotangent can be expanded into Taylor series. Therefore, Eq. (3.5) can be simplified by truncating the series expansions of the trigonometric terms: the first natural frequency of the coupled system for truncation at the first two terms is:

$$\omega_1^2 = \omega_0^2 (1 + \delta) + \mathcal{O}(\omega_r^2) \quad (3.6)$$

$$\omega_1^2 = \omega_0^2 \left(\frac{3m_s}{3m_s + A_{eff} L_f \rho_f} \right) (1 + \delta) + \mathcal{O}(\omega_r^3) \quad (3.7)$$

where $\delta = \rho_f c_0^2 A_{eff} / (L_f m_s \omega_0^2)$ is the added stiffness. While truncation at terms $\mathcal{O}(\omega_r^2)$ for the trigonometric terms in Eq. (3.5) provides the canonical first natural frequency for a piston-tube system [Fahy and Gardonio, 2007, Martin, 2007], it is not quantitatively correct as evident in Eq. (3.6). Truncation at terms $\mathcal{O}(\omega_r^3)$ is instead necessary and we propose the first natural frequency of Eq. (3.7). We show below that the truncation of Eq. (3.7) is sufficient.

Provided $\alpha_0 L_f \ll \pi/2$, the fluid behaves hydrostatically and the deflection of the lattice walls is coupled by the added stiffness and mass of the fluid in the vicinity of the Γ -point. The effective

Chapter 3. Numerical and Homogenized Analysis of Pressure Waves

stiffness of the tube-piston model can be written as:

$$k_{eff} = \omega_1^2(m_s + m_f) = \omega_1^2 m_{eff}, \quad (3.8)$$

where m_{eff} is the effective mass of the RVE composed of the sum of structural and fluid masses, m_s and m_f , where assuming the unit out-of-plane thickness:

$$m_s = \rho_s LA/2, \quad (3.9)$$

$$m_f = \rho_f L_f^2. \quad (3.10)$$

The propagation of pressure waves in the [1 0] direction is described by a 1D chain of springs and masses in series (Fig. 3.3), with stiffness k_{eff} (Eq. (3.8)), and mass m_{eff} . The canonical dispersion relation for a chain of masses and springs [Brillouin, 2003] is adapted for our system and the resulting phase velocity of pressure waves in the fluid-filled lattice is:

$$c_P = \frac{\omega}{k_x} = \frac{2}{k_x} \sqrt{\frac{k_{eff}}{m_{eff}}} \sin \frac{k_x L}{2}. \quad (3.11)$$

In the vicinity of the Γ point:

$$\lim_{k_x \rightarrow 0} c_P = L_f \sqrt{\frac{1}{2} \omega_0^2 (1 + \delta)} = L_f \sqrt{\frac{1}{2} \omega_0^2 \left(\frac{3m_s}{3m_s + A_{eff} L_f \rho_f} \right) (1 + \delta)}, \quad (3.12)$$

Let us compare the latter value of c_P with the numerical model. Precisely, one can see that the pressure-wave velocity of Eq. (3.12) well matches the slope of the pressure mode for $\rho^* = 0.04$ in both beam and plane-element models (Figs. 3.4(a-b)). The comparison with plane elements [Dorodnitsyn and Spadoni, 2014a] is necessary as the deformation mechanism of the cell walls depends on the type of entrained fluid, as will be discussed in Sec. 3.4.3. For the solid and fluid properties described in Table 3.1 for case 1, beam and plane elements produce the same results as Fig. 3.1. Moreover, one can generalize the result of Eq. (3.12) to the phase velocity of the fast pressure mode in non-dispersive regimes away from resonance of the cell walls (Fig. 3.4(c)). This follows from a simple consideration of uniform pressure loading which only excites odd modes, which have the same stiffness, and thus the phase velocity of the fast pressure mode is well captured by Eq. (3.12). It is also noteworthy that Eq. (3.12) captures the phase velocity of the fast-pressure mode in the [1 1] direction (or $\Gamma - M$ in Figs. 3.1 and 3.4).

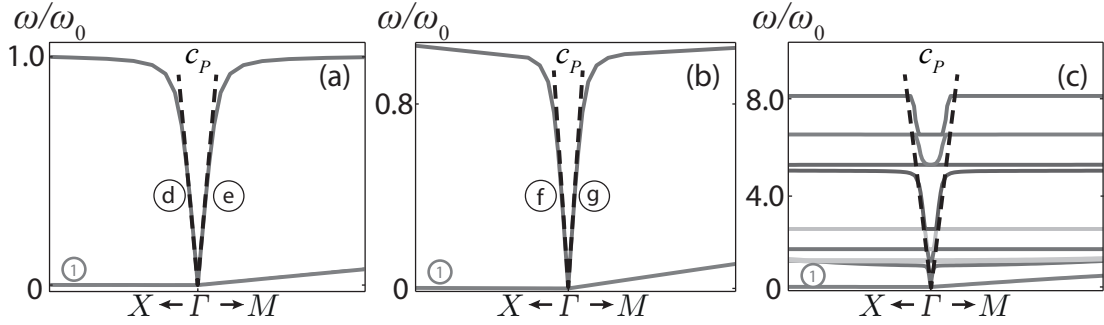


Figure 3.4 – Band structure detail about the Γ point with $\rho^* = 0.04$ for beam (a) and plane-element (b) models [Dorodnitsyn and Spadoni, 2014a]. Superposition of Eq. (3.12) to numerical band structure for high-frequency regimes (c). Circled label (1) denotes the FSI shear mode in $\Gamma - X$ direction.

We would like to explore the developments above from a different point of view. We depict the left (black) and right-hand (red) sides of Eq. (3.5) in Fig. 3.5(a) for case 1 $\alpha_0 L_f \ll \pi/2$: the two curves intersect for $\alpha_r L_f \ll \pi/2$. Two remarks are in order. The term $(\alpha_0 L_f / (\alpha_r L_f))^2$ in Eq. (3.5) is negligible, therefore the solution becomes weakly dependent on β , and is governed by the ratio $\alpha_r L_f / (\alpha_0 L_f)$. The frequency ω_1 represents a resonance with wavelength much greater than the size of closed cells in the lattice. For the parameters chosen here, $2\pi / (\omega_1 / c_0) = 2.47$ cm, or 247 times larger than L . This frequency is the equivalent of the Minnaert frequency for an isolated bubble in water. We make an analogy with the Minnaert frequency since pore resonance is a key scattering source: a volume of fluid enclosed by deformable walls. Because of the deformability of the walls, much like compressible air trapped in a bubble, this entity resonates at frequencies lower than those of fluid-volume alone (with either open or closed/rigid boundaries). The resulting wavelength—considering the speed of sound in the fluid phase—is much larger than the length L_f of the tube in our piston-tube model. Given the periodicity of the lattice moreover, ω_1 describes the behavior of the entire cellular solid in the long-wavelength regime.

The importance of the cell-walls natural frequency ω_0 transcends Eq. (3.5). Given the periodicity of the lattice, symmetry conditions given by Bloch theorem (refer to Sec. 2.2.3) dictate that for wavevector $(\mathbf{k}L = (\pi, 0))$, corresponding to point X in the band structure, $\mathbf{u}_R = -\mathbf{u}_L$ and $\mathbf{u}_T = \mathbf{u}_B$ where subscripts denote the right, left, top and bottom sides of the unit cell. The energetically-favorable solution is identical to that of Fig. 3.1(a), with deformations encompassing the top and bottom sides instead. The entrained fluid is not compressed and simply acts as added mass. Resonance of the cell walls is thus a strong dispersion source, regardless of the type of entrained fluid, as shown in Fig. 3.5(b) where $\rho_f \ll \rho_s$. If $\rho_f \sim \rho_s$, ω_0 is derived

considering that the potential energy only comes from the structural deformations, whereas the kinetic energy is composed of both structural and fluid contributions. The tube-piston model of Sec. 3.3.1 only predicts natural frequencies of the coupled model based on a rigid piston. In our case, the piston is really a deformable surface and thus can resonate for $\omega < \omega_r$. Since the stiffness of the cell walls is the same at all frequencies (away from resonances) however, a theoretical model based on a rigid piston with appropriate stiffness is reasonable. This conclusion will prove accurate in the prediction of the phase velocity also, discussed in Sec. 3.4.

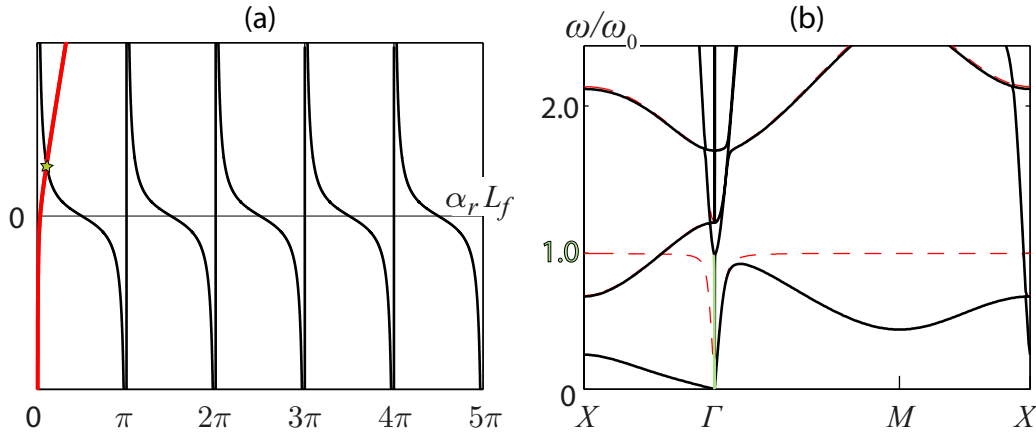


Figure 3.5 – Case 1. Left (black line) and right-hand (red) sides (a) of Eq. (3.5), with corresponding band structure (b) depicting the FSI solution in solid black lines, and the structure-only case in red dashed lines. The ordinate is normalized with ω_0 . The solid green line highlights the $\Gamma - X$ pressure mode in the non-dispersive regime.

Case 2

For case 2 ($\alpha_0 L_f \gg \pi/2$), first-resonance of the pores is lower than that of the cell walls, and $\alpha_0 L_f / (\alpha_r L_f)$ on the right-hand side of Eq. (3.5) is the leading term. In this case, β must be taken into consideration. This leads to two sub-cases: $\beta \ll 1$, and $\beta \gg 1$ corresponding to low and high-density entrained fluid, respectively. The solution to Eq. (3.5) for $\beta \ll 1$ is shown in Fig. 3.6(a), and $\beta \gg 1$ in Fig. 3.6(b). The corresponding band structures are shown in Figs. 3.6(c-d).

For $\beta \ll 1$, the left and right-hand sides of Eq. (3.5) intersect at $\alpha_r L_f = \pi r$ (Fig. 3.6(a)). Thus we expect first dispersion at $\alpha_1 L_f = \pi$, which corresponds to the natural frequency of a closed-closed tube, ω_f^{cc} (Fig. 3.6(a)). For $\alpha_r L_f = \pi r$, the left-hand side of Eq. (3.5) is infinity and the only possibility to satisfy this condition is $\omega_1 \ll \omega_0$. However $\alpha_1 L_f \rightarrow \pi = \omega_f^{cc} / c_0 L_f$, therefore, $\omega_1 = \omega_f^{cc} \ll \omega_0$, which leads the wave propagation to be direction-independent (Fig. 3.6(c)),

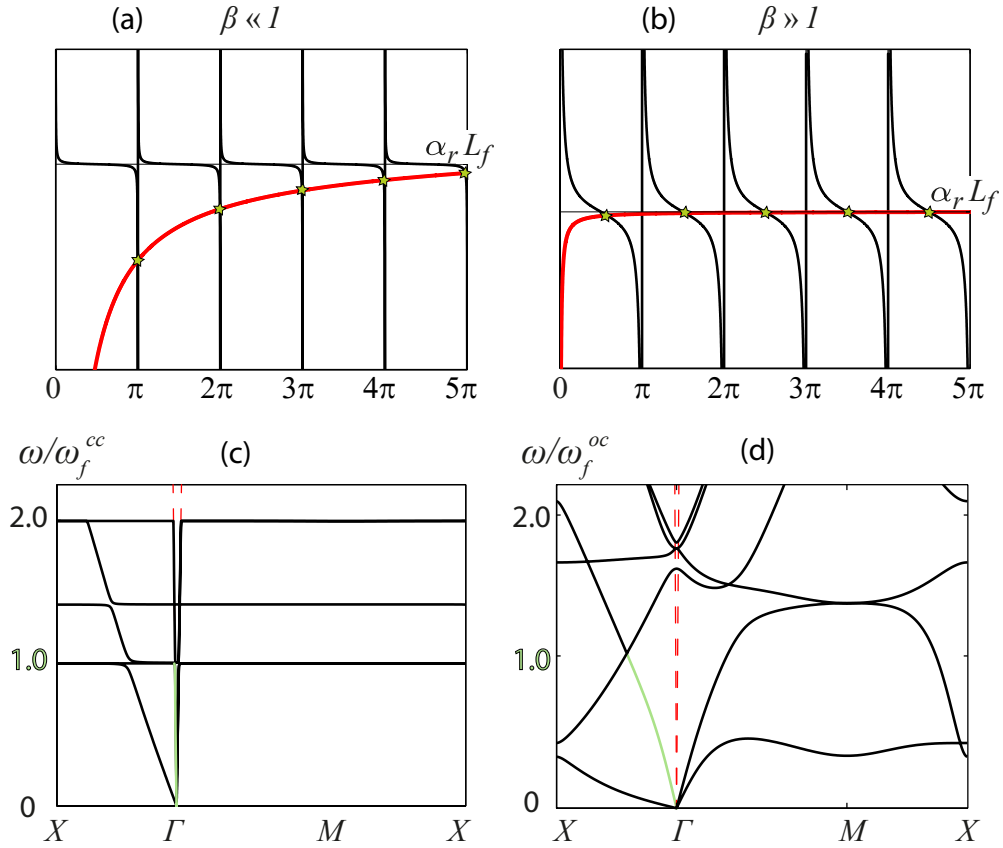


Figure 3.6 – Case 2 (refer to Table 3.1). Left (black line) and right-hand (red) sides of Eq. (3.5) for (a) $\beta \ll 1$ and (b) $\beta \gg 1$. Corresponding band structures (c), (d) where the FSI solution is shown in solid lines, and the structure-only case is in red dashed lines. Ordinates in (c) and (d) are normalized with ω_f^{cc} and ω_f^{oc} , respectively. The solid green lines highlight the $\Gamma - X$ pressure modes in the non-dispersive regime.

a clear indication of internal resonance independent of boundary conditions (wavevector) imposed by Bloch theorem. For $\beta \ll 1$, moreover, the phase velocity of pressure waves for the FSI case is the same as that of the structure only case, provided $\rho_f \ll \rho_s$ indicating a very compressible and light fluid. In this case, the contribution of the entrained fluid is merely dispersion due to phase changes between structural and fluid motion near resonant frequencies of a cavity with rigid walls.

On the other hand when $\beta \gg 1$, solutions to Eq. (3.5) are $\alpha_r L_f = \pi(2r + 1)/2$ (Fig. 3.6(b)), which correspond to the natural frequencies of an open-closed tube, with the first denoted by ω_f^{oc} . The first of such solutions corresponds to $\omega_1 = \omega_f^{oc} \ll \omega_0$; the corresponding band structure is shown in Fig. 3.6(d) where the ordinate axis is normalized by ω_f^{oc} . This case corresponds to a stiff structure with entrained nearly incompressible fluid with high density. In this case,

added mass by the fluid decreases the phase velocity of pressure waves, and fluid resonances introduce strong dispersion (Fig. 3.6(d)). Relative density for this configuration (Table 3.1) is increased to ensure that $\omega_0 \gg \omega_f^{oc}$.

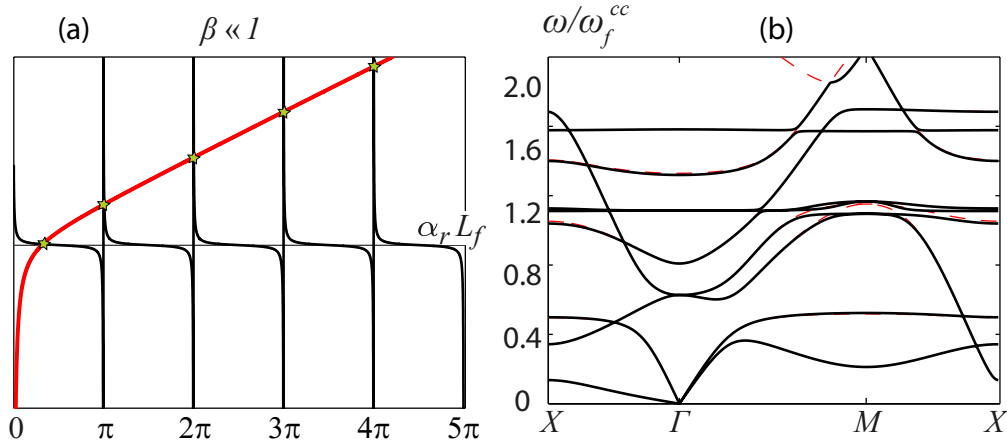


Figure 3.7 – Case 3 (refer to Table 3.1). Left (black line) and right-hand (red) sides (a) of Eq. (3.5), with corresponding band structure (b) depicting the FSI solution in solid black lines, and the structure-only case in red dashed lines. The ordinate is normalized with ω_f^{cc} .

Case 3

For case 3, $\alpha_0 L_f \sim \pi/2$ and two sub-cases are mathematically meaningful: $\beta \ll 1$ and $\beta \gg 1$. Physically however, the second case cannot be achieved while satisfying $\alpha_0 L_f \sim \pi/2$. The first case represents the coupling of fluid and structure with similar resonance frequencies. The left and right-hand sides of Eq. (3.5) intersect at $\alpha_1 L_f < \pi/2$, and $\alpha_r L_f = r\pi$ for $r = 2, 3, \dots$. The first resonant frequency of the coupled system is smaller but comparable to $\pi/2$, corresponding to ω_f^{oc} , while the subsequent resonances are those of a closed-closed tube. This phenomenon is well documented [Fahy and Gardonio, 2007] and is known as frequency splitting for enclosed volumes of fluid by deformable structures [Fahy and Gardonio, 2007]. For higher frequencies, the fluid contribution is significant only for resonant frequencies of the closed-closed tube at $\alpha_r L_f = r\pi$, as shown in Fig. 3.7(b). The rigid-wall boundary conditions on the tube result from antiresonances of the cell walls. Relative density for this configuration (Table 3.1) is also increased to ensure that $\omega_0 \gg \omega_f^{oc}$.

3.3.2 Comparison of analytical and FE models

Thin internal walls in cellular solids may resonate inducing strong dispersion even for wavelengths much smaller than the characteristic pore length L . The thicker solid phase in porous materials does not resonate, at least for the first several branches in the band structure, and dispersion is the result of Bragg scattering for wavelengths near L . Biot's theory has been validated for the macroscopic behavior in the latter regime. In a previous chapter (also in [Dorodnitsyn and Spadoni, 2014a]), we investigated the applicability of Biot's theory for cellular solids with $\rho^* \rightarrow 0$. We summarize our previous findings in Fig. 3.8 and we compare them with Eq. (3.12) for the phase velocity of pressure waves. Two FE models, based on beam and 4-node plane elements, are employed to investigate configurations with $1 \times 10^{-4} \leq \rho^* \leq 1$. The differences between the two element types are (i) plane elements are computationally very expensive for $\rho^* < 0.04$ while (ii) beam elements neglect deformations through the thickness (rigid cross-sections).

Starting with shear waves in the low-frequency regime (below any resonance), homogenized models for a square lattice without entrained fluid give [Dorodnitsyn and Spadoni, 2014a, Kumar and McDowell, 2004] $\sigma_{12} = E_s h^3 / L^3 \varepsilon_{12} = C_{44} \varepsilon_{12}$. The phase velocity of shear waves is obtained as $\sqrt{C_{44} / \bar{\rho}}$, where $\bar{\rho} = \rho_s \rho^* + (1 - \rho^*) \rho_f$. This model is in excellent agreement with FE results both for entrained air and water (Figs. 3.8(a-b)) which, for the properties selected here, represent $\rho_f \ll \rho_s$ and $\rho_f \sim \rho_s$ respectively. This homogenized model is appropriate since shear wavemodes in a square lattice are equivoluminal, and thus the contribution of the fluid is simply added mass, which is captured by $\bar{\rho}$. A comparison between Biot's theory [Dorodnitsyn and Spadoni, 2014a], FE results, and the homogenized model are in excellent agreement for cellular solids with $\rho^* \leq 0.3$ as shown in Fig. 3.8. For $\rho^* > 0.3$, the models diverge owing to the fact that we employ elastic constants from beam theory for both Biot's theory and the C_{44} .

In the case of pressure waves, the homogenized tube-piston model of Eq. (3.12) is in excellent agreement with the FE model based on beam elements for the entire range of ρ^* (Fig. 3.8(c)), but agreement deteriorates with the plane-element FE model and Biot's theory for $\rho^* > 0.1$ as a result of the limitations of beam theory. The FE model based on beam theory does not correctly account for reduction of the pore size as ρ^* increases (size h is just a parameter, and L is unchanged), in addition to neglecting deformations through the thickness. The limitations of beam theory become even more apparent if one considers water for which $\rho_f \sim \rho_s$ (Fig. 3.8(d)) where there is no agreement between beam-element FE model, Eq. (3.12), and either Biot's theory or plane-element FE model (Fig. 3.8(d)). We revisit and explain such limitations below in Sec. 3.4 where we explore in detail microstructural deformations. A last

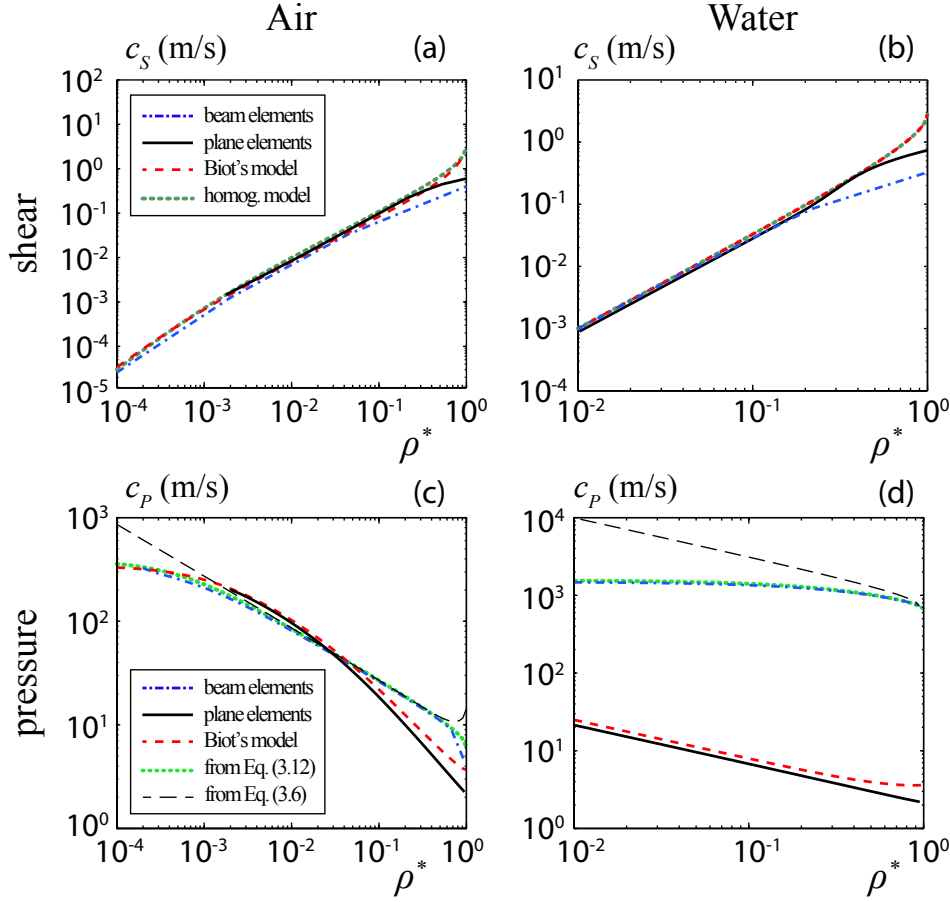


Figure 3.8 – Phase velocities for shear ((a) and (b)) and pressure ((c) and (d)) waves for entrained air ((a) and (c)) and water ((b) and (d)) for increasing relative density ρ^* . Solid, dashed-dotted, and thick dashed lines correspond to the FE results based on the plane elements, beam elements, and Biot's theory for plane conditions, respectively. The dotted lines in panels (a) and (b) correspond to equivalent-continuum models for shear waves based on C_{44} , which is defined in Sec. 3.3.2. The dotted lines in panels (c) and (d) correspond to the equivalent-continuum model for the pressure waves given by Eq. 3.12. The thin dashed lines in panels (c) and (d) denote the pressure-wave velocity obtained by employing Eq. 3.6. All velocity correspond to wavenumbers in the $\Gamma - X$ direction.

comment is due regarding the approximate solutions of Eqs. (3.6) and (3.7). Both perform very well for $0.0001 \geq \rho^* \leq 0.1$ (Fig. 3.8(c)), while the phase velocity predicted by Eq. (3.6) diverges for $\rho^* < 0.001$ since:

$$\lim_{\rho^* \rightarrow 0} c_P = \infty \text{ based on Eq. (3.6),} \quad (3.13)$$

$$\lim_{\rho^* \rightarrow 0} c_P = c_0 \text{ based on Eq. (3.7).} \quad (3.14)$$

The results for plane and beam-element FE models, as well as the results from tube-piston and Biot's models, converge in the fluid limit $\rho^* \rightarrow 0$. We attribute this behavior to the fact that lattices with infinitesimal relative density are mostly determined by the fluid phase, where only the bending of the walls contributes to the structural displacements.

3.4 Macro-Mechanical Equivalent Continuum Model

In this section, we propose an homogenized stiffness tensor C , describing the macrostructural behavior of the closed-cell lattice, for the low-frequency regime corresponding to case 1 above where $\alpha_0 L_f \ll \pi/2$. In general, we observe two wave modes (pressure and shear) below the first resonance of the lattice walls ($\omega/\omega_0 < 1$). This is the same as for a 2D continuum described by classical elasticity theory [Graff, 1975], which is defined by a second-order tensor. The closed cell lattice of Fig. 2.1 has simple cubic symmetry and the stiffness tensor is defined by three independent constants:

$$\begin{Bmatrix} \sigma_{11} \\ \sigma_{22} \\ \sigma_{12} \end{Bmatrix} = \begin{bmatrix} C_{11} & C_{12} & 0 \\ C_{12} & C_{11} & 0 \\ 0 & 0 & C_{44} \end{bmatrix} \begin{Bmatrix} \varepsilon_{11} \\ \varepsilon_{22} \\ 2\varepsilon_{12} \end{Bmatrix} \quad (3.15)$$

where C_{ij} are the effective stiffness constants. We develop next models for C_{11} and C_{12} required to completely define Eq. (3.15). C_{44} is defined in Sec. 3.3.2.

3.4.1 Homogenized model for C_{11} and C_{12}

We can once again employ a quasi-static model given that we are interested in the low-frequency regime $\bar{\omega} < 1$. We propose the model of a cavity bounded by deformable, simply-supported beams (Fig. 3.9).

The beams' rotations are coupled at $x_1 = 0$, $x_2 = L$, and pressure P_b depends on transverse deformations as:

$$P_b = -B_f \frac{\Delta V}{V} = -\frac{B_f}{L^2} \left(\int_0^L w_1(x_1) dx_1 + \int_0^L w_2(x_2) dx_2 \right). \quad (3.16)$$

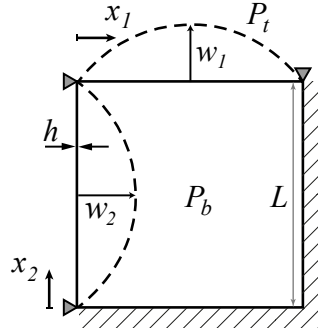


Figure 3.9 – Static model of a square cavity enclosed by simply-supported beams of thickness h , with internal P_b and external pressure P_t .

The coupled integro-differential equations governing beams' deformations are:

$$\begin{aligned} EI \frac{d^4 w_1}{dx_1^4} &= -P_b + P_t, \\ EI \frac{d^4 w_2}{dx_2^4} &= -P_b, \end{aligned} \quad (3.17)$$

with boundary conditions:

$$\begin{aligned} w_1(0) &= 0, & w_2(0) &= 0, \\ w_1(L) &= 0, & w_2(L) &= 0, \\ w_1''(L) &= 0, & w_2''(L) &= 0, \\ w_1'(L) &= w_2'(0), & w_1''(L) &= w_2''(0). \end{aligned} \quad (3.18)$$

Eqs. (3.17) can be solved by considering that the right-hand side, P_b is a definite integral with constant limits of integration. Differentiating Eqs. (3.17) by the corresponding spatial variable leads to two homogeneous fifth-order ODEs, whose general solution contains ten unknown constants. Substituting the general solution back into Eqs. (3.17) determines two constants. The remaining constants are evaluated with Eqs.(3.18). We do not present this general solution for brevity, however it is similar to the approach employed for solving the PDE in the next chapter and detailed in the Appendix. We define the average strain along x_1 and x_2 as:

$$\begin{aligned} \epsilon_{11} &= \frac{1}{L^2} \int_0^L w_1(x_1) dx_1, \\ \epsilon_{22} &= \frac{1}{L^2} \int_0^L w_2(x_2) dx_2. \end{aligned} \quad (3.19)$$

3.4. Macro-Mechanical Equivalent Continuum Model

From the stress-strain relation of Eq. (3.15), one has:

$$C_{12} = \frac{\sigma_{11}\epsilon_{22} - \sigma_{22}\epsilon_{11}}{(\epsilon_{22})^2 - (\epsilon_{11})^2}, \quad (3.20)$$

which, evaluated for $\sigma_{11} = 0$ and $\sigma_{22} = P_t$, gives:

$$C_{12} = 10^2 \frac{E_s I}{L^3} + B_f = 10^2 \frac{E_s}{12} (1 - \sqrt{1 - \rho^*})^3 + B_f. \quad (3.21)$$

The model is well posed for C_{12} as $\rho^* \rightarrow 0$.

The stiffness term C_{11} can simply be derived from the tube-piston homogenized model (Sec. 3.3.1). Along high-symmetry directions, say $[1\ 0]$, the phase velocity of pressure waves is simply $c_P = \sqrt{C_{11}/\bar{\rho}}$ [Wolfe, 2005]. Then from Eq. (3.12), one obtains:

$$C_{11} = 5 \times 10^2 \frac{E_s I}{L^3} + B_f = 5 \times 10^2 \frac{E_s}{12} (1 - \sqrt{1 - \rho^*})^3 + B_f, \quad (3.22)$$

where the only difference from C_{12} is the factor of 5 in the first term. For $\rho^* < 0.1$ however, the second term B_f dominates. All coefficients derived in this section are applicable to case 1 where $\alpha_0 L_f \ll \pi/2$.

3.4.2 Dispersion surfaces and slowness curves

Dispersion surfaces are obtained from the eigenvalue problem of Eq. (2.16) for $\mathbf{k} \cdot \mathbf{e}_r \in [-\pi, \pi]$, $r = 1, 2$ corresponding to the first Brillouin zone for a square lattice [Brillouin, 2003]. The dispersion surfaces for $\rho^* = 0.04$ ($h = 0.02L$) and $\rho^* = 0.75$ ($h = 0.5L$) are shown in Figs. 3.10(a-b) respectively. The dispersion surfaces which correspond to the case 2, studied in the Sec. 3.3.1 and depicted in Fig. 3.6, are provided in Fig. 3.11 for $\beta \ll 1$ (a), and $\beta \gg 1$ (b). We note the cubic symmetry in dispersive regions, and the difference in gradients between the first surface (shear mode) and the second surface (pressure mode). The band structure is represented by black lines, confirming the validity of the results presented in previous sections.

Dispersion surfaces obtained from FE models allow the determination of anisotropy by defining the slowness vector $\mathbf{s} = \mathbf{k}/\omega|_{\omega_0}$ at a given frequency ω_0 [Wolfe, 2005]. The slowness vector has magnitude $\|\mathbf{s}\| = 1/c_\alpha(\mathbf{k})$, with $\alpha = S, P$ indicating shear and pressure modes. Equilibrium at the macroscale requires:

$$\nabla_j \sigma_{ij} = \bar{\rho} \ddot{u}_i, \quad (3.23)$$

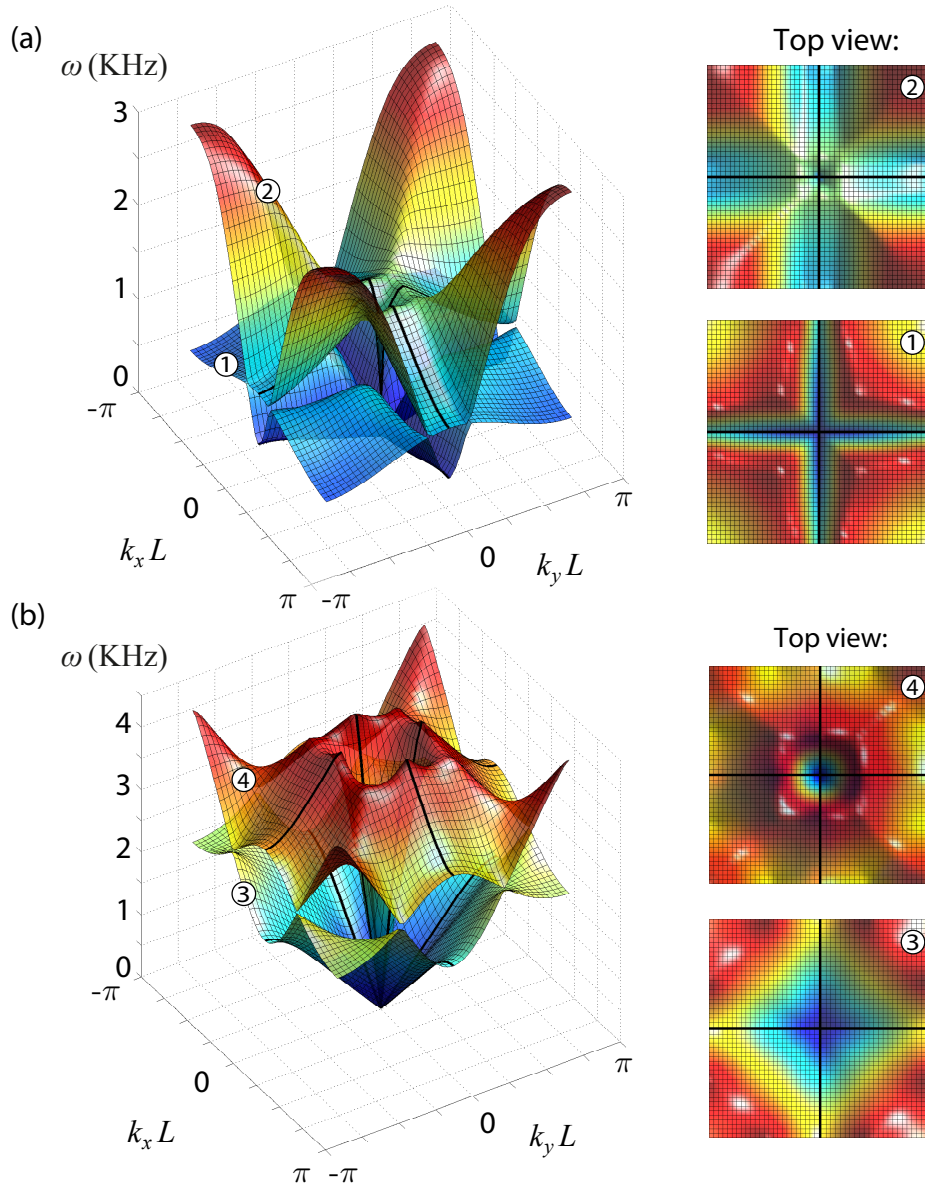


Figure 3.10 – Dispersion surfaces (a) for $\rho^* = 0.04$ (case 1 from Table 3.1), and (b) for $\rho^* = 0.75$ in the (k_x, k_y, ω) -domain, where $|k_x| \leq \pi$ and $|k_y| \leq \pi$. Shear mode surfaces are labeled with circled numbers (1) and (3), while pressure mode surfaces with (2) and (4). Top view of each of the surfaces is provided in the right side of the figure.

where the microstructural stress is defined in Eq. (3.15). Assuming plane harmonic waves with amplitude $\hat{\mathbf{u}}$, one obtains [Wolfe, 2005]:

$$(D_{il} - c_\alpha^2 \delta_{il}) \hat{\mathbf{u}} = \mathbf{0}, \quad (3.24)$$

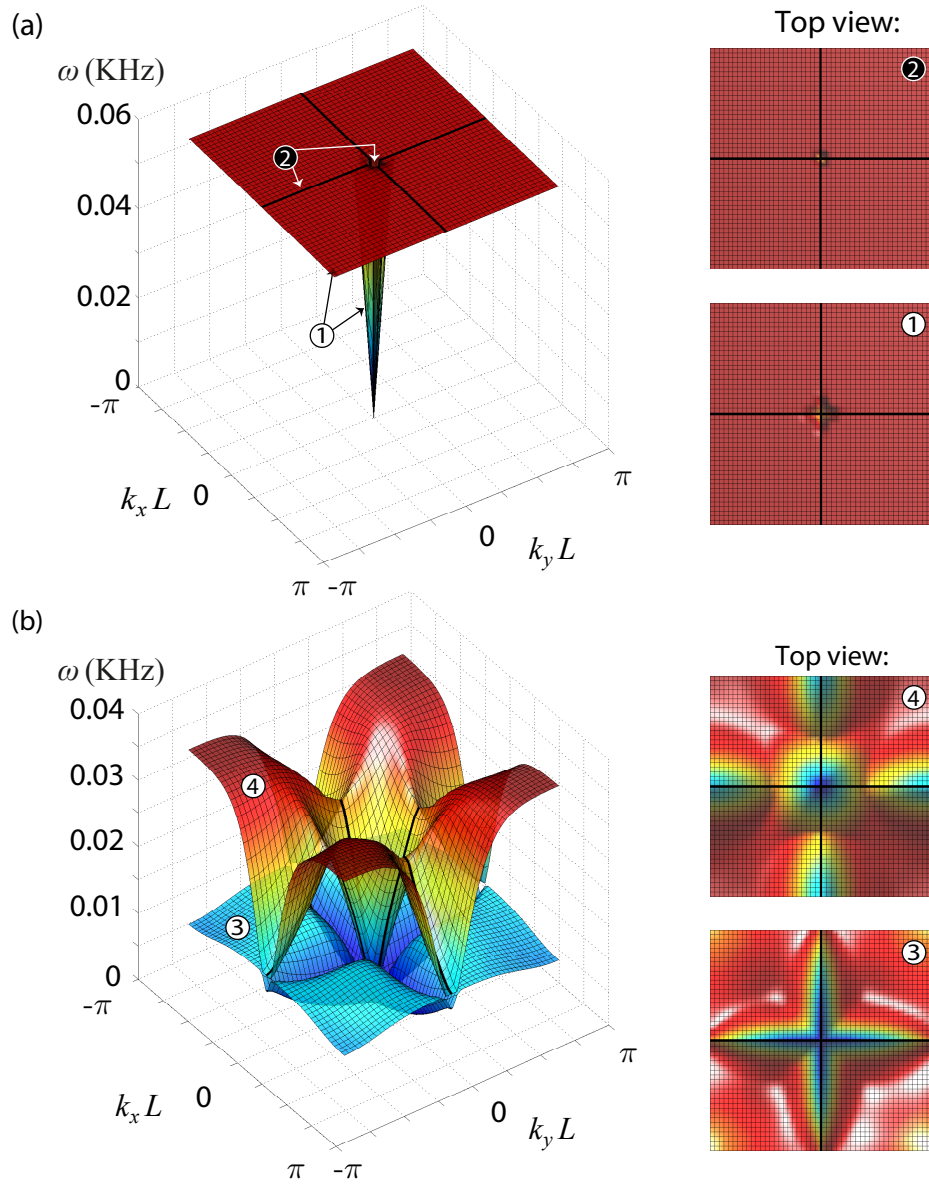


Figure 3.11 – Dispersion surfaces corresponding to case 2 (Table 3.1) for (a) $\beta \ll 1$, and (b) $\beta \gg 1$ in the (k_x, k_y, ω) -domain, where $|k_x| \leq \pi$ and $|k_y| \leq \pi$. Shear mode surfaces are labeled with circled numbers (1) and (3), while pressure mode surfaces with (2) and (4). Top view of each of the surfaces is provided in the right side of the figure.

where:

$$D_{il} = \frac{1}{\bar{\rho}} C_{ijklm} \frac{k_j}{\|\mathbf{k}\|} \frac{k_m}{\|\mathbf{k}\|}, \quad (3.25)$$

is the Christoffel matrix (Einstein notation is used), $\|\mathbf{k}\|$ is the wavenumber, and $\mathbf{k}/\|\mathbf{k}\|$ are components of the direction vector; D_{il} relates elastic constants to the phase velocities of

Chapter 3. Numerical and Homogenized Analysis of Pressure Waves

wavemodes [Auld, 1973, Wolfe, 2005]. The eigenvalues of Eq. (3.24) define the phase velocity c_α , from which the slowness curve is obtained.

Eq. (3.24) can be solved analytically expressing the wavevector \mathbf{k} in terms of magnitude and angle γ :

$$\mathbf{k} = \|\mathbf{k}\| \{\cos \gamma, \sin \gamma\}^T. \quad (3.26)$$

With this definition, the eigenvalue problem of Eq. (3.24) is solved for c_α :

$$c_\alpha = \frac{1}{2\bar{\rho}} \left(C_{11} + C_{44} \mp \sqrt{(C_{11}^2 - 2C_{44}C_{11}) \cos^2 2\gamma + (C_{12}^2 + 2C_{44}C_{12}) \sin^2 2\gamma + C_{44}^2} \right) \quad (3.27)$$

Note that $C_{11} \gg C_{44}$ (Eqs. (3.21) and (3.22)), consistent with the fact that longitudinal waves produce greater restoring force due to local change of volume than shear waves, especially in the presence of fluid. Eq. (3.27) can be simplified further:

$$c_\alpha = \frac{1}{2\bar{\rho}} \left(C_{11} \mp \sqrt{(C_{11})^2 \cos^2 2\gamma + (C_{12})^2 \sin^2 2\gamma} \right). \quad (3.28)$$

This expression of the phase velocity is compared next to numerical estimates from our FE models.

Slowness curves for shear and pressure modes for a square lattice with entrained air are shown in Figs. 3.12(a-b) for $\rho^* = 0.04$, and Figs. 3.12(c-d) for $\rho^* = 0.75$. These values of relative density represent a cellular and a porous medium respectively corresponding to case 1 $\alpha_0 L_f \ll \pi/2$. The agreement between numerical (dashed lines) and analytical results (solid lines) is excellent for all angles (Figs. 3.12(a-d)). Furthermore, shear waves are anisotropic, even in the low frequency regime, and their spatial characteristics depend on ρ^* . Pressure waves, on the other hand are isotropic, and significantly faster than shear waves. This is in agreement with Fig. 3.1 and $C_{44} \ll C_{11}$. Isotropic pressure waves are obtained if $C_{11} \simeq C_{12}$, which is certainly the case of Eqs. (3.21) and (3.22). The proposed tube-piston model is thus applicable for any propagation direction.

For case 2 with $\alpha_0 L_f \gg \pi/2$, slowness curves are shown in Figs. 3.12(e-f) for $\beta \ll 1$ and $\beta \gg 1$ corresponding to low-density/soft and high-density/stiff entrained fluid respectively. In both cases, the shear wave is highly directional, and much slower than the pressure wave.

3.4. Macro-Mechanical Equivalent Continuum Model

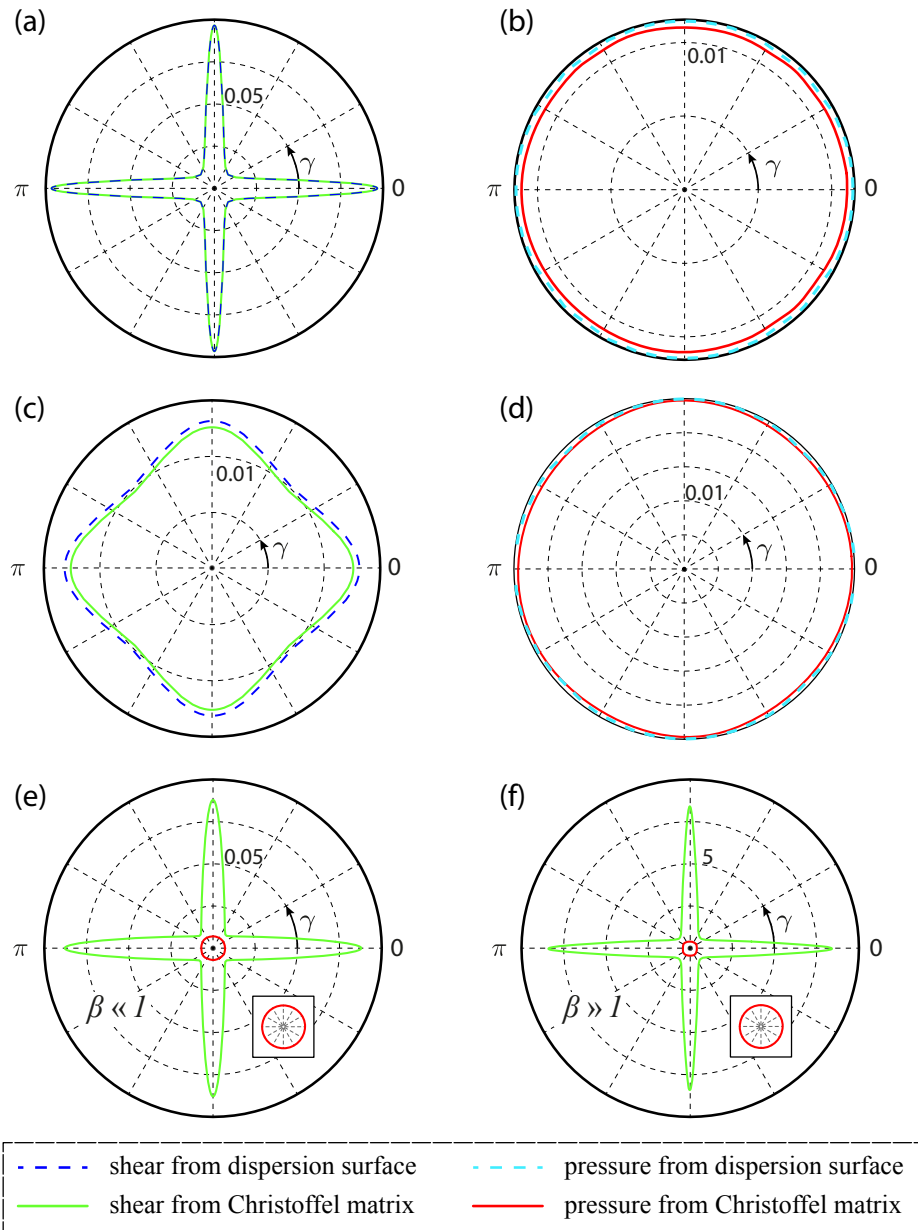


Figure 3.12 – Slowness curves (in s/m) for shear (green) and pressure waves (red). Case 1 $\alpha_0 L_f \ll \pi/2$ $\rho^* = 0.04$ ((a) and (b)) and $\rho^* = 0.75$ ((c) and (d)); Case 2 $\alpha_0 L_f \gg \pi/2$ with $\beta \ll 1$ ($\rho^* = 0.08$) (e) and $\beta \gg 1$ ($\rho^* = 0.2$) (f). All curves are evaluated for the constant frequency $\omega_0 = 10$ Hz. In (a) and (c), green solid and dark blue dashed lines denote respectively the shear slowness from Christoffel matrix (Eq. (3.24)) and from dispersion surfaces obtained with plane elements. In (b) and (d), red solid and light blue dashed lines denote pressure slowness. Panels (e) and (f) correspond to case 2 (Table 3.1) for $\beta \ll 1$ and $\beta \gg 1$, respectively. Enlarged pressure slowness curves are superposed with insets in panels (e) and (f).

3.4.3 Extreme behavior of the pressure wave phase velocity

The dependency of the phase velocity of the pressure wave on the relative density is discussed in detail in [Dorodnitsyn and Spadoni, 2014a], and summarized in Sec. 3.3.2 for $\bar{\omega} \ll 1$. In addition to having a relation between macrostructural behavior and geometric and material properties, it is important to understand the deformation mechanisms of the microstructure. For this reason, the phase velocity of pressure waves is computed for an extended range of relative density $1 \times 10^{-8} \leq \rho^* \leq 1$. We employ Biot's theory given its excellent performance, discussed in Sec. 3.3.2, to explore regimes of ρ^* which would be challenging for FE models. Air and water are considered as the entrained fluid to analyze the contribution of ρ_f versus ρ_s . In general for case 1 ($\alpha_0 L_f \ll \pi/2$), three distinct deformation-mechanism regimes exist (Fig. 3.13). In the limit $\rho^* \rightarrow 0$, microstructural deformations are of bending type (Fig. 3.1(a)). For the piston-tube model of Sec. 3.3.1, the structural natural frequency ω_0 is simply that of a clamped-clamped beam. The phase velocity in the bending regime, furthermore, is logarithmically constant with respect to ρ^* as $\rho^* \rightarrow 0$ and correctly converges to the speed of sound in the fluid phase $c_0 = \sqrt{B_f/\rho_f}$. This first regime is labeled by the circled number 1 in Figs. 3.13(a-b).

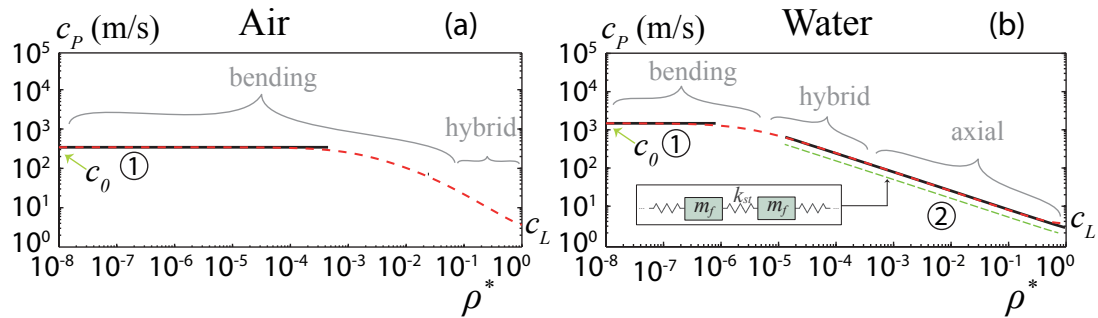


Figure 3.13 – Phase velocities for pressure waves for entrained air (a) and water (b) for $10^{-8} \leq \rho^* \leq 1$ in logarithmic scale. Thin red dashed line denotes Biot's theory. Circled numbers label logarithmically linear regimes of c_p (black solid straight lines). Green dashed line is the approximation of the pressure phase velocity (Eq. 3.29), given by spring-mass model superposed in (b). The gray font labels schematically depict the ranges of different structural deformation behaviors. Studied frequencies belong to non-dispersive range at each value of ρ^* .

For intermediate values of ρ^* , microstructural deformations include bending and through-the-thickness modes (Fig. 3.14(a)). We denote this as the hybrid regime for which simple analytical models of ω_0 do not exist. Among other shortcomings, beam theory neglects any deformations through the thickness (rigid-cross-section assumption) and cannot predict hybrid deformations. This limitation contributes to the discrepancy between analytical and

3.4. Macro-Mechanical Equivalent Continuum Model

beam-based FE models in Fig. 3.8. Since this regime takes place for different values of ρ^* depending on the ratio ρ_s/ρ_f , we conclude that microstructural deformation mechanisms are determined by mass coupling. For light entrained fluid like a gas, mass coupling is small and deformations are of bending-type for $\rho^* < 0.1$ and hybrid-type for $\rho^* \geq 0.1$. For heavy entrained fluid, the bending regime is confined to extremely small values of ρ^* .

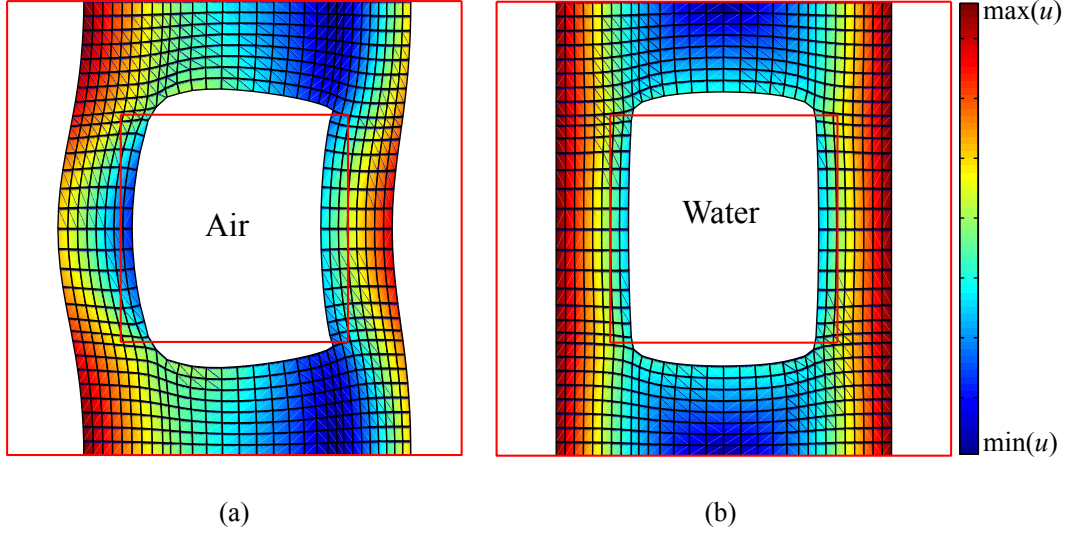


Figure 3.14 – Fluid-structure (FSI) wave modes of a square unit cell with $\rho^* = 0.75$ for (a) air, and (b) water, corresponding to the wavevector \mathbf{k} along x -axis with $k_x = 0.03\pi$, $k_y = 0$. Solid red lines denote the initial configuration. The change in color corresponds to the standard Euclidean norm of the structural displacement vector $u = \sqrt{u_x^2 + u_y^2}$.

For heavy entrained fluid, a third regime exists with through-the-thickness deformations. For values of relative density $\rho^* > 1 \times 10^{-5}$, pressure waves produce the deformations of Fig. 3.14(b). In this case, the entrained fluid can be considered as a heavy and stiff inclusion contributing most of the kinetic energy of pressure waves, with strain energy confined to the solid phase. A simple model for this regime is a chain of springs and masses (inset in Fig. 3.13(b)), with mass and stiffness given by the considerations just above. Accordingly, the spring stiffness is approximated as $k_{eff} = E_s A/h = E_s L/h$ and the effective mass is that of the fluid $m_{eff} = \rho_f L^2$. Then, from Eqs. (3.11) and (3.12), the phase velocity of the pressure waves in the long-wavelength limit is:

$$c_P \sim \sqrt{\frac{E_s L}{\rho_f h}} = \sqrt{\frac{E_s}{\rho_f} \frac{1}{(1 - \sqrt{1 - \rho^*})}}. \quad (3.29)$$

This model correctly captures the logarithmic dependence of the phase velocity in the third regime for $\rho^* > 1 \times 10^{-5}$ (green dashed line in Fig. 3.13(b) labeled with the circled number 2).

The offset between Biot's theory and Eq. (3.29) can be attributed to the fact that the solid phase does contribute some mass and the portion of a cell face participating in the deformation is smaller than L , increasing the effective stiffness.

3.5 Conclusion

Wave propagation in media with microstructure is characterized by strong scattering. In porous media, periodic or not, dispersion arises when wavelengths match some characteristic size of the pores or their distribution and not from the resonant frequency of the entrained gas, at least in the acoustic branch. In cellular solids, the solid phase occupies a small portion of the total volume and may resonate at relatively low frequency. In addition to the size of cavities, resonant scattering contributes to wave dispersion. Significant research has been devoted to wave propagation in cellular solids, but the contribution of entrained fluid has been analyzed via phenomenological, macrostructural models such as Biot's theory. In this chapter, the contribution of entrained fluid is investigated with FE models of a representative volume element, explicitly considering fluid-structure interactions. The entrained fluid is considered inviscid, and both heat conduction and convection are neglected, leading to an acoustic model for cavities. The analogy of a cavity with an equivalent tube is here extended to consider the coupling with deformable boundaries given by structural walls. The periodicity of the considered 2D square lattice allows the derivation of a homogenized model based on computed microstructural deformations.

Wave propagation can be categorized in terms of wall, cavity, and coupled-system resonance frequencies. When the cavity frequencies are higher than wall frequencies, the entrained fluid increases effective stiffness and contributes added mass. A tube-piston model based on computed microstructural deformations accurately describes propagation away from resonances, so long as deformations are of bending type. The same tube model allows the derivation of effective mechanical properties at the macroscale in terms of geometric and material properties. For a square lattice, shear wavemodes are equivoluminal and thus can be modeled with previously derived models. We find that pressure waves are isotropic both for cellular $\rho^* < 0.3$ and porous regimes $\rho^* \geq 0.3$, where ρ^* is the relative density. We complete the macrostructural stiffness description by deriving C_{12} relating stress σ_{11} to strain ε_{22} , and we find excellent agreement with computed phase velocities for shear and pressure modes for all angles. Given the cubic symmetry of the square lattice, the shear wavemode is anisotropic for all considered values of ρ^* and type of entrained fluid.

The proposed homogenized model requires knowledge of the wall resonance frequency. While physically appropriate for $\rho^* \in [0, 1)$, the proposed piston-tube model is not easily extended to relatively large values of ρ^* , owing to the microstructure undergoing bending and through-the-thickness deformations. In this regime, the resonance frequency of the walls cannot be evaluated from beam theory. The onset of bending and through-the-thickness deformation mechanisms is determined by mass coupling. For heavy entrained fluid, through-the-thickness-only deformations are observed, while for light entrained fluid, hybrid modes encompassing both deformation modes are possible. Accordingly, we employ both beam and plane elements to discretize the solid phase of the lattice.

Wave dispersion is also affected by cavity resonances. In the case this is lower than wall resonance, one has two scenarios: (i) cavity resonances described by a closed-closed tube for a light and soft entrained fluid; (ii) cavity resonances described by an open-closed tube for a heavy fluid. An additional regime is given by coincident cavity and wall-resonance frequency. In this, the classic phenomenon of frequency splitting is observed. Finally, we find Biot's theory to be in excellent agreement with numerical models of both cellular and porous media. Biot's theory however requires effective mechanical properties for the solid phase with and without entrained fluid; particularly the effective bulk and shear moduli. While these properties do exist for a square lattice, this is not the case for more complex cellular solids, especially in 3D. The piston-tube model we propose, on the other hand, only requires the resonant frequency of the walls, and thus should easily be extended to 3D (refer to Sec. 6.2).

In the next chapter the limitation on the low, undisperced frequency ranges is removed by introducing the full analytical model valid for any wavelengths. The analysis is devoted to the pressure waves, with the specific focus on the coexistence of slow and fast P-waves within the certain frequency bands. For that the Rayleigh energy approach is considered.

4 Analytical Analysis of Slow and Fast Pressure Waves

The material presented in the chapter are accepted for publication in JASA Special Issue on Acoustic Metamaterials, 2016.

4.1 Introduction

This chapter presents an analytical study of pressure waves in the system investigated numerically in the previous chapter. The medium is considered as an acoustic metamaterial subjected to plane-harmonic-waves analysis. As it was shown previously, three longitudinal waves are identified from a finite element (FE) model: one slow and two fast pressure waves. The slow one is one order of magnitude slower than the both fast ones, which propagate at the same rate in the non-dispersive regimes. The slow pressure wave is only generated in case the cells are filled with a fluid and propagates only in the high frequency range above the odd structural resonant frequency. The goal is to derive an equivalent continuum which predicts behavior found in the full numerical model for pressure waves in the $\Gamma - X$ direction. The model predicts the existence of both fast and slow longitudinal wavemodes and the correct deformations of the walls. This is done in three steps. First, in Sec. 4.2, a simplified finite-element model is introduced, in which the wave number is included in the material parameters. Second, a fully analytical mechanical model of the microstructure is described in Sec. 4.3. Finally, in Sec. 4.4, the pressure wave modes are investigated using Rayleigh's energy approach. It is an elegant method to characterize the difference between slow and fast longitudinal waves, and to introduce the phase velocity analysis.

The full FE model displayed further echoes the one from Chapter 2. The band-structure shown in Fig. 4.1(c), limited to the path $\Gamma - X$ in the first Brillouin Zone (i_1 -direction of direct space

Chapter 4. Analytical Analysis of Slow and Fast Pressure Waves

(Fig. 4.1(a)), is computed for two cases: drained (structure-only, STO) and filled with fluid (fluid-structure interaction, FSI). The $\Gamma - X$ limitation is sufficient due to the isotropic behavior of pressure waves subjected to the current analysis (as was established in Sec. 3.4.2). An RVE from Fig. 4.1(b) is consistent with the Timoshenko beam formulation studied previously (Sec. 2.2.1). Material and geometrical parameters are listed in Tab. 4.1.

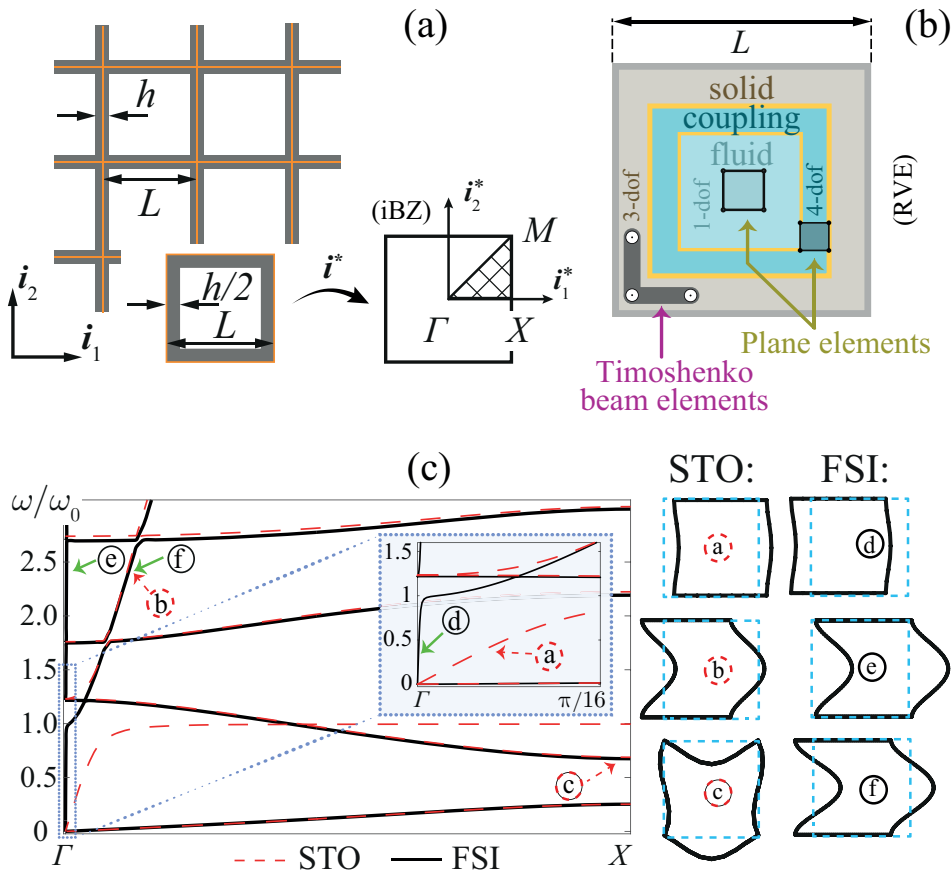


Figure 4.1 – Square lattice with wall thickness h and cell length L and unit cell (a). RVE with solid portion discretized by 3-dof beam elements (b). Coupling elements with both structural and pressure dofs are used to model fluid-structure interaction. Band structure (c) for an infinite cellular material along the Γ, X path in the iBZ. The angular frequency ω is normalized by the first natural frequency of a clamped-clamped beam ω_0 . Circled letters (a) - (c) and (d) - (f) denote wave number - frequency combinations used to depict the deformed configurations of wave modes in STO and FSI cases, respectively.

The calculated cell deformations of some relevant pressure ((d) - (f), (a) - (b)) and shear waves ((c)) are shown in Fig. 4.1(c). It can be seen that the vertical wall deflections related to pressure waves are described by modeshapes comparable a clamped-clamped beam. Due to the hydrostatic loading imparted by the fluid, only symmetric (odd) mode shapes occur.

4.2. Simplified Finite-Element Approach of P-waves

Table 4.1 – Material and geometrical properties are in accordance with Chapter 2 and [Dorodnitsyn and Spadoni, 2014a].

	Relative density ρ^*	fluid bulk modulus β (Pa)	fluid density ρ_f (kg/m ³)	structural Young's modulus E_s (kPa)	structural density ρ_s (kg/m ³)
FSI	0.04	142 000	1.2	1	1000
STO	0.04	0	0	1	1000

The horizontal walls are not bent. This has been proved in [Dorodnitsyn and Spadoni, 2014a], where it is shown that a pure longitudinal compression of the walls guarantees minimum energy in the RVE. On the other hand, shear modes require the bending of both horizontal and vertical walls [Dorodnitsyn and Spadoni, 2014a]. For higher-energy shear waves (c) the antisymmetric (even) modes of a clamped-clamped beam are allowed [Dorodnitsyn and Spadoni, 2014b].

In this chapter, we develop an analytical model to predict the pressure wave behavior in the geometry previously studied numerically (Fig. 4.1 and Tab. 4.1). The goal is to understand the origin of the slow pressure wave, by studying an equivalent continuum which matches the full numerical model for pressure waves in the Γ , X direction. The analytical description has to predict both the dispersion behavior and the cell deformations. This is done in three steps. First, in Sec. 4.2, a simplified finite-element model is introduced. This shows that the explicit fluid-structure interaction can be replaced by including the wave number in the material parameters. Second, a fully analytical mechanical model of the microstructure is described in Sec. 4.3. Finally, in Sec. 4.4, the pressure wave modes are investigated using Rayleigh's energy approach. It is an elegant method to characterize the difference between slow and fast longitudinal waves, and to introduce the phase velocity analysis.

4.2 Simplified Finite-Element Approach of P-waves

This section introduces a simplification of the FE matrices of a representative model for pressure waves (P-waves). In [Dorodnitsyn and Spadoni, 2014b] the authors extensively investigated P-waves using the Christoffel matrix, showing the longitudinal modes to propagate in an isotropic way. Thus, we can limit the analytical study to the $\Gamma - X$ direction without loss of generality. Using the observations of the wall deformations given earlier, one can simplify the considered RVE as follows: two beams are aligned perpendicularly to the direction of the wave vector \mathbf{q} . They are connected by an effective spring, employed to simulate a distributed

fluid force, and connecting each node in the left beam to every node in the right beam. Since the horizontal walls of the square cell are only deformed longitudinally, they can be replaced by a one dimensional spring with spring constant $k = EA/L$. A schematic model is shown in Fig. 4.2(a).

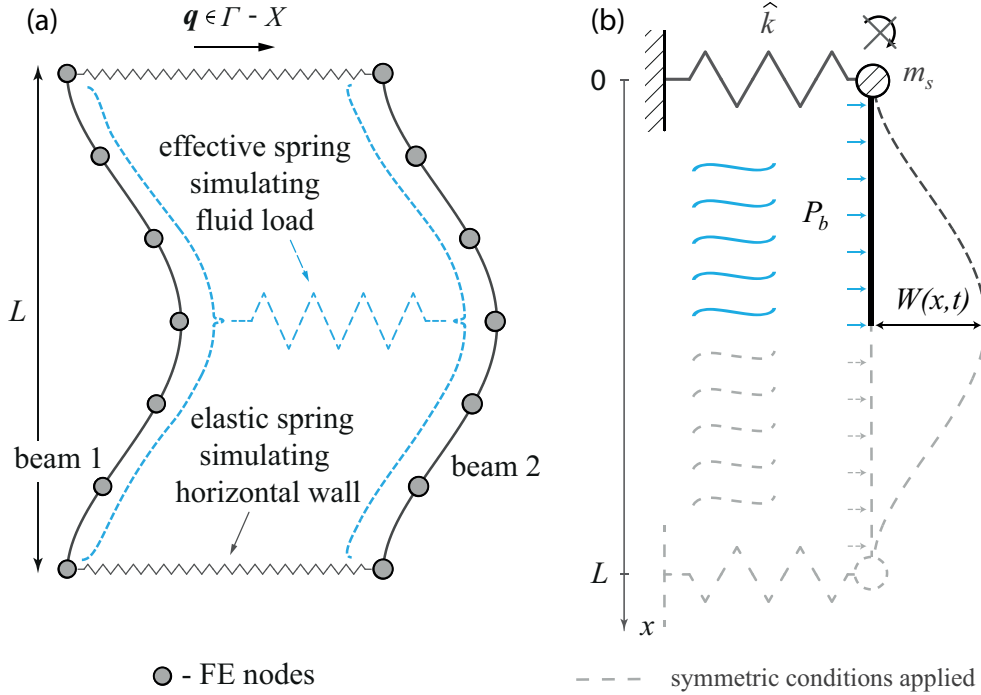


Figure 4.2 – (a): Simplified finite-element model (Ψ -model). The direction of the wave vector q is depicted by the black solid arrow. Walls parallel to the wave propagation are modelled by elastic springs, fluid load is replaced by a distributed effective spring. (b): Equivalent-continuum model. An effective force P_b couples motion of fluid and structure phases. The walls parallel to the direction of wave propagation are modeled by lumped masses m_s and springs with the wavevector-dependent stiffness \hat{k} . The boundary conditions are forced to be symmetric at $x = 0$ and $x = L$.

The stiffness matrix of this model (further referred to as Ψ -model) can be written as

$$[K] = \begin{bmatrix} K_{11} + \beta\Psi_n & K_{12} - \beta\Psi_n \\ K_{21} - \beta\Psi_n & K_{22} + \beta\Psi_n \end{bmatrix}, \quad (4.1)$$

where K_{11} and K_{22} are the stiffness matrices of beams 1 and 2, and $K_{12} = K_{21}^T$ stands for the stiffness of the horizontal springs which represents the elastic coupling. The only nonzero component in the coupling terms is $k = EA/L$ representing the actual rigidity of the parallel walls. Ψ_n is a square matrix of order n with all elements being equal to $1/n$ and n is the number of dofs per beam. Introducing the fluid's compression modulus β , this correction

4.2. Simplified Finite-Element Approach of P-waves

for the STO stiffness matrix captures the hydrostatic pressure load. The effective elastic connection replacing the fluid is chosen massless, therefore the mass matrix for the Ψ -model is identical to the one from the FE model. By plugging the stiffness and mass matrices into Bloch's theorem to impose periodic boundary conditions [Kittel, 2004], one finds the reduced matrices

$$\begin{aligned} [K_r] &= T^T [K] T, \\ [M_r] &= T^T [M] T. \end{aligned} \quad (4.2)$$

In this notation

$$T = \begin{bmatrix} I_n \\ I_n \cdot e^{jq} \end{bmatrix} \quad (4.3)$$

is the transformation matrix expressing the symmetry conditions [Cook, 2001, Chapter 12]. I_n is the identity square matrix of order n , q is the nondimensional wave number, and $j^2 = -1$. Substituting the reduced stiffness and mass matrices into Eqs. (4.2) yields

$$\begin{aligned} [K_r] &= [\tilde{K}_s] + \beta \Psi_n (1 - \cos(q)) = [\tilde{K}_s] + \hat{\beta} \Psi_n, \\ [M_r] &= [\tilde{M}_s], \end{aligned} \quad (4.4)$$

where $[\tilde{K}_s] = K_{11} + K_{22} + 2K_{12} \cos(q)$ and $[\tilde{M}_s] = M_{11} + M_{22} + 2M_{12} \cos(q)$ are the reduced STO matrices (corresponding to the case of $\beta = 0$). According to Eqs. (4.4), an effective bulk modulus can now be defined as

$$\hat{\beta} = \beta (1 - \cos(q)). \quad (4.5)$$

This is an important finding since the influence of the fluid on the wave propagation is now stored in just one additional term. This property will be used further to develop the analytical model.

The resulting band-structure for the Ψ -model is compared to the one for the full FE model in Fig. 4.3. A good agreement in the low frequency ranges for both (a) STO and (b) FSI cases can be verified. Moreover, from the comparison of STO and FSI band structures the existence of the slow P-wave in the presence of the fluid is confirmed. The flat lines next to $\omega/\omega_0 = 3$ indicate the propagation of the wave to be direction independent (captured by both full FE and Ψ -model), which points out the presence of resonance. The Ψ -model statement does not capture the shear waves since the necessary horizontal wall bending is neglected. The higher

frequency discrepancy can be attributed to the way the Ψ -model has been defined: the fluid does not influence the model mass matrix, as it is the case in the full FE system. Therefore, the effective mass of the Ψ -model is lower which makes the P-waves to be slightly slower in the high frequency regimes than in the full FE model.

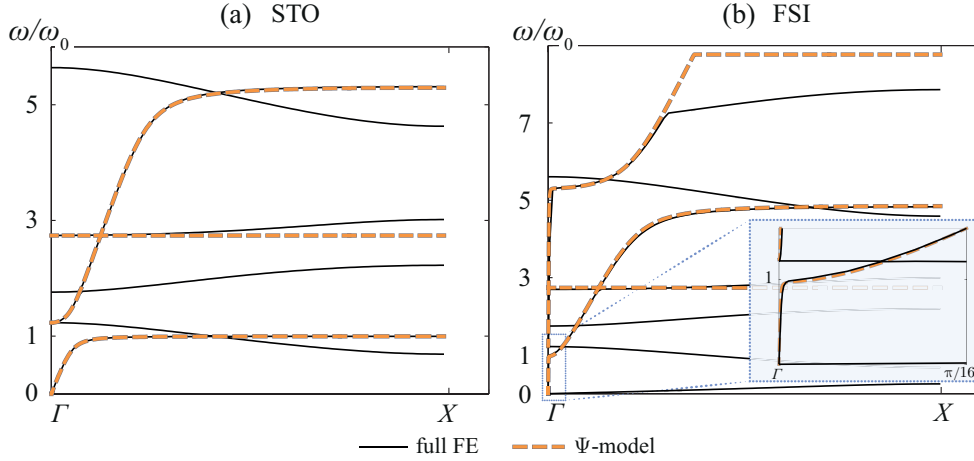


Figure 4.3 – Comparison of two band-structures in the direction $\Gamma - X$: full FE model from Fig. 4.1(c) (black solid lines) and Ψ -model (orange dashed lines). The STO case is depicted in (a), FSI in (b). The ordinate ω is normalized by the first natural frequency of a clamped-clamped beam, ω_0 .

4.3 Analytical dispersion relation of P-wave Propagation

In this section we develop an analytical model that matches the numerical models and allows for a physical interpretation of the system behavior. The derivations in Sec. 4.2 are used to develop a micro-mechanical model composed of a thin beam with elastic supports (Fig. 4.2(b)). Based on the clamped-like modeshapes of the P-waves (Fig. 4.1), the rotation of the beam ends is restricted. The skeleton members parallel to the direction of the wave propagation are substituted by a combination of two lumped masses and elastic spring supports. These springs allow the rigid body translation and are characterized by the effective wave-dependent stiffness \hat{k} determined analogically to effective bulk modulus from Eq. (4.4)

$$\hat{k} = \hat{k}(q) = k(1 - \cos(q)) = \frac{EA}{L}(1 - \cos(q)). \quad (4.6)$$

The masses $m_s = \rho_s AL$ take into account the coupling of two beams in the junction.

4.3. Analytical dispersion relation of P-wave Propagation

Additionally, an effective hydrostatic fluid force P_b couples the motion of both phases: P_b depends on the transverse deformations $W(x, t)$ of the beams. Therefore, in a cell with unitary out-of-plane thickness, it can be described as an external distributed force

$$P_b = -\widehat{\beta} \frac{\Delta V}{V} = -\frac{\widehat{\beta}}{L^2} \int_0^L W(x, t) dx, \quad (4.7)$$

where $\widehat{\beta} = \widehat{\beta}(q)$ is given by Eq. (4.5). Eq. (4.7) can be immediately derived from the definition of the bulk modulus taking into account that the change in volume is provided by the lateral displacement of the beam.

From the aforesaid, the governing integro-differential equation becomes

$$EI \frac{\partial^4 W(x, t)}{\partial x^4} + \rho_s A \frac{\partial^2 W(x, t)}{\partial t^2} - P_b = 0, \quad (4.8)$$

Two physical boundary conditions, expressing the rotation-free behavior and the shear force at $x = 0$ can be written as

$$\begin{aligned} W'(0, t) &= 0, \\ EI W'''(0) &= -\widehat{k}(q) W(0, t) - m_s \ddot{W}(0, t). \end{aligned} \quad (4.9)$$

Moreover, the symmetric deformation implies

$$\begin{aligned} W(0, t) &= W(L, t), \\ W'(0, t) &= W'(L, t). \end{aligned} \quad (4.10)$$

Under these conditions, the shear force condition is automatically fulfilled in $x = L$.

Assuming a harmonic solution with amplitude $w(x)$,

$$W(x, t) = w(x) e^{i\omega t}, \quad (4.11)$$

the governing Eq. (4.8) becomes

$$w''''(x) - \alpha^4 w(x) + \frac{\widehat{\beta}(q)}{EIL^2} \int_0^L w(x) dx = 0, \quad (4.12)$$

where $\alpha^4 = \omega^2(\rho_s A)/(EI)$, and α being the well-known wave number for bending waves in

Chapter 4. Analytical Analysis of Slow and Fast Pressure Waves

thin beams. The boundary conditions Eqs. (4.9-4.10) are transformed to

$$w(0) = w(L), \quad (4.13a)$$

$$w'(0) = w'(L) = 0, \quad (4.13b)$$

$$EIw'''(0) = -(\hat{k}(q) - \omega^2(q)m_s)w(0). \quad (4.13c)$$

The equation of motion Eq. (4.12) can be solved using the standard technique for homogeneous differential equations with boundary conditions. Details are provided in Appendix A.1. The resulting dispersion relation is shown in Fig. 4.4.

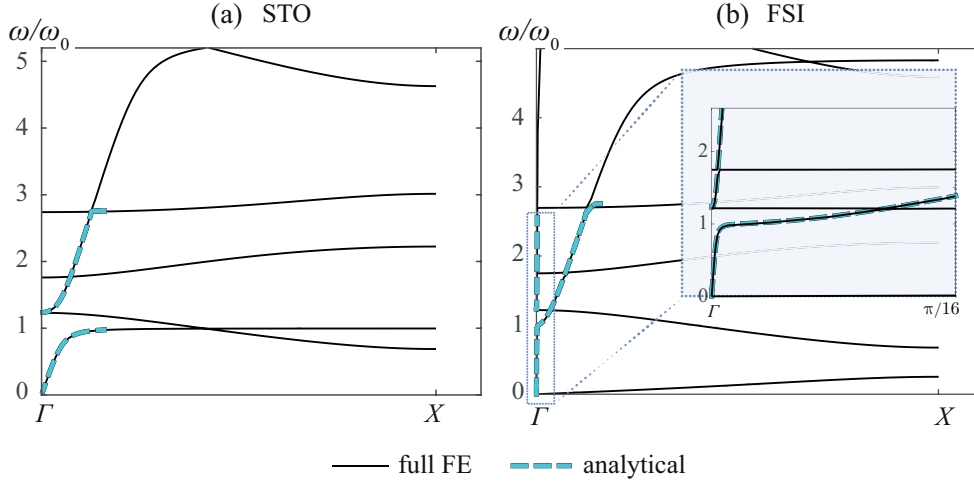


Figure 4.4 – Comparison of two band-structures: full FE model from Fig. 4.1(c) (black solid lines) and fully analytical model (blue dashed lines): (a) for STO and (b) for FSI.

At this end one notices the fact that Bloch's theorem was not imposed explicitly whereas it is embedded into the material parameters $\hat{k}(q)$ and $\hat{\beta}(q)$ in accordance with Sec. 4.2. Without loss of generality, the wavenumber is further limited to $0 \leq q \leq 0.5$ which is computationally sensible and stays within the long-wavelength stipulation. As one can see from Fig. 4.4, the resulting analytical band-structure agrees perfectly with the one from the FE model for both cases: FSI (a) and STO (b). In the STO case, $\hat{\beta} = 0$, Eq. (4.12) is reduced to the Euler-Bernoulli beam equation for thin beams assuming no shear force variation through the thickness. The resulting curves match the Euler beam solution with clamped boundaries [Hodges and Pierce, 2011, Chapter 2]. Altogether, this confirms that for the first modes, the analytical model can be considered instead of the FE simulations.

4.4. Rayleigh Quotient Analysis of the Analytical System

From the analytical model, the group velocity of the P-waves can be calculated explicitly. The analytical characteristic equation can be denoted as $f(\alpha, q) = 0$. Then its differentiation leads correspondingly to the group velocity of the i^{th} mode

$$c_g^{(i)}(q) = \frac{\partial \omega_i}{\partial q} = \frac{\partial \omega_i}{\partial \alpha_i} \frac{d\alpha_i}{dq} = -2\alpha_i L \sqrt{\frac{EI}{\rho_s A}} \frac{\partial f}{\partial q} \left(\frac{\partial f}{\partial \alpha} \bigg|_{\alpha_i} \right)^{-1}. \quad (4.14)$$

4.4 Rayleigh Quotient Analysis of the Analytical System

The derivation in the previous chapter has shown that an effective wavenumber-dependent fluid compressibility and wall stiffness explains the existence of a fast P-wave over the entire frequency range, and a much slower compression wave above the first beam resonance. We will further investigate the difference between those two waves in terms of wall deformation and group velocity using Rayleigh's method. This approach also gives insight in the potential energy of both waves. Only the FSI case is studied, the STO case can then be obtained directly by setting $\beta = 0$.

Throughout this analysis, P-waves at three different wavenumbers are compared: A wave with very long wavelength (q_1), a wave with equal group velocity but for a frequency above the first beam resonance (q_3) and the slow P-wave at the same frequency (q_2).

4.4.1 Differential eigenvalue problem

In the FSI case, Eq. (4.12) can be rewritten as a differential eigenvalue problem in a strong form considering the integral term to be a function of q only

$$\frac{EI}{\rho_s A} \frac{d^4 w_i(x, q)}{dx^4} + \frac{\hat{\beta}(q)}{\rho_s AL^2} \int_0^L w_i(x, q) dx = \xi_i w_i(x, q), \quad \text{where } \xi_i = \omega_i^2 \geq 0, \quad (4.15)$$

with the boundary condition Eqs. (4.13). The index i refers to the P-wavemode: $i = 1$ and $i = 3$ for fast P-waves below and above the first beam resonance, and $i = 2$ for the slow P-wave. This equation is written with respect to an undetermined eigenvalue ξ_i and a corresponding eigenfunction $w_i(x, q)$. The weak form can be determined by employing any function $v_i(x, q)$ which satisfies the geometric boundary conditions (Eqs. (4.13a,b)) [?, Chapter 8]. Integration

by parts yields the weak formulation

$$\frac{EI}{\rho_s A} \left(\int_0^L \frac{d^2 v_i(x, q)}{dx^2} \frac{d^2 w_i(x, q)}{dx^2} dx + v_i(x, q) \frac{d^3 w_i(x, q)}{dx^3} \Big|_0^L \right) + \frac{\hat{\beta}(q)}{L^2} \left(\int_0^L v_i(x, q) dx \right) \left(\int_0^L w_i(x, q) dx \right) = \xi_i \int_0^L v_i(x, q) w_i(x, q) dx. \quad (4.16)$$

The Rayleigh quotient determining ξ_i can be found by setting $v_i(x, q) = w_i(x, q)$ in Eq. (4.16), and by applying the natural boundary condition Eq. (4.13c):

$$\begin{aligned} \xi_i &= \frac{EI \int_0^L \left(\frac{d^2 w_i(x, q)}{dx^2} \right)^2 dx + \frac{\hat{\beta}(q)}{L^2} \left(\int_0^L w_i(x, q) dx \right)^2 + 2\hat{k}(q) w_i^2(0, q)}{\rho_s A \int_0^L w_i^2(x, q) dx + 2m_s w_i^2(0, q)} \\ &= \frac{V_i(q)}{K_i(q)} = \left(\omega_i^{(RQ)}(q) \right)^2. \end{aligned} \quad (4.17)$$

The numerator $V_i(q)$ is the maximal potential energy and denominator $K_i(q)$ is the reference kinetic energy of the i^{th} mode [?, Chapter 8]. Plugging $w_i(x, q)$, calculated from the analytical model in the previous section, into Eq. (4.17) leads once again to the dispersion relation shown in Fig. 4.5(a). A minor difference between the curves is dictated by the property of Rayleigh's quotient to be an upper bound for the lowest eigenvalue [?, Chapter 8].

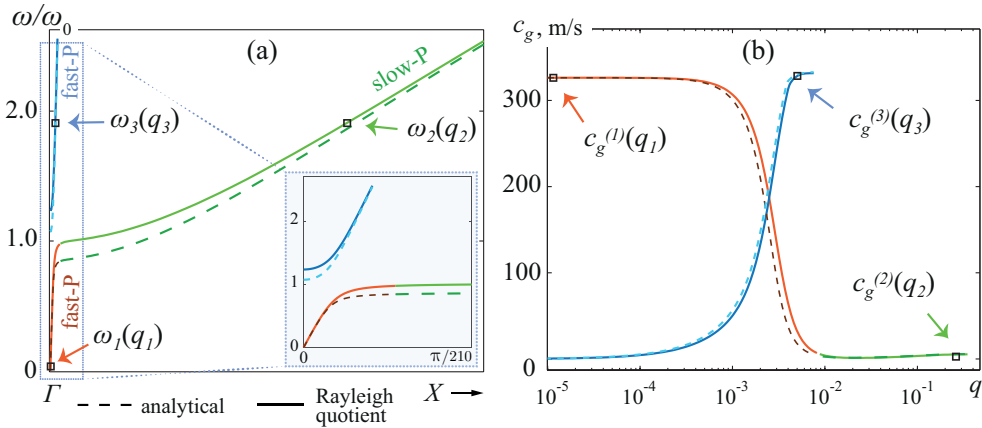


Figure 4.5 – Band-structure (a) and group velocity comparison (b) in the FSI case. Results obtained from the analytical model are given in dashed lines, whereas results based on Rayleigh quotient Eq. (4.17) are in solid lines. The nondimensional wavenumber q is limited by value of 0.5.

4.4.2 Existence of two fast P-waves with same group velocity

From Rayleigh's quotient Eq. (4.17), it is straightforward to calculate the group velocity $c_g^{(i)}(q)$ of the pressure waves. Employing the chain rule yields

$$c_g^{(i)}(q) = \frac{\partial \omega_i(q)}{\partial q} = \frac{\partial}{\partial q} \left(\sqrt{\frac{V_i(q)}{K_i(q)}} \right) = \frac{1}{2} \left(\frac{V_i(q)}{K_i(q)} \right)^{-\frac{1}{2}} \cdot \frac{\partial}{\partial q} \left(\frac{V_i(q)}{K_i(q)} \right). \quad (4.18)$$

If one compares the group velocity derived from Eq. (4.18) to the group velocity directly computed from the analytical dispersion relation in Eq. (4.14), a fair agreement can be observed in Fig. 4.5(b).

At low wavenumbers, the low frequency P-wave is undispersed and thus traveling at a constant group velocity. The high frequency P-wave reaches the same group velocity well above the first beam resonance. Two points fulfilling $c_g^{(1)}(q_1) = c_g^{(3)}(q_3)$ are shown in Fig. 4.5(b). On the same figure, it is clear that a wave pulse with frequency ω_3 will be split into a fast and slow part, the slow part having a considerably higher wavenumber and smaller wavelength.

The intersection of the velocity graphs shows a remarkable point where two waves with different frequencies can travel at the same speed *and* with the same wavelength. This happens at the closest approach of the red and blue dispersion curves in Fig. 4.5(a), thereby minimizing the frequency difference.

4.4.3 Analysis of the existence of a slow and fast P-wave with equal frequency

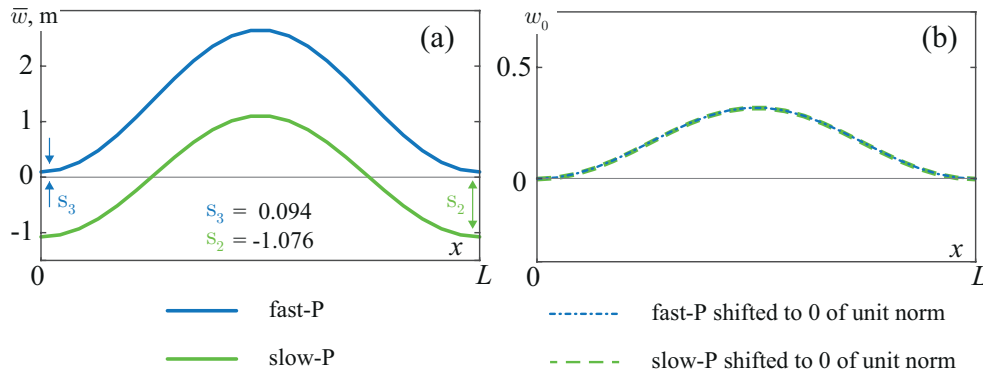


Figure 4.6 – Wavemodes $\bar{w}(x, q)$ derived from analytical model are visualized at q_2 and q_3 corresponding to frequencies $\omega_2(q_2)$ and $\omega_3(q_3)$: analytical solution (a), and $w_0(x, q)$ shifted to zero of unit norm (b).

In this section, the simultaneous presence of two P-waves in the high frequency range is

Chapter 4. Analytical Analysis of Slow and Fast Pressure Waves

analyzed (green and blue lines in Fig. 4.5(a)). As stated before, the wall deformations are only defined up to a constant. They can be rewritten with respect to this constant: $w_i(x, q) = A\bar{w}_i(x, q)$, where A is the undetermined amplitude equal for every i , and \bar{w} is an analytically known function. The slow P-wave deformation $\bar{w}_2(x, q_2)$ and the fast P-wave deformation $\bar{w}_3(x, q_3)$ are shown in Fig. 4.6(a). The normalized bending deformations (denoted as $w_0(x, q)$) at a certain frequency are equal, apart from the translation s_i , as can be verified from Fig. 4.6(b).

The Rayleigh quotient from Eq. (4.17) is now calculated by plugging in the test functions, $w_0(x, q) + s$, in order to investigate the rigid body translation s . The dependency of $\omega_i^{(RQ)}$ on the shift s is shown in Fig. 4.7(a). It should be noted that the wavenumber dependency of $\hat{\beta}$ and \hat{k} results in a completely different qualitative course of the RQ. The zoomed plot of (a) focused on the extrema of $\omega_2^{(RQ)}$ and $\omega_3^{(RQ)}$ is shown in (b). Stars denote the absolute extrema of both functions, where the RQ becomes stationary and is therefore equivalent to solving the eigenvalue problem [?, Chapter 8]. The plot shows the only possibility for the system to exhibit two unique P-waves at the same frequency: the slow P-wave RQ reaches its minimum and the fast P-wave its maximum value. The extrema are reached in the translation values $s = s_2$ for ω_2 , and $s = s_3$ for ω_3 . These values perfectly agree with the values of the tip displacements depicted in Fig. 4.6(a). A similar behavior can be found for all other wavenumbers, as one can verify in Fig. 4.6(c) for a lower frequency.

4.5 Conclusion

The presence of a slow and fast pressure wave in a saturated closed-cell material is an unexpected result occurring in FE simulations of such media. In this chapter, we derived an equivalent unit cell that permits the derivation of the dynamic behavior analytically. Basically, the walls parallel to the wave propagation can be replaced by a wavenumber-dependent mass-spring system. Moreover, the compression modulus of the fluid requires the same wavenumber dependency to cover the fluid-structure interaction. Using these simplifications, the beam equation of the walls perpendicular to the wave propagation can be derived and solved.

The analytical dispersion relation perfectly matches the full FE model, thereby showing that the simplifying assumptions are valid. From the model, one can show that a fast and a slow pressure wave exist for frequencies above the first resonance of a single wall. The wall deformation is equal for both wave modes, but the shift of the wall's endpoints is different. For the fast wave, the endpoints shift in the same direction as the wall deflection, whereas the

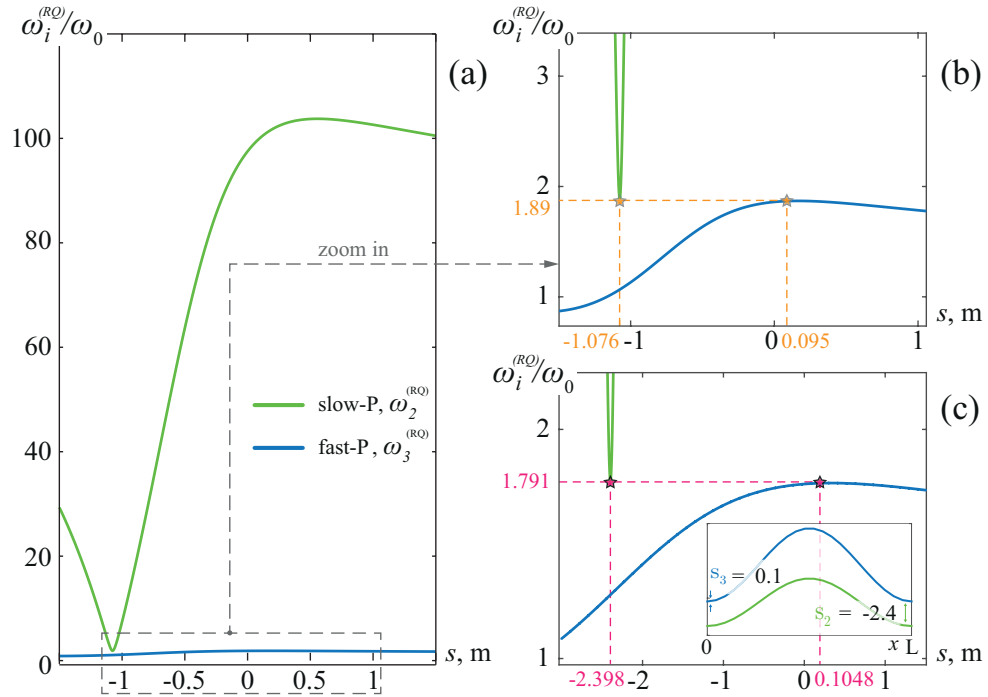


Figure 4.7 – Dependence of Rayleigh quotient on the rigid body shift of the fast and slow pressure wavemodes (a). Coexistence of a slow and fast mode for $q_1 = 1.16 \times 10^{-5}$ (b) and $q_1 = 5.6791 \times 10^{-4}$ (c). The analytically calculated beam deformations are embedded into (c). Stars denote the extrema.

boundaries during the slow p-wave passage move in the opposite direction. In the limit case without fluid, setting the compression modulus β to zero, the slow wave disappears.

These observations are confirmed by Rayleigh's method, which hints to the energetic behavior of the system. Two waves with the same frequency but different wavenumbers can coexist if the RQ of the slow mode reaches a minimum and the RQ of the fast mode shows a maximum.

In order to develop a metamaterial with desired p-wave properties, the analytical description has clear advantages over the full FE simulation. The method is faster than the full FE implementation, since thin walls typically require a large amount of very small elements in the fluid domain. It is also more robust to certain known numerical issues such as shear locking. For thicker walls, the Euler-Bernoulli equation for thin beams could be expanded to more complete dynamic models such as the Timoshenko equation if through-the-thickness shear effects become important.

In the next chapter, we present the experimental approach for shear waves. The numerical and analytical analysis of this kind of waves gathered throughout the thesis is tested experimentally,

Chapter 4. Analytical Analysis of Slow and Fast Pressure Waves

allowing to consider the proposed configuration of a cellular solid with closed cells as an alternative concept of acoustic metamaterials.

5 An Acoustic Metamaterial with Negative Index: Experimental Validation

The chapter is mainly reprinted from [Dorodnitsyn and Van Damme, 2016] with authorization of the publisher.

5.1 Introduction

The previous chapters were devoted to a careful analysis of pressure and shear waves using the numerical and analytical approaches. The analytical models were employed to validate the numerical results, which in turn demonstrated, that saturated porous media can act as acoustic metamaterials and provided guidelines for the design of such systems including their performance in the audible frequency range. Thus it would be important to confirm the studies experimentally.

The chapter is structured as follows. First, an acoustic metamaterial with fluid-filled cells is fabricated. We focus on shear waves in order to investigate the presence of bandgaps for this wave type. According to the simulations, pressure waves are admitted for all frequencies, therefore the bandgaps are called partial [Li et al., 1998]. We measure the shear wavemode deformations, recorded at steady-state, we use a time of arrival analysis to measure the group velocity of selected wavemodes, and finally we identify bandgaps and their frequency ranges. All of our findings are qualitatively and quantitatively in agreement with predictions of the prior theoretical analyses. Eventually, the confirmation with the previous numerical studies is achieved in three steps. In Sec. 5.2 we first measure the wavemodes pertaining to three qualitatively different shear waves in the frequency range below 3.5 kHz, in a steady-state study. We then in Sec. 5.3 measure the group velocity and demonstrate waves with negative group velocity, i.e. moving backwards, for a certain frequency interval, showing that this

system acts as a negative-index metamaterial. Finally, in Sec. 5.4 we confirm the presence of partial bandgaps due to the locally-resonant behavior of the thin structural components.

5.2 Deformation analysis

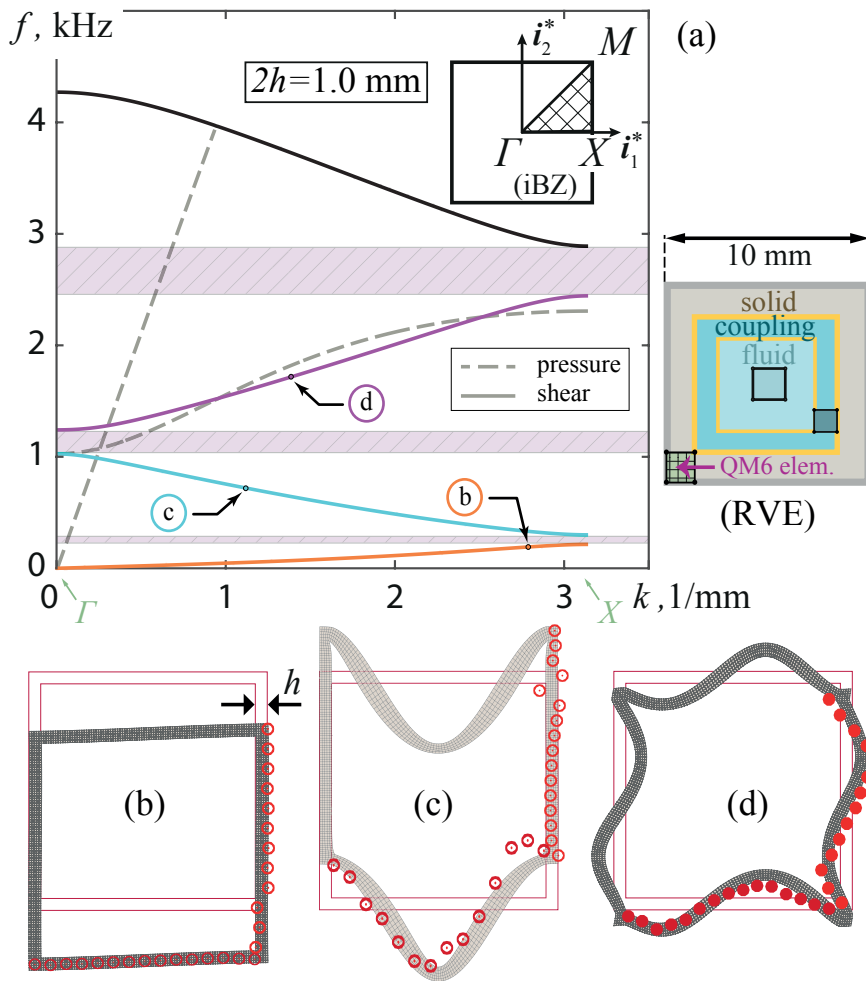


Figure 5.1 – Band-structure (a) for an infinite cellular material with wall thickness of 1 mm along the $\Gamma - X$ path in the iBZ, with discretization of an RVE to the right. Solid phase is DuraformFlex with water as entrained fluid. The bandgap zones are shaded. Deformed configurations of the first 3 shear wave modes (b,c,d). Numerical wavemodes are in gray, while experimental data are superposed with dots (an undeformed configuration is shown with purple frames).

The propagation of elastic waves is studied in a 2D square lattice shown in Fig. 5.1(a). The presence of fluid in a representative volume element (RVE, shown in the right part of Fig. 5.1(a)) is implemented by employing a fluid-structure interaction scheme described in Sec.2.2. Im-

posing periodic boundary conditions along the high symmetry directions in the irreducible Brillouin zone (iBZ) allows for the computation of the band-structure [Kittel, 2004]. The cell walls are discretized with two-dimensional plane QM6 elements, to avoid shear locking [Cook et al., 2007, Chapter 6], and to capture thickness deformations of the solid material (refer to Sec. 3.4.3). The band-structure is limited to the path $\Gamma - X$ in the iBZ (horizontal direction of direct space as shown in Fig. 5.1(a)), and corresponds to the case of water as an entrained fluid, and a wall thickness of 1 mm. Typical cell deformations for the first three shear modes are shown in gray in Fig. 5.1(b,c,d) for wavevector frequency-combinations corresponding to the experiment described below. It can be seen that the low-frequency shear modes (b,c) require much smaller bending of the vertical walls than of the horizontal walls. The first and third modes (b-d) show an antisymmetric deformation of the horizontal walls. For the second shear mode (c), the horizontal walls demonstrate a symmetric mode of a beam with rotation-fixed ends. For each consecutive shear wave band, a higher bending mode is excited. The vertical walls can only undergo antisymmetric deformations (with undeformed walls as a limit state) due to the periodic boundary conditions.

The dispersion curves of even shear bands have a negative slope, a property linked to so-called left-handed materials. In these frequency bands, the material has a negative effective mass density and elastic modulus. As a result, the group and phase velocities have opposite signs. Such effective material parameters can be achieved through an interaction of different resonance types [Liu et al., 2011a]. Although a full analytical treatment for cellular materials is beyond the scope of this letter, we expect that the combination of symmetric and antisymmetric cell wall deformations results in this peculiar dynamic behavior. When both cell walls show antisymmetric modes, a right-handed material with positive effective parameters is obtained.

The design of an experimental cellular solid requires several practical considerations. The structural material properties must be related to the properties of the entrained fluid. To guarantee dispersion via resonant scattering, the resonance frequencies of the lattice walls must be well below those of the cavities (refer to Chapter 3). To operate at acoustic wavelengths, the overall cell dimensions must also be chosen appropriately. Here, we use water for the fluid phase (density $\rho_f = 1000 \text{ kg/m}^3$, bulk modulus $\beta = 2.2 \text{ GPa}$). We therefore chose DuraForm[®]Flex (density $\rho_s = 440 \text{ kg/m}^3$) as the solid phase.

DuraForm[®]Flex is a micro-porous thermoplastic elastomer, i.e. a soft rubber-like material, that is suitable for selective laser sintering (SLS), a high-accuracy 3D printing technique. However, the material properties depend on the entrained fluid because some fluid is absorbed into the pores. Elastic modulus and Poisson's ratio of DuraForm[®]Flex in the water-wet condition were

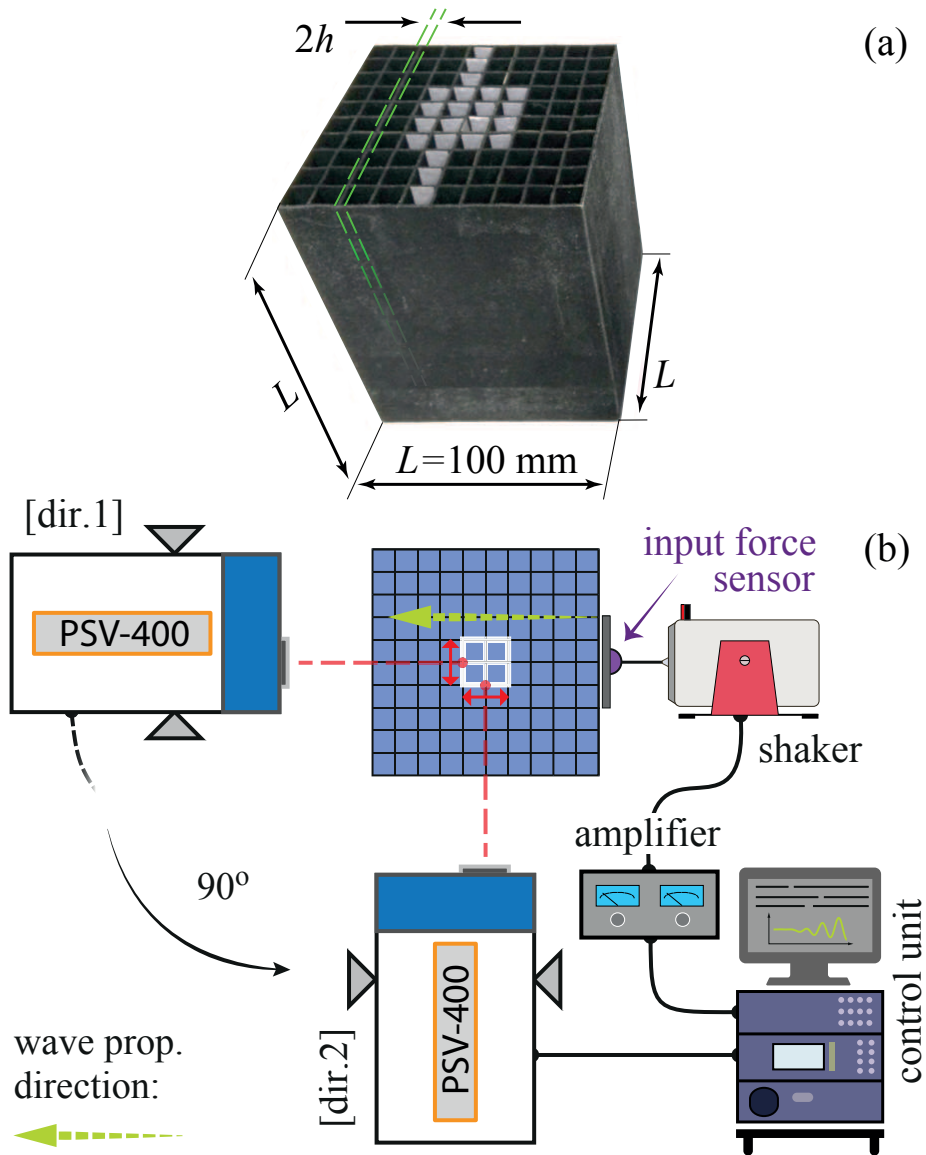


Figure 5.2 – Experimental setup. (a) The geometry of a sample with wall thickness $2h$. (b) Scheme of a setup with the rotatable 2D-SLDV scanning head.

obtained via standard stress-strain tests in accordance with the ASTM D638-14 method [ASTM International, 2014], with deformations measured via Digital Image Correlation (DIC). In the regime of small strains, for axial deformation ϵ_{axial} less than 5%, the material response is nearly linear, which is confirmed in Fig. 5.3(a). Here, the resulting stress σ is represented through the ratio of the applied tensile load F and the cross-sectional area of a sample $A = 0.42 \text{ mm}^2$. The 3D-printed dogbone sample, tensile test machine, and DIC area are shown in the inset to Fig. 5.3(a). Young's modulus and Poisson's ratio can be found from the plateau values of the

smooth fitting of the experimental data. Two sets of processed measurements along with both fitting curves is shown in Fig. 5.3(b,c). The obtained numerical values are as follows, $E_s = 10.38$ MPa and $\nu_s = 0.28$ respectively. The mass density in soaked conditions was measured to be $\rho_s = 595$ kg/m³.

Three cellular structures were fabricated having 10×10 square unit cells in the cross-section, with cell dimensions of $1 \text{ cm} \times 1 \text{ cm}$ and wall thicknesses $2h$ of 1 mm, 1.5 mm and 2 mm, and a height of 10 cm, as shown in Fig. 5.2(a). This configuration is sufficient to approximate periodic boundary conditions and plane-strain conditions. The cells in the sample are filled with water to within several millimeters of the top of the sample, which remains open and unconstrained. The bottom of the sample is fixed to avoid undesired rigid body shifts.

The experimental setup is shown schematically in Fig. 5.2(b). In order to measure wall deformations, we employed a Scanning Laser Doppler Vibrometer (SLDV) (Polytec[®] PSV-400, operated with the Polytec[®] PSV-A-010 workstation). The SLDV allows for the reconstruction of the out-of-plane motion of a preselected 2D grid of points. To measure the motion of the walls both perpendicular and parallel to the direction of wave propagation, the SLDV was located in two positions as shown in Fig. 5.2(b) ([dir.1] and [dir.2], respectively). Scanning was performed on a 2×2 set of cells in the middle of the sample, ensuring retention of periodic boundary conditions. The scanned area was coated with reflective tape (Fig. 5.2(a)) to increase the quality of the laser beam reflection. The plane acoustic waves were generated with a LDS V201 shaker. A force sensor was located at the junction of the stinger and percussive plate.

For the deformation analysis, we excite the 1 mm wall sample using a continuous excitation at frequencies corresponding to different expected shear wavemodes (200 Hz, 700 Hz, and 1700 Hz) until the measured velocity reaches a constant level (steady-state regime). To remove noise, the SLDV measurements were averaged 20 times. The resulting velocity signals give an image of the wall deformation in time. Examining a single timeframe, we obtain a very good match between experiment and theory, as shown in Fig. 5.1(b-d)). Note that, due to the normal excitation, pressure waves are also predicted numerically. We expect the current sample design with slender soft walls to be very compliant for shear waves, compared to the stiffness in the longitudinal direction. Indeed, none of the experimental results shows any trace of pressure waves.

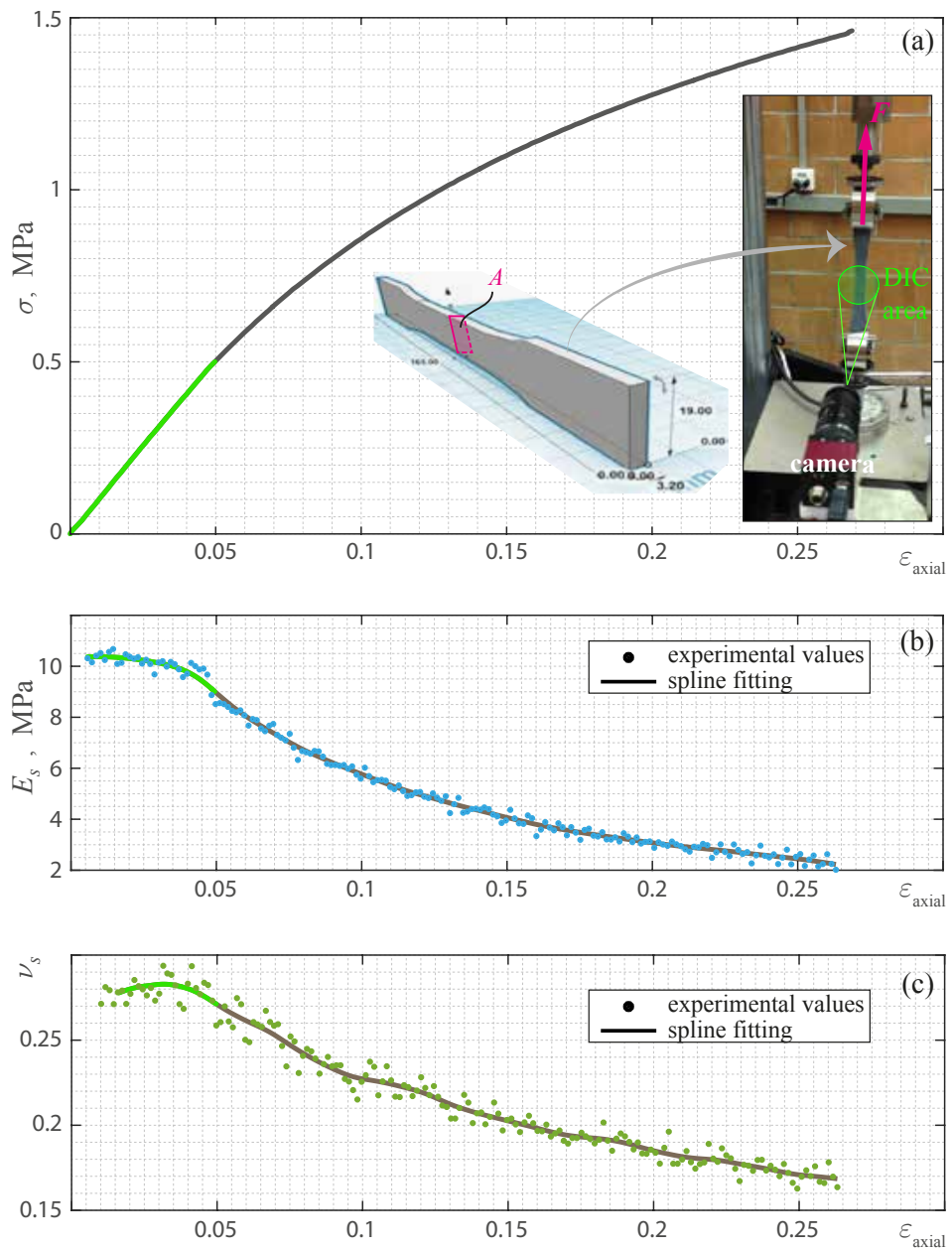


Figure 5.3 – A tensile test of a dogbone made of DuraformFlex taken in moist condition. The stress-strain curve with the tensile test setup (a). Young's modulus and Poisson's ratio as a function of axial strain (b), (c) respectively. The linear regime for axial strains ϵ_{axial} less than 5% is highlighted in green.

5.3 Group velocity analysis. Negative index behavior

Using the same cellular structures, we measured the group velocity based on a time of arrival (TOA) analysis. The motion of a wall, away from the boundaries, is measured at a single point of the selected wall using the SLDV in the [dir.1] alignment. For this analysis, the forcing signal consists of a 4-cycle sinusoidal pulse modulated with a Hamming window in a frequency range of 300-2700 Hz with 50 Hz steps. The waves are generated by the same shaker connected to a waveform generator (National Instruments PXI 5402) controlled by LabView.

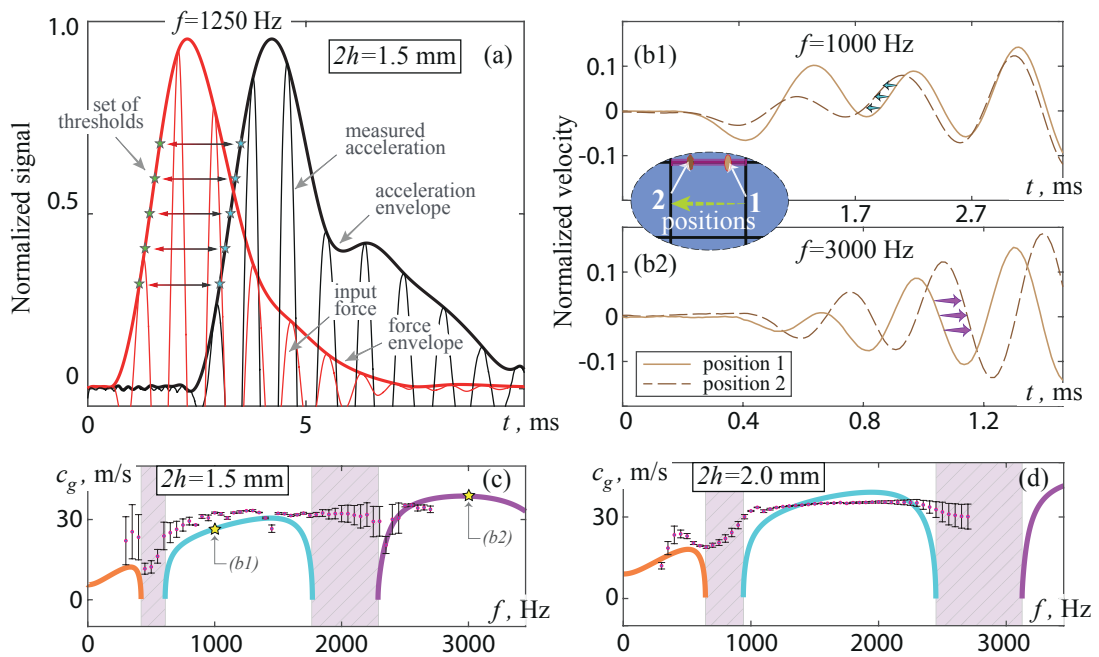


Figure 5.4 – Group velocity analysis. (a) Thresholds for a TOA measurement for $2h = 1.5$ mm and $f = 1250$ Hz. The wave propagation direction for $2h = 1.5$ mm: (b1) at $f = 1000$ Hz (backward, $c_g < 0$), and (b2) at $f = 3000$ Hz (forward, $c_g > 0$). The comparison of experimental (mean values in dots with corresponding errorbars) and numerical (solid colored lines) group velocities for $2h = 1.0$ mm (c) and $2h = 1.5$ mm (d).

The TOA is measured at the selected wall with respect to the initial force signal recorded by the input force sensor. In order to compare both signals, the recorded wall velocities are smoothed using Savitzky-Golay filtering and then differentiated to obtain the acceleration. Both measured signals, force and acceleration, are wrapped with the envelope. Then, the signals are normalized by the amplitude of the envelope's first peak. Additional peaks might occur in the vibrometer signal due to reflections. Finally, a threshold value is selected at which the time difference is calculated. We chose a mid-range value of 0.5. In order to estimate the error in this measurement, several threshold values were chosen as shown in Fig. 5.4(a) for

$2h = 1.5$ mm at $f = 1250$ Hz. Knowing the TOA and the distance between the input force sensor and the selected cell wall, the group velocity c_g can be determined. The set of thresholds defines the error bars as the standard deviation of the mean value at each excitation frequency. The results for $2h = 1.5$ mm and $2h = 2.0$ mm are shown in Figs. 5.4(c,d), respectively. The numerical estimation of the group velocity is gathered from the dispersion curves along $[\Gamma - X]$ using the relation $c_g = 2\pi(\partial f / \partial k)$.

Good agreement between experimental and numerical group velocities is achieved for $2h = 1.5$ mm and $2h = 2.0$ mm (Fig. 5.4(c,d)). The measured velocities show a clear dip for frequencies in the first bandgap. In the second bandgap, the error bars become considerably larger. This is due to the fact that the resulting pulse contains frequencies from both pass bands around the bandgap, which are traveling at different velocities.

One can verify the presence of a left-handed behavior qualitatively based on phase considerations. To do this, we point the laser vibrometer in the [dir.2] direction. Two sensing positions on a single cell wall are shown in the inset of Fig. 5.4(b1,b2). Position 1 is closer to the shaker while position 2 is located within the same cell but further from the source. The recorded signals for both positions are shown in Fig. 5.4(b1, b2) ($2h = 1.5$ mm at $f = 1000$ Hz and $f = 3000$ Hz). At the lower frequency, group and phase velocities are expected to have opposite signs. The phase front measured closest to the source arrives *later* than the phase front at the more-distant point. Although the wave package travels forward in time, the phase seems to go in the opposite direction, meaning that c_p and c_g have a different sign. At the higher frequency, a positive group and phase velocities are obtained: the direction of motion of the phase is equal to the one of the wave package. The phenomenon of group and phase velocity having opposite different signs is due to a negative refractive index, as has been reported for several other types of acoustic metamaterial configurations [Brunet et al., 2015, Fok and Zhang, 2011].

5.4 Partial bandgaps analysis

Finally, we confirm experimentally the presence of the bandgaps predicted by the FE model. As discussed earlier, these cellular structures are of the local resonant scattering type. Bandgaps occur in the vicinity of the resonant frequencies of the beam-walls, where destructive interference forbids the propagation of shear waves for any wavenumber; pressure waves do propagate, however. The numerically predicted bandgaps are indicated by the shaded areas in Fig. 5.4(c,d). The bandgaps here are narrow compared to other metamaterials [Delpero et al., 2016, Krödel et al., 2014]. To uncover bandgaps experimentally, we study the response of

the structure to both a 3-period burst and a sweep over the frequency range of interest. The sweep signal is used to verify the bandgap zones whereas the burst measurements clarify the signal deformation due to the dispersion. As an illustrative example, the case $2h = 1.5$ mm at $f = 550$ Hz is shown in Fig. 5.5(a). The force and wall response used in the TOA experiment are processed via Fast Fourier Transforms (FFTs) in Matlab to determine the single-sided spectrum. The spectra are plotted on top of each other, and a clear bandgap in the vicinity of the selected frequency is observed (Fig. 5.5(a)). Since the gap is narrow, the remaining frequency content of the pulse can travel through the structure.

The sweep response over an interval of 200-4000 Hz is measured via SLDV on 4 adjacent walls perpendicular to the wave propagation, and located six cells away from the source, using the SLDV in the [dir.1] orientation. In 20 evenly spaced points, the sweep transfer function $H(f)$ is calculated as the ratio of the measured velocity spectrum and the input force spectrum. The transfer functions for both samples are shown in Fig. 5.5(b,c) along with the numerically estimated bandgaps. Good agreement between numerical and experimental results is observed. Although the bandgaps are narrow and only valid for shear waves, a clear dip in the transfer functions is present. The second band gap is measured at slightly lower frequencies for $2h = 2.0$ mm. This can be explained since no damping is applied in the model, although viscoelastic damping becomes more important for thicker cell walls at high frequencies.

The sweep response over an interval of 200-4000 Hz is measured via SLDV on 4 adjacent walls perpendicular to the wave propagation, and located six cells away from the source. In 20 evenly spaced points, the sweep transfer function $H(f)$ is calculated as the ratio of the measured velocity spectrum and the input force spectrum. The transfer functions for both samples are shown in Fig. 5.5(b,c) along with the numerically estimated bandgaps. Very good agreement between numerical and experimental results is observed. Although the bandgaps are narrow and only valid for shear waves, a clear dip in the transfer functions is present. A shift of numerical areas towards slightly larger frequencies for $2h = 1.0$ mm can be explained by inaccuracies in the material parameters and omission of damping in the model. Moreover, 1 mm is the minimal thickness for a structure laser-sintered using Duraform, thus making a sample less precise than the larger one.

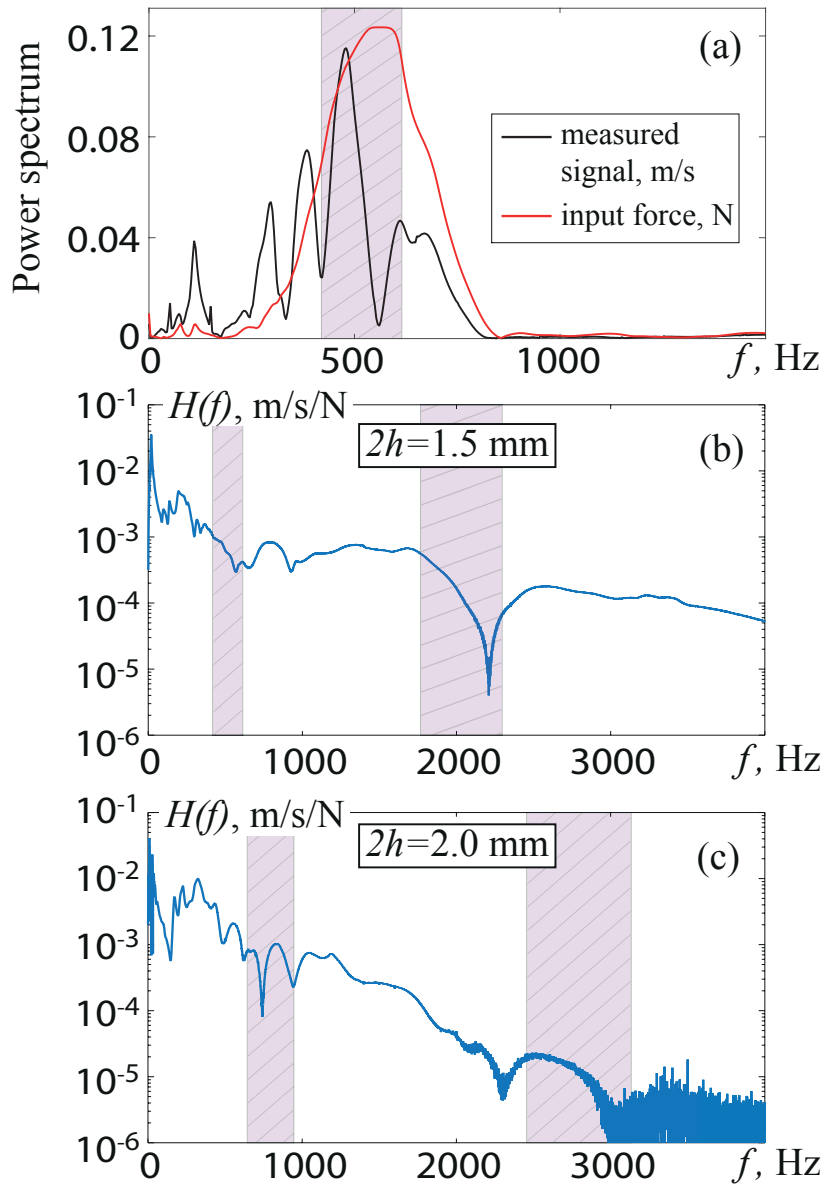


Figure 5.5 – Bandgap analysis. (a) Spectrum of a single frequency burst for $2h = 1.5$ mm at $f = 550$ Hz. (b,c) Transfer function of a sweep signal for $2h = 1.0$ mm and $2h = 1.5$ mm, respectively. The numerical bandgap zones are superposed on top.

5.5 Conclusion

In summary, we have presented an experimental study of shear wave propagation in an acoustic metamaterial with entrained fluid, and confirmed predictions of a previous numerical model. Comparisons were made for the steady-state modes of the shear waves, for the group velocity –in particular regimes of left-handed behavior– and for bandgaps in the band-

structure. For different wall thicknesses, very good agreement with numerical estimates was found for all three of the above features. Therefore, we believe that this work establishes a new concept for acoustic metamaterials: a closed-cell cellular solid with entrained fluid. Such a metamaterial should find wide application due to its low cost, simplicity, versatility in terms of scalability, and ability to design desired macroscopic behavior using different types of fluids and bulk materials.

6 Conclusions

6.1 Summary of the results

This thesis introduces a novel concept for metamaterials inspired by peculiar properties of periodic cellular solids. Although metamaterials are designed materials branched off from the electromagnetic metamaterials, we suggest considering a closed-cell cellular solid with entrained fluid and soft vibrating walls instead. Cellular solids have well-settled theoretical models which so far were not linked to the acoustic metamaterials field.

A numerical model for the dynamics of the considered metamaterial was proposed first in Chapter 2. A representative volume element was analyzed with the finite-element approach with an explicitly implemented fluid-structure interaction scheme. Considering both beam and plane elements allows for analyzing the propagation of elastic plane harmonic wave in a wide range of relative densities $1 \times 10^{-4} \leq \rho^* \leq 1$, for both light and heavy fluid phases. The analysis of such a range permits to explore the applicability of Biot's theory, originally developed for porous media with open cells. This theory predicts two pressure modes, a fast and a slow one. However, under the closed-cell limit, it only foresees the fast pressure wave. The numerical model indeed shows a single pressure wave only for frequencies below the resonance of the lattice walls. Surprisingly, two pressure modes are present for higher frequencies. In the case of a low-frequency shear wave, it was shown that the fluid merely acts as an added mass. Thus the homogenized model based on microstructural deformations for drained configurations can be employed. The latter has a simpler mathematical description and meaningful physical basis, and shows a good agreement with both the numerical and Biot formulations.

Wave propagation in the studied acoustic metamaterial is characterized by strong scattering,

Chapter 6. Conclusions

unlike porous media. In the latter case, dispersion only arises when the wavelengths match a characteristic size of the pores. In Chapter 3 the dispersion sources were analyzed. In the proposed cellular solid, the structure phase occupies a small portion of the total volume and thus may resonate at a relatively low frequency, which affects the wave dispersion. Furthermore, the contribution of entrained fluid was analyzed using the analogy between a cavity and an equivalent tube. A tube-piston model based on computed microstructural deformations showed an accurate description of the dynamic behavior away from resonances. The effective tube and cavity models allowed the derivation of the effective stiffness tensor at the macroscale in terms of the geometric and material properties. As an important conclusion, the pressure waves were shown to be isotropic, while the shear wavemode was found anisotropic for all considered values of relative density and regardless of whether the fluid is heavy or light. Furthermore, for heavy entrained fluids, through-the-thickness wall deformations were observed. This is opposed to light entrained fluids, where the deformations are of the hybrid bending type only. Thus, when designing a metamaterial of this class it would be of significant importance to take into account this phenomenon in order to benefit from the locally resonant behavior.

Three distinct pressure waves can be identified in the frequency regime around the first resonant frequency of the lattice walls. The slow pressure wave is shown to be one order of magnitude slower than both fast ones. The latter propagate at the same speed in the non-dispersive regimes away from the resonance. The slow pressure wave only occurs in case the cells are filled with a fluid and it propagates only for frequencies above the first structural resonant frequency. This exotic wave is not predicted by classical models of porous media. In Chapter 4 an analytical description of pressure waves in this frequency range is derived. As a preliminary step, a simplified finite-element model was used to integrate the fluid effect into the structure dynamics. The resulting equivalent continuum does not need to account for the fluid-structure interaction, yet the wave propagation showed a good agreement with the original finite-element model governed by fluid-structure interaction. It was shown that the bending deformation of the beams was the same for slow and fast longitudinal waves at a given frequency, and that they only differ as regards the rigid body translation. The coexistence condition for both waves was finally verified with Rayleigh's variational approach. Altogether the physics behind the propagation of pressure waves was derived from a bottom-up approach, rather than from an ad hoc model as in Biot's theory.

Finally, in Chapter 5 the proposed acoustic metamaterial was realized experimentally. The shear wave propagation in a soft rubber-like cellular solid with water-filled cells was investi-

gated. The results were compared to three numerical predictions: the steady-state analysis of the wavemode shapes, the group velocity and in particular regimes of negative group velocity, and the presence of narrow partial bandgaps in the band-structure. A very good agreement with numerical estimations was found for all these features.

6.2 Further outlook and possible applications

2D geometries

Since the entire project was based on a 2D square lattice it would be essential to consider other planar configurations. It is known that the change in unit cell geometry of a cellular solid with no entrained fluid results in a significant alteration of the wave dynamics, which in turn may introduce or affect the bandgaps and frequency-dependent anisotropy [Phani et al., 2006]. The introduction of a fluid phase in e.g. a honeycomb structure is worth studying, due to its abundant presence in many applications. The computational model requires a relatively minor modification for different 2D geometries determined by an appropriate mapping of the boundary conditions without any mathematical change in the system of governing equations.

3D extension

Once the 2D system is fully documented, the analysis of the 3D case needs to be studied. Although the conceptual idea remains the same, the computational part needs to be updated significantly. For instance, in order to describe a closed-cell configuration in 3D, the beam elements no longer hold, and the use of special shell elements is necessary. As a takeoff, a 3D extension for a particular geometry has been already done [Spadoni et al., 2014]. The discretization of a unit cell uses rigidly connected shells of uniform thickness with both membrane and bending stiffness forming the solid phase. The composed material with entrained fluid can be considered as a closed-cell crystalline foam. This is a prototypical 3D acoustic metamaterial characterized by strong wave dispersion due to resonant scattering. The theoretical proposition becomes even more significant taking into account recent achievements in manufacturing techniques of periodic crystalline closed-cell foams [Gabbriellini et al., 2012]. The studied configuration shows remarkable resemblance to pentamode behavior within distinct frequency bands, resulting from the interaction of fluid and structure. Essentially, if this study is practically realized it will represent a much simpler realization of the pentamode material derived in [Kadic et al., 2012] (Sec. 1.2.2, Fig. 1.3(c)).

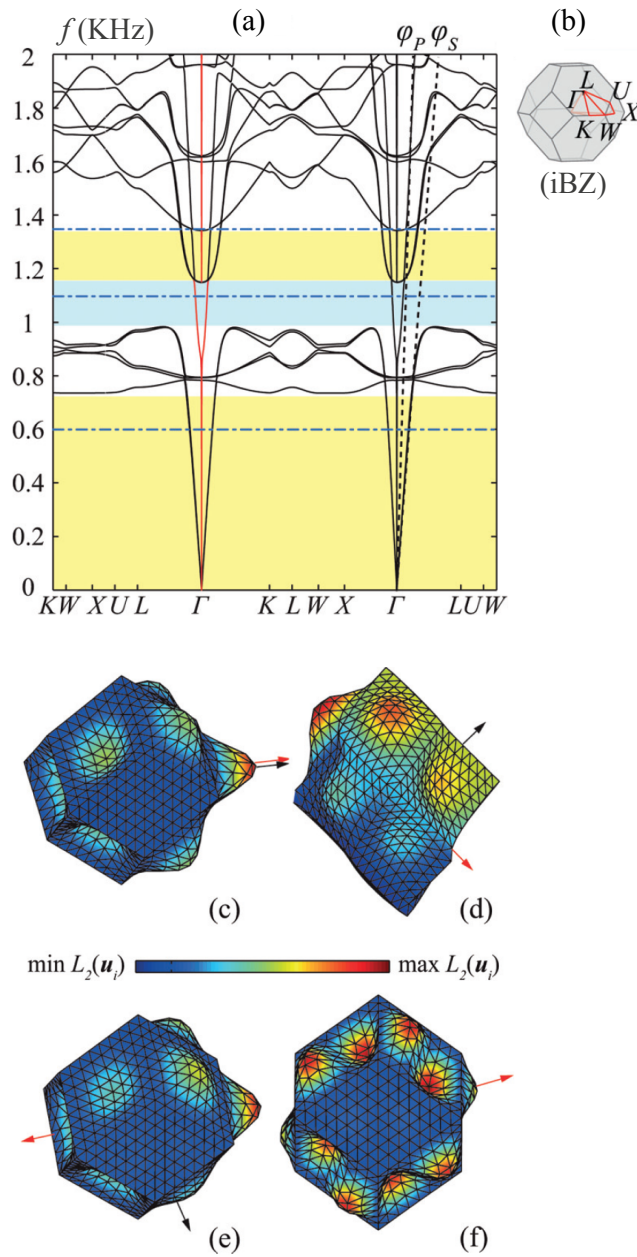


Figure 6.1 – Band-structure for the fcc rhombic dodecahedron foam with entrained water in (a) and the corresponding iBZ (b). Several simple deformed configurations are as follows: (c) decapolar fast pressure ($f = 221.6$ Hz, $k_1 = k_2 = 24.6$, $k_3 = 0$ rad/m), (d) dipolar shear ($f = 434.5$ Hz, $k_1 = k_2 = 5122$, $k_3 = 0$ rad/m), (e) decapolar ballistic shear ($f = 1233.3$ Hz, $k_1 = k_2 = 9220$, $k_3 = 0$ rad/m), and (f) resonant hexadecapolar shear mode ($f = 1630.9$ Hz, $k_1 = k_2 = 15366$, $k_3 = 0$ rad/m) with the red and black arrows indicating the wavevector and the polarization respectively. Figure is reprinted from [Spadoni et al., 2014] with publisher permission.

Three unit cells, typical for foams, were considered: the truncated octahedron (Kelvin foam), the rhombic dodecahedron, and the Weaire-Phelan unit cell. The computed band-structure for the rhombic dodecahedron is given in Fig. 6.1(a). The wide shear waves bandgap is shaded in light blue. It is also notable that the velocity derived with the equivalent piston-tube model described in details in Chapter 3 matches the numerical results (φ_P in the right part of Fig. 6.1(a)). The velocity of the low frequency shear wave predicted with the equivalent continuum described in Chapter 2 is also in good agreement with the numerical estimations (φ_S in the right part of Fig. 6.1(a)). Several representative deformed configurations are shown in Fig. 6.1(c) for a pressure wave, and in Fig. 6.1(d-f) for shear waves.

Experimental validation of pressure waves

Finally, the experiment described in Chapter 5 was carried out to investigate shear waves. A logical follow-up is to prove experimentally the presence of both, fast and slow longitudinal modes, predicted by the numerical model. Although the computational formulation has been validated using several bottom-up models, the measurement of two pressure waves propagating simultaneously within the common frequency range would be a great achievement. The conducted experiment only allowed measurable shear waves due to the material and fabrication limitations. Thus, a possible analysis of pressure waves could imply the prevention of shear behavior, or at least characterized by an undispersed shear wavemode.

One of the possible configurations for a unit cell with reduced shear compliance, is using two materials for the solid matrix. Preserving the same square geometry, the RVE is now updated as follows: vertical walls are made of a soft thermo-plastic elastomer (such as Duraform), and horizontal walls are made of a stiff material (such as a steel, for instance). This design is promising due to the prior knowledge of the pressure wavemodes to pertain the particle motion in the horizontal direction. The soft component of these unit cells can still be manufactured with the laser sintering technique, where the steel parts can then be inserted into predesigned grooves. The band-structure for such a system can be calculated using the existing FEM model, and is provided in Fig. 6.2(a). Here, the geometry of an RVE is defined according to Fig. 6.2(b) with the following mechanical properties for steel: $\rho_{\text{steel}} = 8027.2 \text{ kg/m}^3$, $\nu_{\text{steel}} = 0.33$, $E_{\text{steel}} = 193 \text{ GPa}$. The derived band-structure confirms the presence of the single shear wavemode (Fig. 6.2(c)). Therefore, slow and fast, pressure waves co-exist in certain frequency ranges highlighted in gray in Fig. 6.2(a). Despite the different matrix, the desired resonance-based dispersion is present. The deformed configurations are labeled in the dispersion curves accordingly to the mode type: at $f = 860 \text{ Hz}$ the slow and fast longitudinal wavemodes (d,e), and at $f = 2350 \text{ Hz}$

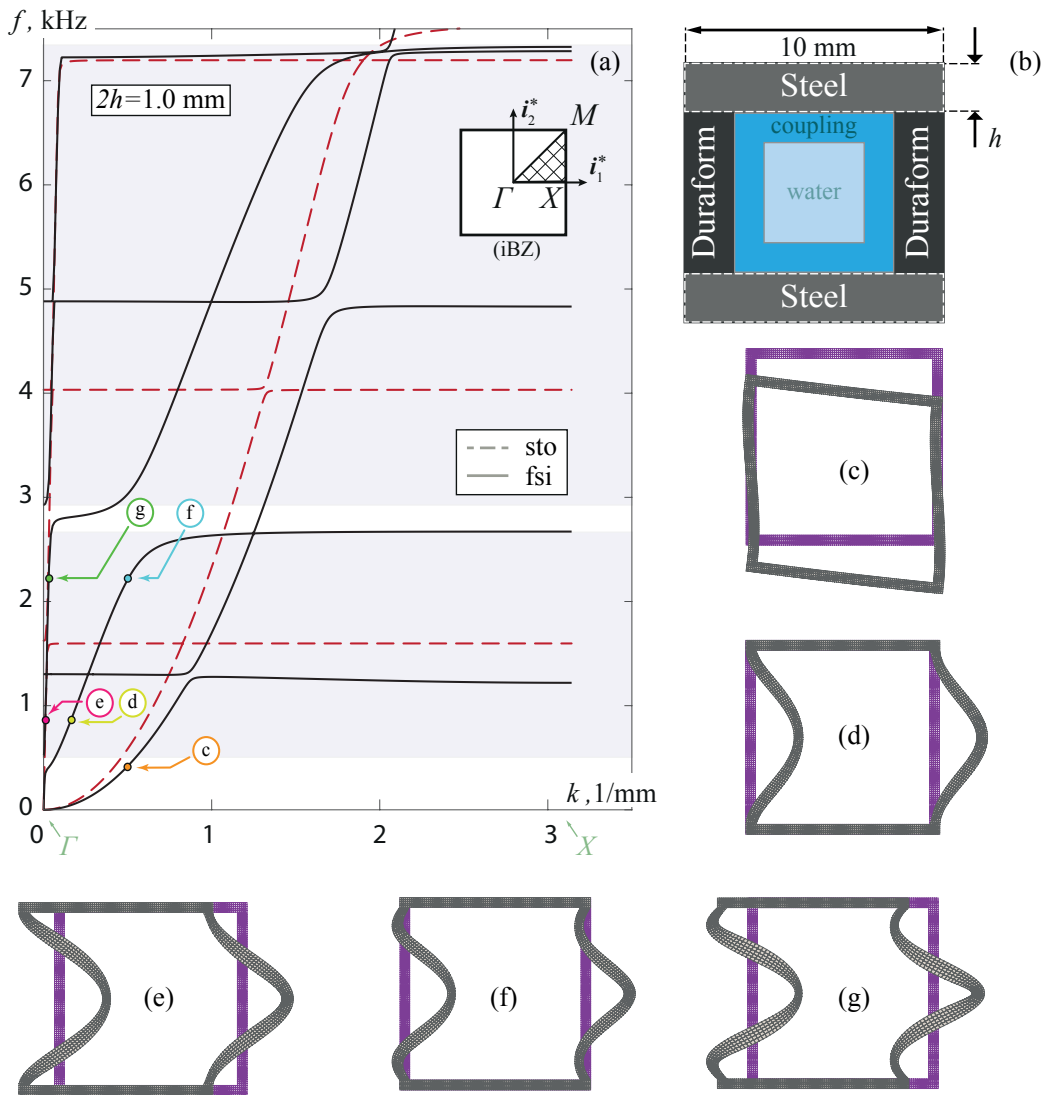


Figure 6.2 – Band-structure (a) for an infinite cellular material with wall thickness of 1 mm along the $\Gamma - X$ path in the iBZ. The solid phase consists of two bulk materials, Duraform and steel; the discretization of the corresponding RVE (b). Deformed configuration of the first shear wave mode at $f = 425$ Hz (c); slow (d) and fast (e) pressure wavemodes at $f = 860$ Hz; slow (f) and fast (g) pressure wavemodes at $f = 2350$ Hz. The undeformed configurations are shown with purple frames.

the slow and fast ones (f,g), as expected, are characterized by horizontal displacement and by bending-type deformation.

Possible applications

It was shown throughout the thesis that the studied concept provides the possibility to tune the velocity of the waves, a key parameters for acoustic metamaterials. The frequency range and resulting velocities are controlled by the actual cell size, wall thickness, bulk material properties and the type of the entrained fluid. This concept should eventually find a wide application, representing a versatile acoustic metamaterial platform characterized by low cost, and a simple, scalable design. Therefore cellular solids with controlled macroscopic parameters (bulk material and entrained fluid) might allow acoustic lensing and waveguiding, as introduced in Chapter 1.

The resonant scattering in cellular fluid-filled structures may introduce a strong dispersion source. The latter was analyzed in detail in the present work. Controlling the dispersion leads to possible applications of frequency filtering due to partial or full bandgaps. The ability to design a bandgap is interesting not only as a curious scientific problem but also as a highly demanded feature in industrial applications of sound and vibration insulation of structures [Goffaux et al., 2003, Zhu and Semperlotti, 2013], acoustic mirrors in selective frequency ranges [Aliev et al., 2010, Ella, 1999], and even seismic absorbers [Brûlé et al., 2014, Kim and Das, 2012].

A Appendix

A.1 Derivation of the analytical dispersion relation

In this appendix, mathematical procedure is provided to solve Eq. (4.12) using the four boundary conditions stated in Eqs. (4.13a-c). The approach is structured in the following consecutive order:

- Differentiate Eq. (4.12), keeping in mind that P_b is a definite integral with finite limits of integration, and therefore independent of x :

$$w''''(x) - \alpha^4 w'(x) = 0. \quad (\text{A.1})$$

- Eq. (A.1) is a homogeneous fifth-order ODE, whose general solution contains five constant coefficients C_i , for $i = 1, 2, \dots, 5$. Solving it with respect to $w'(x)$ yields:

$$w'(x) = C_1 \sin(\alpha x) + C_2 \cos(\alpha x) + C_3 \sinh(\alpha x) + C_4 \cosh(\alpha x). \quad (\text{A.2})$$

- Integrating once Eq. (A.2) reads:

$$w(x) = \frac{1}{\alpha} [-C_1 \cos(\alpha x) + C_2 \sin(\alpha x) + C_3 \sinh(\alpha x) + C_4 \cosh(\alpha x)] + C_5. \quad (\text{A.3})$$

- Notice, that taking four times derivative of Eq. (A.3) allows distinguishing C_5 as:

$$w''''(x) = \alpha^4 (w(x) - C_5). \quad (\text{A.4})$$

- Plugging Eq. (A.3) into Eq. (A.1) and using Eq. (A.4) allows defining C_5 in terms of the

other four constants:

$$C_5 = \frac{\tilde{\beta}}{\alpha^2 (\alpha^4 - \tilde{\beta}L)} \left[-C_1 \sin(\alpha L) + C_2 (\cos(\alpha L) - 1) + C_3 \sinh(\alpha L) + C_4 (\cosh(\alpha L) - 1) \right], \quad (\text{A.5})$$

where:

$$\tilde{\beta} = \frac{\hat{\beta}(q)}{EIL^2}. \quad (\text{A.6})$$

- Thus, the general solution to Eq. (4.12) is:

$$w(x) = C_1 \left[-\frac{1}{\alpha} \cos(\alpha x) - \Lambda \sin(\alpha L) \right] + C_2 \left[\frac{1}{\alpha} \sin(\alpha x) - \Lambda (\cos(\alpha L) - 1) \right] + C_3 \left[\frac{1}{\alpha} \cosh(\alpha x) + \Lambda \sinh(\alpha L) \right] + C_4 \left[\frac{1}{\alpha} \sinh(\alpha x) + \Lambda (\cosh(\alpha L) - 1) \right] \quad (\text{A.7})$$

- The unknown coefficients in Eq. (A.7) can be found using the four boundary conditions Eqs. (4.13a-c). The resulting homogeneous system of linear equations has a nontrivial solution only if the determinant of the coefficient matrix is zero. This condition provides the characteristic equation with respect to the nondimensional wavelengths $\alpha_i L$ as a function of q . We do not show the characteristic equation for brevity, however it represents an elaborate trigonometric equation. The solution relates the frequency ω_i to a wavenumber q , employing the equality:

$$\omega_i(q) = \alpha_i^2(q) \sqrt{\frac{EI}{\rho_s A}}. \quad (\text{A.8})$$

This allows the calculation of the dispersion relation which is plotted in Fig. 4.4.

Bibliography

- J. Achenbach. *Wave propagation in elastic solids*, volume 16. Elsevier, 2012.
- K. Alderson and K. Evans. The fabrication of microporous polyethylene having a negative poisson's ratio. *Polymer*, 33(20):4435–4438, 1992.
- G. N. Aliev, B. Goller, D. Kovalev, and P. A. Snow. Hypersonic acoustic mirrors and microcavities in porous silicon. *Applied Physics Letters*, 96(12):124101, 2010.
- J. Allard and N. Atalla. *Propagation of Sound in Porous Media: Modelling Sound Absorbing Materials 2e*. Wiley, 2009.
- M. J. Allen, V. C. Tung, and R. B. Kaner. Honeycomb carbon: a review of graphene. *Chemical reviews*, 110(1):132–145, 2009.
- X. Ao and C. Chan. Far-field image magnification for acoustic waves using anisotropic acoustic metamaterials. *Physical Review E*, 77(2):025601, 2008.
- ASTM International. D638-14 standard test method for tensile properties of plastics. 2014. URL <http://www.astm.org/Standards/D638.htm>.
- B. A. Auld. *Acoustic fields and waves in solids*, volume 1. Wiley New York, 1973.
- J. L. Auriault and E. Sanchez-Palencia. Etude du comportement macroscopique d'un milieu poreux saturé déformable. *Journal de Mécanique*, 16(4):575–603, 1977.
- Y. Bachmat and J. Bear. On the concept and size of a representative elementary volume (rev). In *Advances in transport phenomena in porous media*, pages 3–20. Springer, 1987.
- B. Banerjee. *An introduction to metamaterials and waves in composites*. CRC Press, 2011.
- J. Bauer, S. Hengsbach, I. Tesari, R. Schwaiger, and O. Kraft. High-strength cellular ceramic composites with 3d microarchitecture. *Proceedings of the National Academy of Sciences*, 111(7):2453–2458, 2014.

Bibliography

- Z. P. Bažant and M. Christensen. Analogy between micropolar continuum and grid frameworks under initial stress. *International Journal of Solids and Structures*, 8(3):327–346, 1972.
- T. Belytschko. Fluid-structure interaction. *Computers & Structures*, 12(4):459–469, 1980.
- J. G. Berryman. Confirmation of biot’s theory. *Applied Physics Letters*, 37(4):382–384, 1980.
- M. A. Biot. Theory of propagation of elastic waves in a fluid-saturated porous solid. I. Low-frequency range. *The Journal of the Acoustical Society of America*, 28:168, 1956a.
- M. A. Biot. Theory of propagation of elastic waves in a fluid-saturated porous solid. II. Higher frequency range. *The Journal of the Acoustical Society of America*, 28:179, 1956b.
- M. A. Biot and D. G. Willis. The elastic coefficients of the theory of consolidation. *J. appl. Mech*, 24(4):594–601, 1957.
- W. Bragg and W. Bragg. The reflection of x-rays by crystals. *Proceedings of the Royal Society of London. Series A, Containing Papers of a Mathematical and Physical Character*, pages 428–438, 1913.
- L. Brillouin. *Wave Propagation in Periodic Structures: Electric Filters and Crystal Lattices*. Dover Phoenix Editions. Dover Publications, 2003. ISBN 9780486495569.
- S. Brûlé, E. Javelaud, S. Enoch, and S. Guenneau. Experiments on seismic metamaterials: Molding surface waves. *Physical review letters*, 112(13):133901, 2014.
- T. Brunet, A. Merlin, B. Mascaro, K. Zimny, J. Leng, O. Poncelet, C. Aristégui, and O. Mondain-Monval. Soft 3d acoustic metamaterial with negative index. *Nature materials*, 14(4):384–388, 2015.
- W. Brutsaert. The propagation of elastic waves in unconsolidated unsaturated granular mediums. *Journal of Geophysical Research*, 69(2):243–257, 1964.
- T. Bückmann, N. Stenger, M. Kadic, J. Kaschke, A. Frölich, T. Kennerknecht, C. Eberl, M. Thiel, and M. Wegener. Tailored 3D Mechanical Metamaterials Made by Dip-in Direct-Laser-Writing Optical Lithography. *Advanced Materials*, 2012.
- R. Burridge and J. B. Keller. Poroelasticity equations derived from microstructure. *The Journal of the Acoustical Society of America*, 70:1140, 1981.
- J. Carcione. *Wave Fields in Real Media: Wave Propagation in Anisotropic, Anelastic, Porous and Electromagnetic Media*. Handbook of Geophysical Exploration: Seismic Exploration. Elsevier Science, 2007. ISBN 9780080468907.

- J. M. Carcione and G. Quiroga-Goode. Some aspects of the physics and numerical modeling of biot compressional waves. *Journal of Computational Acoustics*, 3(04):261–280, 1995.
- J. M. Carcione, F. Cavallini, J. E. Santos, C. L. Ravazzoli, and P. M. Gauzellino. Wave propagation in partially saturated porous media: simulation of a second slow wave. *Wave Motion*, 39(3): 227–240, 2004.
- E. Casadei and J. J. Rimoli. Anisotropy-induced broadband stress wave steering in periodic lattices. *International Journal of Solids and Structures*, 2013.
- P. Celli and S. Gonella. Manipulating waves with lego® bricks: A versatile experimental platform for metamaterial architectures. *Applied Physics Letters*, 107(8):081901, 2015.
- I. Chekkal, C. Remillat, and F. Scarpa. *High Performance Structures and Materials VI*, chapter Acoustic Properties of Auxetic Foams, pages 119–130. WIT Press, 2012.
- H. Chen and C. Chan. Acoustic cloaking in three dimensions using acoustic metamaterials. *Applied physics letters*, 91(18):183518, 2007.
- A. H.-D. Cheng. Material coefficients of anisotropic poroelasticity. *International Journal of Rock Mechanics and Mining Sciences*, 34(2):199–205, 1997.
- E. Chevillotte and R. Panneton. Elastic characterization of closed cell foams from impedance tube absorption tests. *The Journal of the Acoustical Society of America*, 122:2653, 2007.
- E. Chevillotte, C. Perrot, and R. Panneton. Microstructure based model for sound absorption predictions of perforated closed-cell metallic foams. *The Journal of the Acoustical Society of America*, 128:1766, 2010.
- R. Cook. *Concepts and applications of finite element analysis*. Wiley, 2001. ISBN 9780471356059.
- R. D. Cook et al. *Concepts and applications of finite element analysis*. John Wiley & Sons, 2007.
- J. M. Cowley. *Diffraction physics*. Elsevier, 1995.
- T. J. Cui, D. R. Smith, and R. Liu. *Metamaterials*. Springer, 2014.
- C. G. Darwin. Xxxiv. the theory of x-ray reflexion. *The London, Edinburgh, and Dublin Philosophical Magazine and Journal of Science*, 27(158):315–333, 1914.
- N. Dauchez, S. Sahraoui, and N. Atalla. Convergence of poroelastic finite elements based on biot displacement formulation. *The Journal of the Acoustical Society of America*, 109(1): 33–40, 2001.

Bibliography

- T. Delpero, S. Schoenwald, A. Zemp, and A. Bergamini. Structural engineering of three-dimensional phononic crystals. *Journal of Sound and Vibration*, 363:156–165, 2016.
- B. Dempsey, S. Eisele, and D. McDowell. Heat sink applications of extruded metal honeycombs. *International journal of heat and mass transfer*, 48(3):527–535, 2005.
- S. Diebels and W. Ehlers. Dynamic Analysis of a Fully Saturated Porous Medium Accounting for Geometrical and Material Non-linearities. *International Journal for Numerical Methods in Engineering*, 39(1):81–97, 1996.
- L. Dormieux, A. Molinari, and D. Kondo. Micromechanical approach to the behavior of poroelastic materials. *Journal of the Mechanics and Physics of Solids*, 50(10):2203–2231, 2002.
- V. Dorodnitsyn and A. Spadoni. Elastodynamics of a two-dimensional square lattice with entrained fluid—part i: Comparison with biot’s theory. *Journal of Vibration and Acoustics*, 136(2):021024, 2014a.
- V. Dorodnitsyn and A. Spadoni. Elasto-dynamic behavior of a two-dimensional square lattice with entrained fluid ii: Microstructural and homogenized models. *Journal of Vibration and Acoustics*, 136(3):031005, 2014b.
- V. Dorodnitsyn and B. Van Damme. Two-dimensional fluid-filled closed-cell cellular solid as an acoustic metamaterial with negative index. *Physical Review B*, 93(13):134302, 2016.
- O. Doutres, N. Atalla, and K. Dong. Effect of the microstructure closed pore content on the acoustic behavior of polyurethane foams. *Journal of Applied Physics*, 110(6):064901–064901, 2011.
- N. Dutta and H. Odé. Attenuation and dispersion of compressional waves in fluid-filled porous rocks with partial gas saturation (white model)-part i: Biot theory. *Geophysics*, 44(11):1777–1788, 1979.
- J. Ella. Bulk acoustic wave (baw) filter having a top portion that includes a protective acoustic mirror, Feb. 16 1999. US Patent 5,872,493.
- N. Epstein. On tortuosity and the tortuosity factor in flow and diffusion through porous media. *Chemical Engineering Science*, 44(3):777–779, 1989.
- A. C. Eringen. *Microcontinuum Field Theories: I. Foundations and Solids*. Microcontinuum Field Theories. Springer, 2001.

- H. Esfahlani, S. Karkar, H. Lissek, and J. R. Mosig. Acoustic dispersive prism. *Scientific reports*, 6, 2016.
- A. G. Evans, J. Hutchinson, and M. Ashby. Multifunctionality of cellular metal systems. *Progress in Materials Science*, 43(3):171–221, 1998.
- F. J. Fahy and P. Gardonio. *Sound and Structural Vibration: Radiation, Transmission and Response*. Elsevier Science, 2007.
- C. Feuillade. The attenuation and dispersion of sound in water containing multiply interacting air bubbles. *The Journal of the Acoustical Society of America*, 99:3412, 1996.
- L. Fok and X. Zhang. Negative acoustic index metamaterial. *Physical Review B*, 83(21):214304, 2011.
- R. Gabbrielli. A new counter-example to Kelvin's conjecture on minimal surfaces. *Philosophical Magazine Letters*, 89(8):483–491, 2009.
- R. Gabbrielli, A. J. Meagher, D. Weaire, K. A. Brakke, and S. Hutzler. An experimental realization of the Weaire–Phelan structure in monodisperse liquid foam. *Philosophical Magazine Letters*, 92(1):1–6, 2012.
- I. Gibson and D. Shi. Material properties and fabrication parameters in selective laser sintering process. *Rapid Prototyping Journal*, 3(4):129–136, 1997.
- L. Gibson and M. Ashby. *Cellular Solids: Structure and Properties*. Cambridge Solid State Science Series. Cambridge University Press, 1999. ISBN 9780521499118.
- L. J. Gibson. Biomechanics of cellular solids. *Journal of biomechanics*, 38(3):377–399, 2005.
- C. Goffaux, F. Maseri, J. Vasseur, B. Djafari-Rouhani, and P. Lambin. Measurements and calculations of the sound attenuation by a phononic band gap structure suitable for an insulating partition application. *Applied physics letters*, 83(2):281–283, 2003.
- S. Gonella and M. Ruzzene. Analysis of in-plane wave propagation in hexagonal and re-entrant lattices. *Journal of Sound and Vibration*, 312(1):125–139, 2008a.
- S. Gonella and M. Ruzzene. Homogenization and equivalent in-plane properties of two-dimensional periodic lattices. *International Journal of Solids and Structures*, 45(10):2897–2915, 2008b.

Bibliography

- P. Göransson. A 3D, symmetric, finite element formulation of the biot equations with application to acoustic wave propagation through an elastic porous medium. *International journal for numerical methods in engineering*, 41(1):167–192, 1998.
- K. Graff. *Wave Motion in Elastic Solids*. Dover Books on Engineering Series. Dover Publications, 1975.
- M. Gravade, M. Ouisse, M. Collet, F. Scarpa, M. Bianchi, and M. Ichchou. Auxetic transverse isotropic foams: from experimental efficiency to model correlation. *Acoustics 2012 Nantes*, 2012.
- I. Gueven, P. Kurzeja, S. Luding, and H. Steeb. Experimental evaluation of phase velocities and tortuosity in fluid saturated highly porous media. *PAMM*, 12(1):401–402, 2012.
- B. Gurevich, O. Kelder, and D. Smeulders. Validation of the slow compressional wave in porous media: comparison of experiments and numerical simulations. *Transport in porous media*, 36(2):149–160, 1999.
- W. D. Harkins. The evolution of the elements and the stability of complex atoms. i. a new periodic system which shows a relation between the abundance of the elements and the structure of the nuclei of atoms. *Journal of the American Chemical Society*, 39(5):856–879, 1917.
- M. T. Hoang and C. Perrot. Identifying local characteristic lengths governing sound wave properties in solid foams. *Journal of Applied Physics*, 113:084905, 2013.
- D. H. Hodges and G. A. Pierce. *Introduction to structural dynamics and aeroelasticity*, volume 15. cambridge university press, 2011.
- M. Itskov. On the theory of fourth-order tensors and their applications in computational mechanics. *Computer Methods in Applied Mechanics and Engineering*, 189(2):419–438, 2000.
- M. Kadic, T. Bückmann, N. Stenger, M. Thiel, and M. Wegener. On the practicability of pentamode mechanical metamaterials. *Applied Physics Letters*, 100(19):191901, 2012.
- S.-H. Kim and M. P. Das. Seismic waveguide of metamaterials. *Modern Physics Letters B*, 26(17):1250105, 2012.
- C. Kittel. *Introduction to Solid State Physics*. John Wiley & Sons, 2004. ISBN 9780471415268.

- T. F. Krauss, M. Richard, and S. Brand. Two-dimensional photonic-bandgap structures operating at near-infrared wavelengths. *Nature*, 383(6602):699–702, 1996.
- S. Krödel, T. Delpero, A. Bergamini, P. Ermanni, and D. M. Kochmann. 3D auxetic microlattices with independently controllable acoustic band gaps and quasi-static elastic moduli. *Advanced Engineering Materials*, 16(4):357–363, 2014.
- R. S. Kumar and D. L. McDowell. Generalized continuum modeling of 2-D periodic cellular solids. *International Journal of Solids and Structures*, 41(26):7399–7422, 2004.
- R. Lakes. Foam structures with a negative Poisson's ratio. *Science*, 235:1038–1040, 1987.
- C. Y. Lee, M. J. Leamy, and J. H. Nadler. Acoustic absorption calculation in irreducible porous media: A unified computational approach. *The Journal of the Acoustical Society of America*, 126:1862, 2009.
- J.-H. Lee, J. P. Singer, and E. L. Thomas. Micro- / nanostructured mechanical metamaterials. *Advanced materials*, 24(36):4782–4810, 2012.
- R. Lenhard and J. Parker. Measurement and prediction of saturation-pressure relationships in three-phase porous media systems. *Journal of Contaminant Hydrology*, 1(4):407–424, 1987.
- Z.-Y. Li, J. Wang, and B.-Y. Gu. Creation of partial band gaps in anisotropic photonic-band-gap structures. *Physical Review B*, 58(7):3721, 1998.
- E. Lind-Nordgren and P. Göransson. Optimising open porous foam for acoustical and vibrational performance. *Journal of Sound and Vibration*, 329(7):753 – 767, 2010.
- X. Liu, G. Hu, G. Huang, and C. Sun. An elastic metamaterial with simultaneously negative mass density and bulk modulus. *Applied physics letters*, 98(25):251907, 2011a.
- X. N. Liu, G. K. Hu, C. T. Sun, and G. L. Huang. Wave propagation characterization and design of two-dimensional elastic chiral metacomposite. *Journal of Sound and Vibration*, 330(11): 2536–2553, 2011b.
- Z. Liu, X. Zhang, Y. Mao, Y. Zhu, Z. Yang, C. Chan, and P. Sheng. Locally resonant sonic materials. *Science*, 289(5485):1734–1736, 2000.
- S. Lopatnikov and A.-D. Cheng. Macroscopic Lagrangian formulation of poroelasticity with porosity dynamics. *Journal of the Mechanics and Physics of Solids*, 52(12):2801–2839, 2004.
- T. J. Lu, F. Chen, and D. He. Sound absorption of cellular metals with semiopen cells. *The Journal of the Acoustical Society of America*, 108:1697, 2000.

Bibliography

- V. Martin. *Éléments d'acoustique générale: de quelques lieux communs de l'acoustique à une première maîtrise des champs sonores*. Presses polytechniques et universitaires romandes, 2007. ISBN 9782880746544.
- R. Martinezsala, J. Sancho, J. Sánchez, V. Gómez, J. Llinares, and F. Meseguer. Sound-attenuation by sculpture. *nature*, 378(6554):241–241, 1995.
- P. G. Martinsson and A. B. Movchan. Vibrations of lattice structures and phononic band gaps. *The Quarterly Journal of Mechanics and Applied Mathematics*, 56(1):45–64, 2003.
- H. Masuda and K. Fukuda. Ordered metal nanohole arrays made by a two-step replication of honeycomb structures of anodic alumina. *Science*, 268(5216):1466–1468, 1995.
- F. Maurin. Bloch theorem with revised boundary conditions applied to glide and screw symmetric, quasi-one-dimensional structures. *Wave Motion*, 61:20–39, 2016.
- D. M. Mead. Wave propagation in continuous periodic structures: research contributions from Southampton, 1964-1995. *Journal of Sound and Vibration*, 190(3):495 – 524, 1996.
- G. W. Milton and A. V. Cherkaev. Which elasticity tensors are realizable? *Journal of engineering materials and technology*, 117(4):483–493, 1995.
- M. Minnaert. XVI. On musical air-bubbles and the sounds of running water. *The London, Edinburgh, and Dublin Philosophical Magazine and Journal of Science*, 16(104):235–248, 1933.
- M. Molerón, M. Serra-Garcia, and C. Daraio. Acoustic fresnel lenses with extraordinary transmission. *Applied Physics Letters*, 105(11):114109, 2014.
- P. M. Morse and H. Feshbach. *Methods of theoretical physics*. 1953.
- J. T. Nelson. Acoustic emission in a fluid saturated heterogeneous porous layer with application to hydraulic fracture. *Lawrence Berkeley National Laboratory*, 1988.
- A. N. Norris. Acoustic metafluids. *The Journal of the Acoustical Society of America*, 125(2): 839–849, 2009.
- J. Pendry. Negative refraction makes a perfect lens. *Physical review letters*, 85(18):3966–3969, 2000.
- C. Perrot, F. Chevillotte, and R. Panneton. Bottom-up approach for microstructure optimization of sound absorbing materials. *The Journal of the Acoustical Society of America*, 124:940, 2008a.

- C. Perrot, F. Chevillotte, and R. Panneton. Dynamic viscous permeability of an open-cell aluminum foam: Computations versus experiments. *Journal of Applied Physics*, 103(2): 024909–024909, 2008b.
- A. S. Phani, J. Woodhouse, and N. A. Fleck. Wave propagation in two-dimensional periodic lattices. *The Journal of the Acoustical Society of America*, 119(4):1995–2005, 2006.
- J. Plateau. Experimental and theoretical statics of liquids subject to molecular forces only. 1873.
- J. R. Rice and M. P. Cleary. Some basic stress diffusion solutions for fluid-saturated elastic porous media with compressible constituents. *Rev. Geophys. Space Phys*, 14(2):227–241, 1976.
- A. P. Roberts and E. J. Garboczi. Elastic moduli of model random three-dimensional closed-cell cellular solids. *Acta materialia*, 49(2):189–197, 2001.
- M. Ruzzene, F. Scarpa, and F. Soranna. Wave beaming effects in two-dimensional cellular structures. *Smart materials and structures*, 12(3):363, 2003.
- J. Sánchez-Pérez, D. Caballero, R. Martínez-Sala, C. Rubio, J. Sánchez-Dehesa, F. Meseguer, J. Llinares, and F. Gálvez. Sound attenuation by a two-dimensional array of rigid cylinders. *Physical Review Letters*, 80(24):5325, 1998.
- J. E. Santos, J. Douglas Jr, J. Corberó, and O. M. Lovera. A model for wave propagation in a porous medium saturated by a two-phase fluid. *The Journal of the Acoustical Society of America*, 87:1439, 1990.
- D. Schurig, J. Mock, B. Justice, S. Cummer, J. Pendry, A. Starr, and D. Smith. Metamaterial electromagnetic cloak at microwave frequencies. *Science*, 314(5801):977–980, 2006.
- J. Sherwood. Biot poroelasticity of a chemically active shale. 440(1909):365–377, 1993.
- J. Shim, C. Perdigou, E. R. Chen, K. Bertoldi, and P. M. Reis. Buckling-induced encapsulation of structured elastic shells under pressure. *Proceedings of the National Academy of Sciences*, 109(16):5978–5983, 2012.
- D. Smeulders and M. Van Dongen. Wave propagation in porous media containing a dilute gas–liquid mixture: theory and experiments. *Journal of Fluid mechanics*, 343:351–373, 1997.
- D. Smith, W. Padilla, D. Vier, S. Nemat-Nasser, and S. Schultz. Composite medium with simultaneously negative permeability and permittivity. *Physical review letters*, 84(18):4184–4187, 2000.

Bibliography

- A. Spadoni and M. Ruzzene. Elasto-static micropolar behavior of a chiral auxetic lattice. *Journal of the Mechanics and Physics of Solids*, 2011.
- A. Spadoni and M. Ruzzene. Elasto-static micropolar behavior of a chiral auxetic lattice. *Journal of the Mechanics and Physics of Solids*, 60(1):156–171, 2012.
- A. Spadoni, M. Ruzzene, S. Gonella, and F. Scarpa. Phononic properties of hexagonal chiral lattices. *Wave Motion*, 46(7):435–450, 2009.
- A. Spadoni, R. Höhler, S. Cohen-Addad, and V. Dorodnitsyn. Closed-cell crystalline foams: Self-assembling, resonant metamaterials. *The Journal of the Acoustical Society of America*, 135(4):1692–1699, 2014.
- M. Stadler and M. Schanz. Acoustic band structures and homogenization of periodic elastic media. *PAMM*, 10(1):427–428, 2010.
- M. R. Stinson and Y. Champoux. Propagation of sound and the assignment of shape factors in model porous materials having simple pore geometries. *The Journal of the Acoustical Society of America*, 91:685, 1992.
- A. J. Suiker, A. V. Metrikine, and R. De Borst. Comparison of wave propagation characteristics of the Cosserat continuum model and corresponding discrete lattice models. *International Journal of Solids and Structures*, 38(9):1563–1583, 2001.
- M. Thompson and J. R. Willis. A reformulation of the equations of anisotropic poroelasticity. *Journal of Applied Mechanics-ASME*, 58:6122616, 1991.
- W. S. Thomson. On the division of space with minimum partitional area. *Acta mathematica*, 11(1-4):121–134, 1887.
- V. G. Veselago. The electrodynamics of substances with simultaneously negative values of ϵ and μ . *Sov. Phys. Usp.*, 10:509–514, 1968.
- A. Wang and D. McDowell. Yield surfaces of various periodic metal honeycombs at intermediate relative density. *International Journal of Plasticity*, 21(2):285–320, 2005.
- X. Wang and T. J. Lu. Optimized acoustic properties of cellular solids. *The Journal of the Acoustical Society of America*, 106:756, 1999.
- M. Warner, B. Thiel, and A. Donald. The elasticity and failure of fluid-filled cellular solids: Theory and experiment. *Proceedings of the National Academy of Sciences*, 97(4):1370–1375, 2000.

- D. Weaire and S. Hutzler. *The Physics of Foams*. Clarendon Press, 2001. ISBN 9780198510970.
- D. Weaire and R. Phelan. A counter-example to Kelvin's conjecture on minimal surfaces. *Philosophical Magazine Letters*, 69(2):107–110, 1994.
- G. Widawski, M. Rawiso, and B. Francois. Self-organized honeycomb morphology of star-polymer polystyrene films. 1994.
- J. P. Wolfe. *Imaging phonons: acoustic wave propagation in solids*. Cambridge University Press, 2005.
- Y. L. Xu, X. G. Tian, and C. Q. Chen. Band structures of two dimensional solid/air hierarchical phononic crystals. *Physica B: Condensed Matter*, 407(12):1995–2001, 2012.
- Y. Yan, A. Laskar, Z. Cheng, F. Menq, Y. Tang, Y. Mo, and Z. Shi. Seismic isolation of two dimensional periodic foundations. *Journal of Applied Physics*, 116(4):044908, 2014.
- H. Zhu and F. Semperlotti. Metamaterial based embedded acoustic filters for structural applications. *AIP Advances*, 3(9):092121, 2013.

Curriculum Vitae



Vladimir Dorodnitsyn

address: Av. de Prefaully, 15c,
1022 Chavannes-pres-Renens, Switzerland
mob. phone: +41 (76) 587-4288
email: vladimir.dorodnitsyn@gmail.com
born: June, 04, 1987

Education

2009: M.Sc. and B.Sc., Lomonosov Moscow State University,
department of mechanics and mathematics, laboratory of gas and wave dynamics.
M.Sc. project on cylindrical shells under external pressure, supervised by prof. A.V.
Zvyagin. The thesis has been awarded with the second place among all mechanics
and math graduates in 2009.

Work experience

2010-2011: *Accenture*, Business Analyst, system integration, SAP eWM (full-cycle
implementation project, and several partial ones).

Teaching

Teaching assistant at EPFL in Solid Mechanics (2012-2014), General Physics (2013),
and Aeroelasticity (2014).

Supervision of EPFL's students in Mechanical Engineering under their final B.Sc.
project (2012).

Extracurricular activity

President of international nonprofit student consulting organization, SHARE EPFL
(2013-2015). In collaboration with TTO EPFL and external partners.

Language skills

English: fluent
French: communicational
German: basic
Russian: native

Publications

Peer-reviewed journal articles

V. Dorodnitsyn and A. Spadoni. Elastodynamics of a two-dimensional square lattice with entrained fluid—part i: Comparison with biot’s theory. *Journal of Vibration and Acoustics*, 136(2):021024, 2014a

V. Dorodnitsyn and A. Spadoni. Elastodynamics of a two-dimensional square lattice with entrained fluid—part ii: Microstructural and homogenized models. *Journal of Vibration and Acoustics*, 136(3):031005, 2014b

A. Spadoni, R. Höhler, S. Cohen-Addad, and V. Dorodnitsyn. Closed-cell crystalline foams: Self-assembling, resonant metamaterials. *The Journal of the Acoustical Society of America*, 135(4):1692–1699, 2014.

V. Dorodnitsyn and B. Van Damme. Analytical Analysis of Slow and Fast Pressure Waves in a 2D Cellular Solid with Fluid-filled Cells. *Currently in review, JASA Special Issue on Metamaterials, 2016.*

V. Dorodnitsyn and B. Van Damme. A 2D Fluid-filled Closed-Cell Cellular Solid as an Acoustic Metamaterial with Negative Index. *Physical Review B*, 93(13):134302, 2016

Conference Proceedings

V. Dorodnitsyn and A. Spadoni. Elastodynamics of a two-dimensional square lattice with entrained fluid, In Proceedings of *11Th World Congress On Computational Mechanics and 5Th European Conference On Computational Mechanics (ECCM)*, Barcelona, Spain 2014.

Conference presentations

Elastodynamics of a two-dimensional square lattice with entrained fluid, *11Th World Congress On Computational Mechanics and 5Th European Conference On Computational Mechanics (ECCM)*, Barcelona, Spain 2014.

Microstructural and Homogenized Models for a Two-Dimensional Square Lattice With Entrained Fluid, *ASME International Mechanical Engineering Congress & Exposition*, Montreal, Canada, 2014.

External talks

Swiss Federal Laboratories for Materials Science and Technology (EMPA), Dübendorf, Switzerland, 2015.

